A ROTATING MODULATION IMAGER FOR THE ORPHAN SOURCE SEARCH PROBLEM

by

Benjamin Raymond Kowash

A dissertation submitted in partial fulfillment
of the requirements for the degree of
Doctor of Philosophy
(Nuclear Engineering and Radiological Sciences)
in The University of Michigan
2008

Doctoral Committee:

Professor David K. Wehe, Chair
Emeritus Professor Ziyaeddin A. Akcasu
Professor Jeffrey A. Fessler
Professor Ronald F. Fleming

ACKNOWLEDGEMENTS

The past three years have moved by so quickly and at times it did not seem like it would be possible to design and build a prototype RMC system, develop a new system model, conduct the experiments necessary to write a dissertation, and then actually put the document together. This dissertation would not have been possible without the help from a large supporting cast of people who helped me at critical steps along the way.

I would first like to thank my faculty advisor and dissertation chair, Prof. Wehe, who provided a great pool of research topics to choose from initially, and then always came up with intriguing questions to push my research forward.

My research committee provided outstanding support to this research effort. I want to thank Prof. Akcasu for the time he spent working with me on my system model and discussing the statistical behavior of the RMC. Prof. Fessler introduced me to the world of estimation theory, which has opened up an entire new realm of future research possibilities. Thank you for your patience and your outstanding mentoring style that helped me learn these powerful concepts quickly. Finally Prof. Fleming always was available to provide critical feedback and always had unique twists that I could apply to the problem. I will not forget his sage advice (I think borrowed from Feynman) to always look first for the easiest problems that have not yet been solved, and then go solve them.

I am also extremely grateful for the support of my research group over the past three years. Jim Berry acted as a sounding board during the design phase of the RMC. Without his experience, the prototype system would have been a much less robust device. Paul, Haori, Jason, and Wonho all took time out of their research schedules to get me started in the lab and their continued support throughout this research was crucial to finishing on time. Finally I would like to acknowledge the support of my wife and son, who put up with the long hours away from home to achieve this goal.

TABLE OF CONTENTS

ACKNOWLEDGEMENTS.. ii

LIST OF FIGURES vi

LIST OF TABLES... xiii

LIST OF APPENDICES xv

ABSTRACT xvi

CHAPTER

I. INTRODUCTION 1

1.1 Previous Research and Motivation 3

1.2 Contributions of this Work 6

1.3 Overview of the Dissertation 8

II. THEORY OF RMC OPERATIONS 10

2.1 RMC Operation.. 11

2.2 RMC System Models 12

2.2.1 Far Field Models 13

2.2.2 Near Field Model 17

2.2.3 Universal Field Model 17

2.2.3.1 Modeling Mask Thickness 23

2.2.3.2 Modeling Mask Penetrations 24

2.2.3.3 Computer Implementation of System Model........................ 25

2.2.3.4 Computation of Solid Angle 27

2.2.3.5 Detector Efficiency 30

2.2.3.6 Unmodulated Background – b(E) 31

2.2.3.7 Comparison of Universal Field to the Wilmore Far Field Model..... 32

2.2.3.8 RMC Response to Complex Source Geometries 34

2.3 RMC Data Analysis and Image Reconstruction 37

2.3.1 Log-Likelihood Function, Fisher Information, and Cramer Rao Lower Bound on Variance 39

2.3.2 Estimation of Source Parameters Using Log-Likelihood and Maximum Likelihood Expectation Maximization 43

2.4 RMC Indicators of Performance 50

2.4.1 System Angular Resolution, Depth Resolution, and Point Spread Function 50

2.4.2 Modulation Efficiency and Dynamic Range 52

2.4.3 Estimator Variance Via a Parametric Bootstrap Routine..................... 52

2.4.4. RMC Sensitivity and Source Detection 53

2.5 Summary of RMC Theory 56

III. RMC SYSTEM DESIGN AND OPERATIONAL PARAMETERS...58

3.1 Design Requirements 59

3.1.1 RMC Structural Design... 59

3.1.2 RMC Mask Design 61

3.1.3 Automation, Control, and Feedback Systems 64

3.1.4 Data Acquisition 65

3.1.5 System Calibration 67

3.1.5.1 Mask Alignment.. 67

3.1.5.2 Setting the RMC Initial Position 68

3.1.5.3 Source Positioning System 68

3.1.6 Validation of the Universal Field Model 70

3.2 RMC Operational Parameters 72

3.2.1 Mask Separation Parameter 73

3.2.2. Adaptive Imaging Using the Dwell Time Parameter.......................... 82

3.3 Summary of RMC System Design and Operational Parameters 87

IV. MEASURED PERFORMANCE OF AN RMC FOR THE ORPHAN SOURCE SEARCH PROBLEM.......................................90

4.1 RMC Response to an Unmodulated Background 91

4.1.1 Known vs. Unknown Uniform Background 92
4.1.2 Measuring the Unmodulated Background 95
4.2 RMC Response to a Single Point Source.. 95
4.2.1 Measurement of RMC Accuracy and Bias for a Single Point Source in Two-Dimensions.. 95
4.2.2 Estimation of the Depth Coordinate and Associated Accuracy and Bias 101
4.3 RMC Response to Multiple Point Sources 112
4.3.1 Angular Resolution 113
4.3.2 Dynamic Range.. 116
4.3.3 Response to Multiple Sources of Different Energy 119
4.4 Detection Time 124
4.5 Summary of RMC Measurements and Simulations 128
V. CONCLUSIONS AND FUTURE WORK 132
5.1 Review of Key Findings 132
5.2 Suitability of the RMC to the Orphan Source Search Problem 135
5.3 Future Work.. 137
5.3.1 System Design Enhancements and Optimization 137
5.3.2 Imaging with RMC arrays 139
5.3.3 Further Adaptive Imaging Studies... 141
5.3.4 Time Coded Apertures... 141
APPENDICES.. 144
REFERENCES 151

LIST OF FIGURES

Figure

2-1. The RMC process is illustrated for a far field source as the masks are rotated together (or similarly the source orbits a set of fixed masks). The green circle represents the projection of the front mask and the blue circle represents the fixed rear mask and detector as shown in the lower picture. The yellow star indicates the orientation of the source with respect to the masks. As the masks rotate the slits appear to open and close, creating a modulated pattern. 11

2-2. (a) One possible configuration of a RMC system. As the mask pair is rotated together, the slit pairs will appear to move across each other for any source located off the centerline axis. This has the effect of either blocking the source or allowing photons to pass to the detector. This produces the modulated detector response seen in (b)... 12

2-3. A picture of the 1D transmission function used by Wilmore to describe the fate of a photon incident on a 1D black mask. If the photon hits an open element it is transmitted and the function M(x) = 1. If the photon hits a closed mask element it is not transmitted to the detector and M(x)=0. (image reproduced from Wil70)......... 14

2-4. The coordinate system used to define the postion of the RMC with respect to the source is used throughout this thesis. The polar notation ρ and ϕ are the convention often used in astronomy for sources in the far field. Any source located along the line defined by the coordinates ρ and ϕ will the same transmission function in the far field. 18

2-5. When the source is in the near field the forward projection (A) of the front mask is magnified as expected. For the numerical approach taken, it is often easier to consider the back projection (B) of the rear mask and detector up to the top plane of the front mask. Regardless of the direction of projection, both methods produce the same result.. 19

2-6. This shows the basic pattern for a RMC mask and the required parameters..... 21

2-7. This illustrates how the mask thickness is modeled by representing a single mask using the same technique used to define the RMC. Instead of two planes separated by a distance L, there are four planes with the distance between planes 2 and 3 separated by L and the other planes by a distance t. The single mask constraint is understood by comparing photon 1 versus photon 2. The first photon enters the top mask pair in the third slit, but passes through the second slit on the bottom mask. With a single black mask this is physically impossible (see photon 2). For a case like photon 2, the bottom mask would be considered closed and the transmission would be 0.. 24

2-8. Comparison of a point source far field model versus the UM system model at various ranges for two masks with no thickness and a mask separation parameter L=24 cm. The source is located at ρ,ϕ = 2.87°. 33

2-9. The RMC point source transmission function deviates from the far field model when a finite mask thickness is considered. In this case the masks are 12.7 mm thick and the mask separation parameter L=24 cm. The source is located at ρ,ϕ = 2.87°. 34

2-10. The top plot shows the RMC transmission function for an extended circular source, while the bottom plot shows an extended line source. In both cases, the object only appears extended once it is greater than ~0.5 times the angular resolution of the system. Past this point the transmission function becomes compressed, as some of the source is always visible to the detector regardless of the mask orientation. This is very similar to the effect produced when a point source is in the near field. 36

2-11. These maps show the Fisher information and CRLB for a 2 mCi point source located 250 cm from the RMC. The maps have an expected symmetry, as the information at a given radial coordinate should be the same regardless of the azimuthal coordinate. In the lower right picture, the CRLB at the center pixel has been removed, because it had a value of 10^{12}, which is 14 orders of magnitude greater than the other pixels. This is expected, since the RMC has no sensitivity for sources directly on axis. The values F_{11}, F_{22}, F_{33}, $CRLB_{11}$, $CRLB_{22}$, and $CRLB_{33}$ indicate the location of the estimate in the Fisher Information and CRLB matrices.42

2-12. Shown here are maps of the log-likelihood function as a function of the three spatial coordinates x,y,z, and the source activity. The MLE for all of the images occurs at x,y,z = (10,0,300) cm and α = 200 μCi, given by the image in the 3rd row and 2nd column (shown in the red box). The MLE matches exactly with the true source coordinates and activity.. 44

2-13. This is the RMC transmission function and associated MLEM reconstructed image for a point source located at x,y,z = 15,15,250 cm. The 180° ambiguity results from the symmetric nature of the transmission function. This ambiguity can be resolved by making a second measurement at a different position as proposed by several authors. Alternatively the ambiguity can be resolved by modifying the mask design so it is no longer symmetric. This will be discussed further in Chapter 3. .. 49

2-14. The transmission function of two point sources as recorded by a single RMC can be useful for understanding the angular resolution. In this simulation, the theoretical resolution, Θ, is 0.955° shown by the cyan curve. When the source separation is less than 0.5Θ the two sources are not resolved as two independent points. 51

2-15. The histograms shown above are used to compare the performance of an RMC system against a bare detection system. The red distributions represent the source + background, while the blue distributions are background only. These distributions are then used to generate receiver operating curves (ROC) that are indicators of the separation between distributions. When the two distributions overlap the ROC curves will be a straight line between 0,0 and 1,1. The area under the ROC curve can be used as a metric to compare the two systems. 56

3-1. Illustration of the RMC system design. 60

3-2. This figure illustrates how the modulation efficiency changes as a function of mask thickness for both tungsten and lead masks. The black line shows how the field of view changes with thickness when the slits are 4mm wide. 61

3-3. When the RMC masks are symmetric (left panels) the 180° ambiguity is apparent. When the masks are made asymmetric (right panels) the ambiguity can be resolved with a single measurement. The cost of making the masks asymmetric is a reduction in the RMC modulation and geometric efficiency. 63

3-4. Block diagram of the RMC data acquisition system. 66

3.5. A picture of the Velmex source positioning system used to accurately position the source with respect to the RMC is shown in the top right panel. The RMC (top left) is mounted on a frame that can be aligned to the Velmex system. Once the frames are calibrated and aligned, the source can be positioned with 5 μm of precision. The bottom panel shows the RMC as seen from behind the source positioning system. 69

3-6. The universal field system model described in chapter 2 is plotted against data measured using the RMC system outlined in chapter 3. The model is accurate even when the source is 1 meter from the RMC. The discrepancy between the model and data at the large dip is caused by the model's assumption of black masks. 71

3-7. The separation between the masks impacts the frequency of the transmission function as shown here for a point source at x,y,z = (0,-10,241) cm. When the masks are close together the transmission function has a lower frequency than when they are further apart. 74

3-8. The CRLB on the source position is affected by the choice of mask separation. It is seen that no single mask separation parameter has the best variance properties at all positions. This reflects the fact that each mask separation parameter is most sensitive to a particular set of spatial frequencies in the source scene. The magenta and cyan curves representing L=30 and 35 cm mask separations have poor variance properties because of excessive magnification values when the source is in the near field. 75

3-9. The images above illustrate the benefits of measuring a source scene with different values of the mask separation parameter. The simulated rigid ruler source contains 8 independent sources that are 1 cm long. There is also a 1 cm separation between each source. The image becomes better resolved as more mask separation values are added. 77

3-10. The three panels here demonstrate how a stronger nuisance source (T shaped source) can be removed during the MLEM algorithm to reveal a weaker target source. The first panel is the image when just the nuisance T-shaped source is present. The second panel contains both the nuisance source and weak point source. The third panel shows the weak source once the nuisance source is removed by adding its transmission function to the unmodulated background variable............. 81

3-11. For each rotation the sum of the elements of τ remains constant. This process is repeated until the total time allocated for the measurement has elapsed. 83

3-12. The log-likelihood distributions and their associated ROC curves are shown in this figure. The panels on the left assume the uniform sampling scheme, while the panels on the right assume the adaptive sampling scheme. These figures are generated for the case where the source activity and location are known exactly, and the purpose is to illustrate that the adaptive scheme is superior if the true source position can be located quickly. The area under the curve for the uniform scheme is 0.91 and the area under the curve for the adaptive scheme is 0.97.......................... 86

4-1. Shown is the simulated RMC response to a uniform background, when different values are assumed for the background in the ML-EM algorithm. Plot (A) shows when the background is underestimated for a single image, producing a slightly elevated SNR. This can be resolved by using the bootstrap method to generate multiple images (B) and using the mean image to produce a SNR, which is ~1. Plot (C) is the MLE when the assumed background for the ML-EM algorithm is exact, and (D) shows when the background is overestimated. 94

4-2. The RMC blind spot is illustrated here as the region from ρ=0 to ~0.7°, where the modulation pattern is too uniform to allow for accurate reconstructions. The system resolution, which defines the width of the blind zone is 0.955° and matches well with the measured data. 97

4-3. In the RMC active sensing region, position estimation using the MLEM algorithm is very accurate. With the exception of the source located at ρ=0, the average standard deviation on the position estimate for sources located between the blind zone and field of view edge is ~1.6 arc minutes. 98

4-4. A slight modulation occurs for sources outside the system FOV (Eq. 2.32) that is caused by photons passing through the single mask closest to the detector. In this figure the source is located at ρ,ϕ = (25,0)°, while the FOV is ~17°. 99

4-5. Result from 50 iterations of ML-EM algorithm for a source at x,y,z = (40,-20,215) cm. The point location estimate is not produced, but the broad edge region does point in the direction of the source shown as a white circle. 100

4-6. The difference in the universal and far field models for a source located at (2.87,0)° and 200 cm is apparent in both the transmission functions shown in the top plot, and in the distributions of the log-likelihood value for both models. As the source moves further from the RMC, both transmission functions begin to appear the same and the separation between the distributions decreases. At very large distances the universal and far field models are identical, and the distributions overlap completely. 102

4-7. This plot illustrates the difference between the universal and far field model as the source moves from the near- to mid- and finally far field. 103

4-8. This figure illustrates how the RMC transmission functions change as the source moves from one depth to another, by considering the difference between the different log-likelihood distribution mean ratio. The two most important characteristics to note are that for near field sources the RMC transmission function changes dramatically as a function of depth. As the source moves very far from the detector, the change in the transmission function versus a change in depth is very small and approaches the far field limit. 104

4-9. This is the experimental setup used to test the ability of the RMC to locate point sources in three dimensions. 106

4-10. Shown above is the MLEM image using 20x20 pixels and ten image planes from S_Z=100 to 1000 cm. The true source position is ρ,ϕ,S_Z = (2.87°,0°,500 cm) and the activity is 1.7 mCi (corresponding true image is shown in the red box). Every image with the exception of S_Z=100 cm accurately predicts the polar coordinates ρ and ϕ, while the depth and activity estimates remain ambiguous. The colorbars on each image have units of mCi. It is apparent that this method alone is insufficient to locate the source in 3D. 107

4-11. The above images are generated by executing 10 independent runs of the MLEM algorithm, at a fixed source to detector distance. Unlike Fig. 4.10, the true source position is reflected in all images. Additionally, the images are less resolved at distances less than the true source position shown by the red box. This can be used to constrain the depth coordinate search to distances above this cut line....... 109

4-12. The blue curve represents the angular resolution (in arcminutes) as a function of the source depth coordinate, S_Z. These simulated data use the RMC design from Chapter 3 and assume that the unmodulated background is zero. The black Xs are measured data using the prototype RMC and the results match the simulations very well. The red line is the theoretical far field resolution given by Eq. 2.22........... 114

4-13. The angular resolution is shown as a function of the signal to background ratio when the source is 1027 cm from the RMC. When the source is very intense the resolution approaches the limit shown in Fig. 4.12. Even when the source to background ratio is near unity, the resolution is still less than 1.5°. The dotted red line shows the theoretical far field resolution predicted by Eq. 2.33..................... 115

4-14. The dynamic range is measured by recording the detector response for a cold and hot source. In order to limit the effects caused by measuring data at different radii, the sources are located the same distance from the RMC axis of rotation with an angular separation between sources of ~2°.. 117

4-15. The dynamic range shown here is a measure of the RMC's ability to locate a weak source in the presence of a hot source. When the signal to noise ratio of the weak source falls below five, the weak source is no longer detectable. This condition is met when the dynamic range is ~6, which means that the RMC shown in Chapter 3 can locate a source that is six times weaker than the hottest source in the field of view. 118

4-16. The background subtracted pulse height spectrum for three sources (Ba-133, Cs-137, and Co-60) is shown here. Down scattering from the higher energy sources leads to more noise in the Cs-137 and Ba-133 peaks. It is later shown that the accuracy of the estimates is not significantly impacted as long as this additional noise is included in the system model.. 120

4-17. The effects of higher energy sources on the transmission function at lower energies is highlighted in the top window of this figure. The down scattered photons are not modulated in time, but instead contribute a uniform background in the energy window of interest (356 keV for this figure). When this background is correctly accounted for using the MLEM algorithm, a strong image is formed. Panel A is the image of only the Ba-133. Panel B is the image with the Ba-133 and Cs-137 sources present. Panel C is the image formed using the Ba-133, Cs-137, and Co-60 sources... 124

4-18. The three histograms above show the log-likelihood distributions for different total measurement times (A-144 sec, B – 216 sec, C – 360 sec). The red distribution is the log-likelihood distribution when only background is present and the blue distribution is the source plus background distribution. As the total measurement time increases, the distributions separate and the probability that the measured data will produce an image that accurately locates the source increases. 126

4-19. This shows the minimum detectable source at various distances from the detector using the RMC with a allotted scan time of 30 minutes. The detection values are to 99% confidence that the RMC measurement will produce an image showing the position of the source... 128

5-1. Increasing the size of the front mask (B) increases the system field of view. Increasing the mask size is limited however, because of the finite field of view caused by the thickness of a single mask.. 139

5-2. A fan beam array of RMCs is a possible configuration that could be used to extend the RMC field of view. The blue tubes represent the RMCs with the black dotted line denoting the axis of rotation. Potential blind spots in the array could be alleviated by placing the entire assembly on a rotary table and rotating the system halfway through a measurement to ensure full coverage....................................... 140

5-3. This illustrates how a time coded aperture operates. The coded mask is moved across the pinhole aperture and position sensitive detector. At each time step the mask stops and a measurement is made. The combined measurements at all mask positions produce a higher quality image than just a single coded aperture alone. 142

LIST OF TABLES

Table

2-1. Listed below are the photopeak efficiencies for three commonly used sources in this research. 31

2-2. This shows how the data is recorded as the RMC rotates. The final modulation function is simply the sum of all the counts each discrete rotation angle ωt. For a bootstrap technique, a new modulation function T_{new} is created by random resampling of the columns N times and summing the results. R_n represents the RMC transmission function for the n_{th} rotation. 53

3-1. The data listed below are the estimates of the polar coordinates for a source located at $\rho,\phi = (2.87,-90)°$. The universal field model produces superior estimates based on the position accuracy and standard deviation. The far field model becomes more accurate as the source moves further from the detector toward a far field condition. 72

4-1. Experimental Setup for 2-D mapping of the RMC response to a single point source. 95

4-2. Statistics of Interest for RMC Position Estimation in the active sensing region. 98

4-3. This table shows the depth and activity estimates for eight measured data sets taken at various distances from the RMC. The results were obtained by taking the mean of 10 different runs of the Matlab gradient search algorithm ‘fmincon’, when the initial starting guess for both depth and activity were selected randomly. The polar coordinates ρ and ϕ for each data set are found using the MLEM procedure shown previously and then used as inputs to the ‘fmincon’ routine. 111

4-4. The first row of this table lists the number of counts recorded under the specific photopeak shown in the columns. The second row lists the lower and upper channels that bound the photopeak in the multi-channel spectrum (using 4096 channels). The values in parentheses are the associated voltage settings that are used to set the single channel analyzer windows. 120

4-5. This data shows the number of counts under a specified photopeak when various combinations of sources other than the photopeak source are present. As with Fig. 4.16 this data shows that the lower energy peaks are corrupted by down scattered photons, while the high energy peaks are unperturbed as expected. 121

4-6. Shown below are the polor coordinate and activity estimates when the SCA window is set for the 356 keV photopeak. The true source position is x,y = (10,0) cm and the true activity is 100 μCi. The estimates shown are mean estimates generated from 100 iterations of the bootstrap algorithm. 122

4-7. This table compares the simulated true positive ratio found by comparing the log-likelihood distributions against the measured true positive ratio. Excellent agreement between the two methods indicates that the log-likelihood distributions can be used before a measurement to determine a detection limit based on the total sampling time allotted. 127

LIST OF APPENDICES

Appendix

A. DERIVATIONS AND COMPUTATIONS 145

B. EXPERIMENTAL SETUP AND SYSTEM SETTINGS 148

C. TWO DIMENSIONAL IMAGES OF MASK PENETRATIONS MEASURED USING A HPGE STRIP DETECTOR 150

ABSTRACT

This dissertation explores the application of a mechanically collimated imaging device known as a rotating modulation collimator (RMC) to the orphan source search problem. Orphan sources are lost radioactive sources (accidentally or through material diversion) that can pose a threat to both human health and national security when they fall into the wrong hands. The RMC is a simple imaging system that can see through complex background scenes that can often mask these lost sources.

Key developments for this research include the development of a new system model for predicting the system response when the source is located at any distance from the detector, the design, construction, and characterization of a prototype RMC, new methods for locating sources in three dimensions with a RMC, a new operating mode for imaging extended sources, an initial study on adaptive imaging with the RMC, and a method for predicting the time required to detect a hidden source of a known activity to a given level of confidence. Results from simulations and measurements are used to asses the performance of the RMC for the orphan source search problem.

CHAPTER I

INTRODUCTION

In the fields of homeland security and environmental protection, much effort has been expended on the detection and localization of orphan radioactive sources. An orphan source is a radioactive source that has become lost either through poor accounting practices or by diversion of material by groups looking to smuggle and sell nuclear material. From an environmental protection standpoint, the detection and reclamation of these sources is often a matter of health and safety for populations located around the sources. A few examples taken from Eisenbud and Gesell's book "Environmental Radioactivity" illustrate this point [Eis97].

In December, 1983 a medical therapy machine containing 450 Ci of Co-60 was sold for scrap in Juarez, Mexico. During handling, the machine ruptured and the sources (encapsulated in 75 mCi pellets) were spread across the junk yard. Some of these sources found their way into a foundry where the sources became incorporated in steel that was used for furniture, rebar, and electric motors. Several hundred pellets fell into a truck that then sat on the streets of Juarez for close to two months. The problem was not detected almost a month later in January, 1984 when a truck loaded with rebar stopped for information at the gate of the Los Alamos National Lab. The bars triggered a radiation alarm, which set of a chain of events to trace the source of the radiation. It was determined that at least three people received doses of at least 100 rem from the truck parked on the street. The dose to the 50 people who worked at the scrap yard ranged from 390-635 rem. Fortunately the doses were received over an extended period of time and the effects of the exposure were mild (upset stomachs, nosebleeds). The economic impact was severe. The steel containing the sources had to be located and reclaimed, resulting in the destruction or partial destruction of 834 buildings. Over 3000 table bases and 600 tons of steel bars were reclaimed and 16000 m^3 of soil and 5000 m^3 of other material had to be placed in a special waste disposal site.

A second scenario had even more dire results. In 1987 a teletherapy machine containing 1375 Ci of Cs-137 (in the form of $CsCl_2$ powder) was abandoned at a medical clinic in Goiana, Brazil. The source assembly was removed from the shield and taken by wheelbarrow to a scrap scavenger's home, where two men tried to dissemble it using hammers. After five days, the remaining scrap was given to a local junkman who placed it in a backyard junk lot. At night the junkman noticed the source glowing and brought it into his living room for his friends and neighbors to admire. Several people removed pieces from the source as souvenirs. After two weeks the source was moved to a second junkyard, where workers attempted to disassemble it with a power saw. After two more weeks, several people who had handled the source were developing gastrointestinal problems. Shortly after a physicist was brought in to examine the scrap, and determined it was highly radioactive. The incident unfortunately left several casualties. Four people died from acute radiation exposure and one person had their arm amputated. Twenty-one people were hospitalized for serious skin burns and changes to their blood. While both of these incidents could have been avoided by applying proper safeguards, it highlights the terrible effects that orphan sources can impart when they fall into the wrong hands either accidentally or on purpose.

The orphan source problem became an even bigger concern following the attacks on the World Trade Center towers in New York City on September 11th, 2001. In January of 2003, the Center for Nonproliferation Studies (CNS) at the Monterey Institute of International Studies published a document called "Commercial Radioactive Sources: Surveying the Security Risk" [Fer03]. This document which was reviewed in the March 2003 edition of Nuclear News considered the security risk posed by commercially available radioactive sources [Tay03]. The security risk comes from terrorists acquiring these radioactive sources, and then detonating them in a radiological dispersal device (RDD). An RDD is a conventional explosive device that is used to spread radioactive material around a target area. Although the health threat would be minimal to most people outside of the blast zone, RDDs are recognized as a way to cause mass hysteria by playing on the general population's fear and misunderstanding of radiation. One part of the CNS document specifically addressed the problem of orphan sources in Russia and the developing world. Accurate inventories of sources in these parts of the world are incomplete, and therefore present a high risk for diverting material. Russia for example, produced several radioisotope thermoelectric generators (RTG) to provide power to remote locations of Siberia and southeast Russia. A single RTG can contain anywhere from 30000-300000 Ci of strontium-90 [Tay03]. Needless to say, an explosion containing one of these sources would be an environmental and security nightmare for any government agency to address.

Because of the threat posed by RDDs, much effort has recently gone into improving the capability to locate orphan sources created due to human error, natural disaster, environmental remediation of waste sites, or when nuclear material or weapons are clandestinely moved from one location to another. A current research initiative proposed by the US Department of Homeland Security's Domestic Nuclear Detection Office (DHS/DNDO) is called "Stand-Off Radiation Detection Systems (SORDS) and it seeks the development of autonomous detector systems that can locate an unshielded 1 mCi source at a range of 100 meters. This research focuses on a radiation imaging system known as a rotating modulation collimator that has been used in astronomy for the past several decades. Rotating modulation collimators are appealing for locating orphan sources because of their outstanding angular resolution (< 50 arc seconds at 1 MeV) and their relatively simple design. The theory behind these systems is presented in the next section and extensively in Chapter II.

1.1 Previous Research and Motivation

A reasonable assumption for locating a 1 mCi source at 100 meters is that the detectors need to be made as large as possible to maximize the geometric efficiency. Ziock et al. demonstrated however, that increasing the size of the radiation detector to improve sensitivity is not practical for orphan source search problems, because the background is typically variable over the search region [Zio02]. The source and background counts scale as the detector area is increased, and there is no net gain in the signal to noise ratio as the detector is made larger [Zio07]. The solution provided by their research is to apply imaging techniques to map both the source and background scenes. Imaging techniques effectively allow the user to see through the background improving the sensitivity of the system for orphan sources.

The large area imager developed by Ziock et al. at the Lawrence Livermore National Laboratory uses a 1-dimensional coded aperture imager and a 0.57 m^2 array of CsI detectors to meet the requirements of the SORDS proposal [Zio07-II]. The system is designed to fit inside a trailer which is then towed around areas where suspected orphan sources may be located. The coded aperture imagery data is fused with GPS data and overhead imagery to produce a map highlighting the position of the orphan source.

The rotating modulation collimator (RMC) is another class of mechanically collimated imager that makes use of multiplexing. Unlike coded apertures however, RMCs make use of a single non-position sensitive detector to record a one-dimensional time dependent map of a three-dimensional (spatial) source scene. The initial concept of modulating a detector response in time using a pattern of high Z wires was first proposed for X-ray astronomical observations by Oda [Oda65]. Shortly after this, Mertz introduced the modern RMC design which consist of two or more masks made out of high Z material that are mechanically linked together [Mer67]. The typical RMC mask pattern has parallel slits that run the length of the mask. When the masks are rotated together, the projection of the front mask orbits the rear mask causing the slits to appear to open and close to the source. The modulation function is recorded by binning the number of counts as a function of the rotational angle. Because the measured data is only an indirect measure of the image, a reconstruction algorithm must be applied to the data to create the image. Several different reconstruction methods have been applied to RMC data including filtered back projection, inverse Fourier transform methods, maximum likelihood, and the maximum likelihood expectation maximization algorithm (MLEM) [Sch67, Mur89,Huf02,Sha07-II]. The first two techniques produce ring side lobe artifacts in the reconstructed images. A second set of image processing algorithms developed for use in radio interferometry can then be applied to remove the artifacts [Huf02]. The process of RMC image formation and reconstruction will be explained with more detail in Chapter II.

Rotating modulation collimators have been used on several missions for observing astronomical sources of X- and gamma rays. Initial missions used a single RMC on platforms such as rotating sounding rockets or high altitude balloons. The detectors on these initial missions ranged from simple Geiger counters and films, to more complicated gas proportional counters as well as NaI and CsI scintillators [Oda65, Sch70,Lun81]. In 1986, Mertz et al. introduced the concept of using an array of RMC detectors as a way to image more complex source scenes [Mer86]. By creating mask patterns with different width slits, multiple RMCs can simultaneously measure multiple Fourier components of a given source scene. This additional information is used to generate images of extended sources. This concept was applied to the WINKLER spectrometer developed by Fisher et al., which used nine independent RMC grid pairs coupled to high-purity germanium detectors [Fis90]. The WINKLER spectrometer operated over an energy range of 25 keV to 10 MeV and with a 20° field of view and a 1.6° point spread function (FWHM). The germanium detectors provided an energy resolution of 2.4 keV at 1 MeV. The success of the WINKLER project led to the Reuven Ramaty High Energy Solar Spectroscopic Imager (RHESSI) satellite, which is the most current, ambitious, and successful RMC mission to date.

RHESSI, which was designed to provide hard X-ray images of the sun, contains nine individual RMCs coupled to nine segmented high-purity germanium detectors [RHE08]. The mask patterns for each of the nine collimator pairs are selected to measure multiple Fourier components of target source scene just like the WINKLER spectrometer. This provides the satellite with the capability to generate images of complex scenes associated with solar flares. The system has a spectral resolution of ~1 keV for photons up to 100 keV, ~3 keV for photons up to 1 MeV, and ~5 keV for photons at 20 MeV and with an effective energy range from 3 keV to 17 MeV. The field of view is 1°, which encompasses the entire sun. The angular resolution at 1 MeV is ~36 arcseconds. The success of RHESSI across such a wide range of energies and in such a high background environment indicates that RMCs could be a suitable option for the orphan source search.

A more recent body of research considered a RMC for imaging in the very near field. Sharma et al. developed a prototype RMC to be used with an imaging technique known as neutron stimulated emission computed tomography (NSECT) [Sha07-II]. This type of imaging uses a fast neutron beam (3-5 MeV) to stimulate nuclei through inelastic scatter. When the target nuclei de-excite they emit a characteristic photon which is measured and used to identify the target material. The RMC was selected as a potential gamma camera for this application because of its ability to produce high resolution images over a large energy range (0.4-6.5 MeV for NSECT). The group also recognized that the existing far field models were not sufficient for image reconstruction with the MLEM algorithm in the near field. A simple geometric model was developed that produced the shape of the modulation function, but did not account for certain physical effects such as grid shadowing and mask penetrations by high energy photons. These effects had to be modeled for NSECT images to be well resolved, so ultimately the required transmission functions were simulated using the Monte Carlo code GEANT-4. The research concluded that the RMC was not suitable for the NSECT mission because of its inability to image near field sources with the necessary degree of resolution needed for imaging human breast tissue with NSECT. The experiences provided by both the RHESSI satellite and the NSECT project helped focus some potential areas for this research.

1.2 Contributions of this Work

The primary objective of this research was to measure the performance of an RMC as it applies to the orphan source search problem. Although Sharma et al. studied an RMC for terrestrial use, all measurements were confined to the very near field (<50 cm to the detector). The orphan source search problem is concerned with sources ranging anywhere from 1 to 100 meters from the detector across a wide field of view (ideally 2π). Several new RMC tools were developed to support this research and several new applications are considered. The following is a list of the developments presented in this research.

1. A new universal field system model was developed to predict the RMC response for a source located at any position in the RMC field of view. This model was necessary to accurately locate and identify sources as they move close to the detector. Images generated using this new model showed better position accuracy and standard deviations than images generated using the far field models, when the source was less than 10 meters from the detector. The system model accounts for several physical parameters such as mask thickness, mask penetrations by high

energy photons, and the finite diameter grids.

2. The application of maximum likelihood techniques for RMC data was explored by both Murphy [Mur89] and Sharma [Sha07-II]. In this research maximum likelihood estimation is used to generate 3D source position estimates using a single RMC. The log-likelihood distribution for source plus background and background only scenes is used to calculate search parameters such as the minimum detectable source and to quantify differences between the new universal field model and existing far field models.

3. Extended sources are simulated and fully resolved images are generated using a single RMC as opposed to multiple RMCs. This is accomplished by changing the separation distance between the masks during a simulated measurement. Also a simple change in the mask design removed a 180° source ambiguity created by symmetric masks. This eliminates the need to make at least two RMC measurements at different locations.

4. An adaptive sampling scheme is considered as a method for improving the rate at which an orphan source can be detected. Also a method is devised for computing the detection limits for a given RMC configuration and fixed sampling time.

5. The precision of the MLEM estimates are measured for sources across the field of view and at different depths. A bootstrap resampling technique is used to compute the standard deviation of the source activity and position estimates.

6. The performance of the RMC when multiple point sources are in the near- to mid-range is evaluated. Measurements of the angular resolution demonstrate that the resolution is a function of the separation distance between the source and the detector. Additionally, the measured angular resolution using the prototype RMC was better than previously reported theoretical angular resolution predictions.

The improvement is linked to the use of maximum likelihood techniques for parameter estimation and image reconstruction.

1.3 Overview of the Dissertation

This dissertation is broken down into five chapters. The first chapter contains the introduction and provides a motivation for the research. A short review of the research history is presented along with the contributions of this research to the field of study.

The second chapter presents the theory of RMC operations. Several existing far field models are presented as well Sharma's near field model and the new universal field model that is used in this research. The far field and universal field models are then compared using some simulated source scenarios. The second part of chapter two discusses a variety of maximum likelihood methods that are used to produce source activity and location estimates. The final section of chapter two discusses several measures of performance that are used to assess the quality of the RMC images. These measures of performance include the angular resolution, the estimate accuracy and standard deviation, the modulation efficiency, and the dynamic range. Finally a method using log-likelihood distributions is introduced as a way to compare the RMC system to a bare detection system.

The third chapter contains the design information of the prototype RMC used in this research. Specifically considered are the structural design, the mask design, the automation, control, and feedback system design, the data acquisition system design, and methods for system calibration. The last part of this chapter explores two ways to change the RMC operating parameters to enhance system performance. The first study demonstrates that a single RMC can be used to image complex sources when the mask separation parameter is changed during a measurement. The second study looks at an adaptive sampling scheme that is used to modify the RMC sampling profile as data is recorded. The desired result is a reduction in the amount of time required to positively locate an orphan source.

The fourth chapter discusses the performance of the prototype RMC based on measurements and simulations. The first portion of the chapter considers the RMC response to a uniform background field. Then results are shown as the source moves from the center of the RMC field of view to an area outside the field of view. The third part of the chapter looks at several methods for estimating the depth coordinate of the source. The final section of Chapter 4 explores the RMC response when two or more point sources are located in the RMC field of view. Initially the sources are assumed to emit the same energy photon. Results are then presented when the sources emit different energy photons and the effects of down scattered high energy photons on the image quality at lower energies.

The fifth and final chapter summarizes the key finding of this research. Several conclusions are made about the suitability of the RMC for the orphan source search problem as well as recommendations for the future. The last half of chapter five explores future research that can be conducted using the RMC. Among this research is the use of RMC arrays, the development of a better data acquisition system, and advanced mask designs for enhanced RMC imaging.

CHAPTER II

THEORY OF RMC OPERATIONS

The theory supporting rotating modulation collimator operations shares much in common with other indirect mechanical imaging techniques such as coded apertures. This chapter reviews the far field models traditionally used with RMCs and then presents a new system model that predicts the RMC detector response when the source is located at any distance from the detector. This new model not only is necessary for performing image reconstruction in the near field, but it also offers some key insights into the design and operation of a RMC. The focus then shifts to the set of analytical tools used in this research to translate the RMC detector response functions into source intensity and position estimates. Specifically the concept of maximum likelihood as well as the maximum likelihood expectation maximization algorithm will be presented as methods for source parameter estimation. Because these techniques are inherently non-linear, a boostrap resampling technique is implemented as a useful tool for computing the variance on the intensity and position estimate. With regards to the system design, the Fisher information and Cramer-Rao lower bound (CRLB) on the variance are used to explore RMC limits as various system parameters are perturbed. The final portion of this chapter outlines several measures of performance used to assess the results from various RMC measurements and simulations done in this research. Among these measures of performance are the system field of view, angular resolution, modulation efficiency and dynamic range, estimator accuracy, and RMC detection limits.

2.1 RMC Operation

A rotating modulation collimator typically consists of two or more high Z-material masks that are mechanically coupled to rotate together about a common axis as shown in Figure 2-2a. A typical mask pattern is parallel slits that run the entire length of the mask, although this is not the only possible design. When the masks are rotated the projection of the front mask appears to orbit the rear mask with respect to the source. Similarly, one could consider the source orbiting a system of stationary masks as highlighted in Figure 2-1.

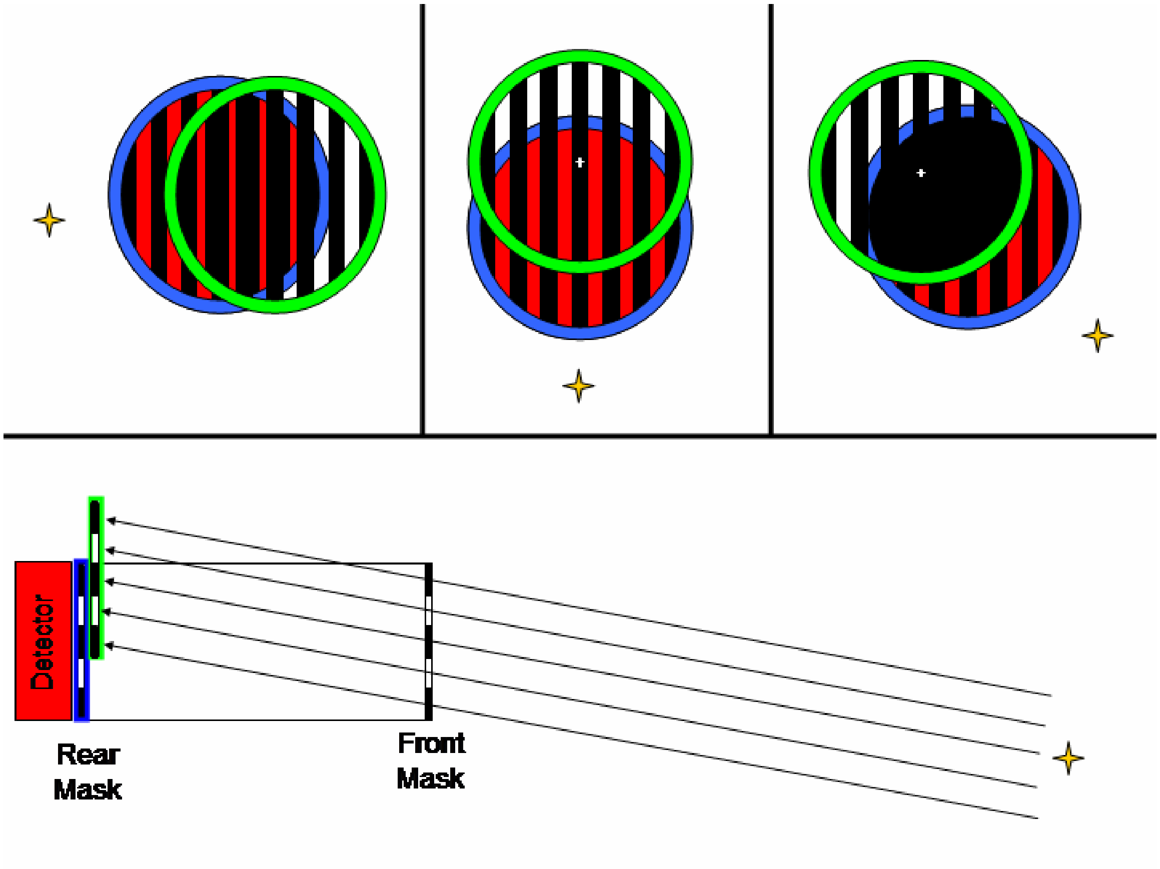

Figure 2-1. The RMC process is illustrated for a far field source as the masks are rotated together (or similarly the source orbits a set of fixed masks). The green circle represents the projection of the front mask and the blue circle represents the fixed rear mask and detector as shown in the lower picture. The yellow star indicates the orientation of the source with respect to the masks. As the masks rotate the slits appear to open and close, creating a modulated pattern.

As the front mask projection moves around the rear mask, the slits will appear to open and close, causing the counts recorded in the detector to be modulated as shown in Fig. 2-2b. One of the defining features of RMCs is that the detector used to record the modulation does not need to be position sensitive. This allows a significant level of flexibility when designing the system as the detector can take on a variety of sizes, materials, or shapes that are optimal for a particular task, while providing high angular resolution with a simple electronic readout.

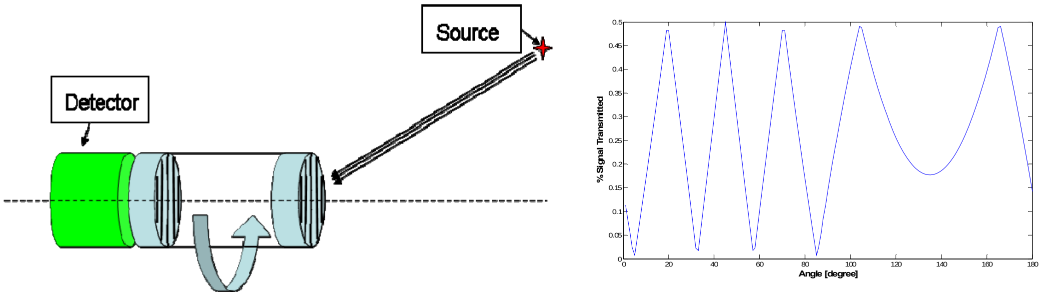

Figure 2-2. (a) One possible configuration of a RMC system. As the mask pair is rotated together, the slit pairs will appear to move across each other for any source located off the centerline axis. This has the effect of either blocking the source or allowing photons to pass to the detector. This produces the modulated detector response seen in (b).

2.2 RMC System Models

The RMC system response shown in Fig 2-2b, is a function of the source location, source strength, non-modulated background, detector efficiency, mask configuration, and the dwell time spent measuring the source at the nth mask rotational position. The number of counts expected to be counted in the nth time bin is the outcome of a Poisson process and can be written as

$$y_n = Poisson\left\{\tau_n\left[\alpha \cdot \varepsilon(E)\cdot \frac{\Omega(\rho,\phi,z)}{4\pi}\cdot\left[P_n(\rho,\phi,z)+P^C{}_n(\rho,\phi,z)\cdot\lambda(E)\right]+b(E)\right]\right\}, \quad (2.1)$$

where τ_n is the dwell time, α is the source activity in Becquerel [Bq], P_n is the probability that a photon emitted isotropically from a location ρ,ϕ,z (cylindrical coordinates) and incident on the RMC masks will pass through an open slit in the masks and hit the detector, ε is the energy dependent detector efficiency, $\Omega/4\pi$ is the solid angle subtended by the front mask of the RMC from the source, and b(E) is the energy dependent background rate in counts per second. The complement of the mask transmission probability P^C_n, multiplied by an energy dependent attenuation factor is the probability that a photon incident on the RMC masks is incident on a blocked element but passes through to the detector. The characteristic RMC saw-tooth pattern is produced by the transmission probability P_n, which is a non-linear function that is directly influenced by the system design and therefore the single most important parameter that can be adjusted to enhance performance for a particular task. The next section examines several methods used previously to generate these probabilities.

2.2.1 Far Field Models

Nearly all studies of RMCs to date have focused on operations in the far field. By definition, when a source is in the far field, all photons that are incident on the RMC will pass through the slits as parallel rays. There have been a variety of far field models proposed for computing the detector response as a function of source location for RMCs, all of which produce similar modulation patterns for a given source position and intensity [Mer67,Sch68,Sch70,Wil70,Huf02]. For simplicity the following assumptions are often used: the masks have no thickness, the masks are completely opaque, and the mask patterns have an infinite extent.

For the purposes of this research, two far field models were considered. The first model developed by Wilmore was selected because of its straightforward and systematic approach to developing the mask transmission function [Wil70]. Wilmore recognized that the probability that a photon incident on a periodic black mask of infinite extent, will be transmitted as a function of position on that mask, can be written as the binary periodic function,

$$\begin{aligned} M(x) &= M(x+p) \\ &= 1 \quad c \le x < c+w \\ &= 0 \quad c+w \le x < c+p, \end{aligned} \tag{2.2}$$

where p is the pitch between slits, w is the slit width, and c is the offset of the mask from the axis of rotation. In this 1D model (highlighted in Figure 2-3), if the photon encounters an open element it is transmitted to the detector and M(x)=1, while a closed element means the photon was not transmitted to the detector and M(x)=0.

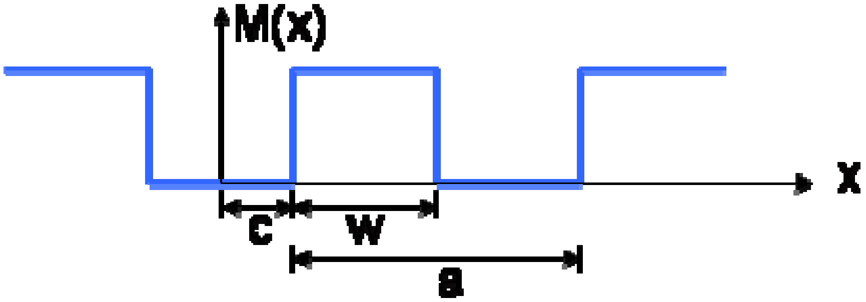

Figure 2-3. A picture of the 1D transmission function used by Wilmore to describe the fate of a photon incident on a 1D black mask. If the photon hits an open element it is transmitted and the function M(x) = 1. If the photon hits a closed mask element it is not transmitted to the detector and M(x)=0. (image reproduced from Wil70)

The function M(x) can be expanded in a Fourier series as

$$M(x) = \frac{w}{p} + \frac{2}{\pi}\sum_{n=1}^{\infty}\frac{1}{n}\sin\left(\frac{n\pi w}{p}\right)\cos\left(\frac{2n\pi}{p}\cdot\left(x - c - \frac{w}{2}\right)\right) \text{ [Wil70].} \tag{2.3}$$

Next Wilmore considered the case of two masks, one located at the detector plane, while the other was parallel to it and separated by a distance L as seen in Fig. 2-2a. In this case, both masks are defined using Eq. 2.3 and can take on different parameters of w, p, and c. The combined transmission of both masks can then be written as

$$\begin{aligned} T(c_1 - c_2) &= \lim_{N\to\infty}\frac{1}{2N}\int_{-N}^{N} M_1(x)M_2(x)dx \\ &= \frac{w_1 w_2}{p_1 p_2} + \frac{1}{2}\sum_{n=1}^{N} A_{n1}A_{n2}\cos\left(\frac{2n_1\pi}{p_1}\cdot\left(c + \frac{1}{2}(w_1 - w_2)\right)\right), \\ &\text{where,} \end{aligned} \tag{2.4}$$

$$A_{n1} = \frac{2}{n_1\pi}\sin\left(\frac{n_1\pi w_1}{p_1}\right),\ A_{n2} = \frac{2}{n_2\pi}\sin\left(\frac{n_2\pi w_2}{p_2}\right),\ \text{and}$$

$$n_2 = n_1\frac{p_2}{p_1}.$$

The transmission function is no longer a function of x, but rather a function of the difference between the offset of the grids, which Wilmore simply defines as T(c). As the masks rotate, the value of c will change, because the position of the projection of the front mask relative to the rear mask is changing as was shown in Fig 2.1.

In the next step, Wilmore recasts Eq. 2.4 into a more useful form as

$$
\begin{aligned}
&T\left(c'\right)=B_0+\sum_{n=1}^{\infty}B_n\cdot\cos\left(\frac{2n\pi c'}{p_1}\right),\ \text{where}\\
&B_0=\frac{w_1w_2}{p_1p_2},\\
&B_n=\frac{4}{n_1n_2\pi^2}\sin\left(\frac{n_1\pi w_1}{p_1}\right)\sin\left(\frac{n_2\pi w_2}{p_2}\right),\\
&c'=L\tan\left(\rho\right)\cos\left(\omega t+\phi\right)+c-\frac{1}{2}\left(w_1-w_2\right),\\
&\frac{2\pi c'}{p_1}=\alpha\cos\omega t-\beta\sin\omega t+\delta,\\
&\left(\alpha^2+\beta^2\right)^{\frac{1}{2}}=\frac{2\pi L\tan\left(\rho\right)}{p_1},\\
&\frac{\beta}{\alpha}=\tan\left(\phi\right),\ \text{and}\\
&\delta=\frac{2\pi}{p_1}\left(c-\frac{1}{2}\left(w_1-w_2\right)\right).
\end{aligned}
\tag{2.5}
$$

In this formulation, α and β are the source coordinates in an arbitrary Cartesian system, ρ and ϕ are the polar radial and azimuthal coordinates respectively, and ω is the angular velocity of the collimators.

Finally, Wilmore inserts the definition for 2πc`/p$_1$ into the top equation of Eq. 2.5 producing his far field model

$$T(t)=B_0+\sum_{n=1}^{\infty}B_n\cos\left[n\alpha\cos\left(\omega t\right)-n\beta\sin\left(\omega t\right)+n\delta\right]. \tag{2.6}$$

This model produces the characteristic RMC pattern and is a function of several of the RMC design parameters such as the slit pitch and width and the mask separation. Furthermore it allows for the first mask to take on different slit parameters than the second mask, which allows Wilmore to make some general statements about mask designs that will produce the best transmission functions. Equation 2.6 is a function of the coordinates α and β in an arbitrary Cartesian system. These can be converted back to their polar equivalents using the relationships provided in Eq. 2.5 [Wil70]. Although not presented in detail here, Wilmore was able to use this same procedure to develop far field models for more complex masks such as a checkerboard pattern, curved slits, and round pinholes.

A second far field model was also studied, although it was not used in the comparative studies presented later in this paper. This model was developed by Hurford et al. for the Reuven Ramaty High Energy Solar Spectroscopic Imager (RHESSI). Huford presents two forms of the model. The first form is equivalent to an earlier model by Schnopper et al., and is given as

$$\begin{aligned} &T(t) = \frac{1}{4}\left(1 + \frac{8}{\pi^2}\cos\left(\Phi\right) + \frac{8}{9}\cos(3\Phi) + \frac{8}{25\pi^2}\cos\left(5\Phi\right) + \cdots\right), \\ &where \qquad (2.7) \\ &\Phi = \cos\left(\frac{2\pi\theta p}{L}\right) \text{ [Huf02].} \end{aligned}$$

Again, p and L are the mask pitch and mask separation respectively, and θ is the angular orientation of the masks with respect to the imaging plane. This model makes several simplifying assumptions like Wilmore, as it does not account for several real RMC design parameters such as mask penetrations by higher energy photons and grid shadowing caused by masks with finite thickness. Huford et al. presents a modified form of Eq. 2.7 to account for these effects, by with the transmission function now represented as

$$T(t) = H \cdot \left(1 + a_1 \cos\left[\Phi - \Psi_1\right] + a_2 \cos\left(2\left[\Phi - \Psi_2\right]\right) + a_3 \cos\left(3\left[\Phi - \Psi_3\right]\right) + \ldots\right). \qquad (2.8)$$

In Eq. 2.8, H is the average transmission through the RMC, while a_i and Ψ_i are the relative modulation magnitudes and collimator phases for the ith harmonic [Huf02]. Huford states for the case of ideal masks seen in Eq. 2.7, the values of H, a_i, and Y_i, are fixed, but when more detailed parameters such as mask penetrations and grid shadowing are considered, they become slowly varying functions in time. The end result is that the sharp triangular modulation peaks produced both by the Wilmore and first Huford model are now represented as sinusoids [Huf02].

Both of the ideal models presented in Eqs. 2.6 and 2.7 produce identical RMC transmission functions for the same point source distributions. The Wilmore model was chosen as the representative far field model in this research because of its straightforward approach, that is somewhat mimicked during the development of a new universal field model.

2.2.2 Near Field Model

Some recent work on RMCs for medical imaging explored their performance in the very near field. Sharma et al. studied the application of a RMC to an imaging technique called neutron stimulated emission computed tomography (NSECT) [Sha07]. For this application, other imaging systems were unsuitable because the source photons are high energy (3-5 MeV) and must be detected with high position resolution. Therefore the RMC was selected as a possible candidate for the task. In this study, measurements were taken in the very near field (10-50 cm source-detector) using a high-purity germanium detector and mask separations ranging from 5-20 cm. Sharma demonstrated that the far field models developed previously were not sufficient to model near field sources and set out to develop a near field model [Sha07]. Sharma's near field approach was a geometric model that defined a region of acceptance as a window defined by the slots and slats of the collimator. The width of the window is given as

$$\ell = \left(S_z - L\right)\left(\frac{w}{t}\right) + L\left(\frac{w}{t}\right), \tag{2.9}$$

where S_z is the separation distance between the source and detector, L is the separation between masks, w is the slit width, and t is the mask thickness. This window of acceptance is pinned to the RMC and as it rotates, any off axis source will only be detected when it falls in the window of acceptance. Outside of this window the collimators appear closed to the source. The resulting transmission function using this model contains only a single peak over a 180° rotation that is centered at the azimuthal coordinate of the source. The width of the peak contains information about the radial coordinate. The geometric model accurately produced the near field transmission functions seen in measurements, but did not include effects such as mask penetrations at high energies or the effects of grid shadowing. Because RMC imaging of NSECT sources required these effects to be modeled, Sharma switched to a Monte Carlo approach to generate the needed transmission probabilities.

2.2.3 Universal Field Model

For orphan source search applications, sources can be located at any range and therefore a new model is desired that is applicable for all ranges. Ideally, such a model should include as many real design parameters as possible, so that when a source is measured, the predicted transmission function will closely approximate the true data. Additionally, the model should remain computationally inexpensive so that transmission functions can be computed rapidly. After studying the various near and far field models and considering possible Monte Carlo solutions, a deterministic numerical approach was selected. This method is based on computing the fraction of the masks that are open as a function of the mask rotation and created by the intersection of the projection of the front mask onto the rear mask and detector. Before continuing it is helpful to define the coordinate system used to define the position of the RMC with respect to the source. Figure 2-4 shows the coordinate system that is used throughout this thesis.

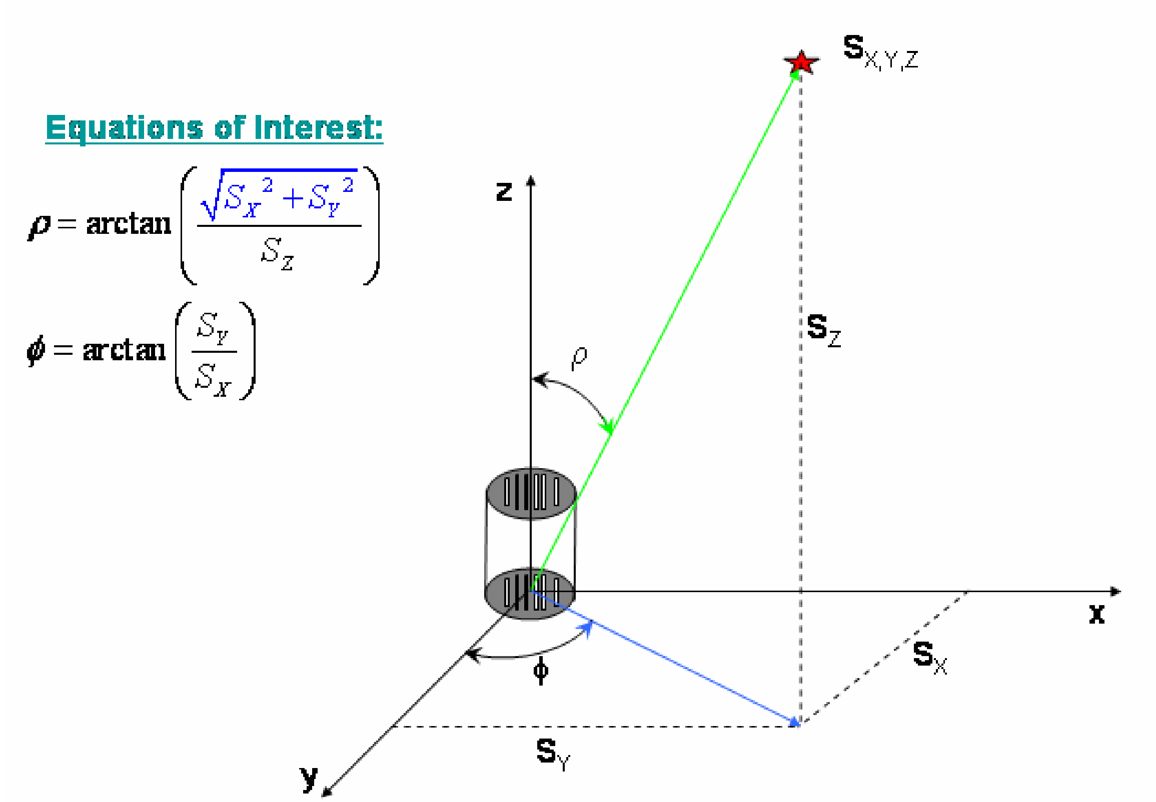

Figure 2-4. The coordinate system used to define the position of the RMC with respect to the source is used throughout this thesis. The polar notation ρ and ϕ are the convention often used in astronomy for sources in the far field. Any source located along the line defined by the coordinates ρ and ϕ will the same transmission function in the far field.

When an object is placed between a source and detector in the near field, the image of the object will be projected and magnified onto the detector face. This same concept applies with RMC projections as seen in Figure 2.5. The source is located a fixed distance S_Z from the detector, the rear mask is against the detector, and the two masks are separated by a distance L. The size of the projected front mask at the detector plane is then simply the magnification

$$M = \frac{S_Z}{S_Z - L} \quad . \tag{2.10}$$

It is also reasonable to consider the back projection of the rear mask and detector onto the top plane of the front mask. In this situation the rear mask and detector are simply shrunk by the factor M and shifted appropriately. Back projection has the advantage that the maximum mask size will be no larger than the front mask, which is useful for the numerical analysis presented later.

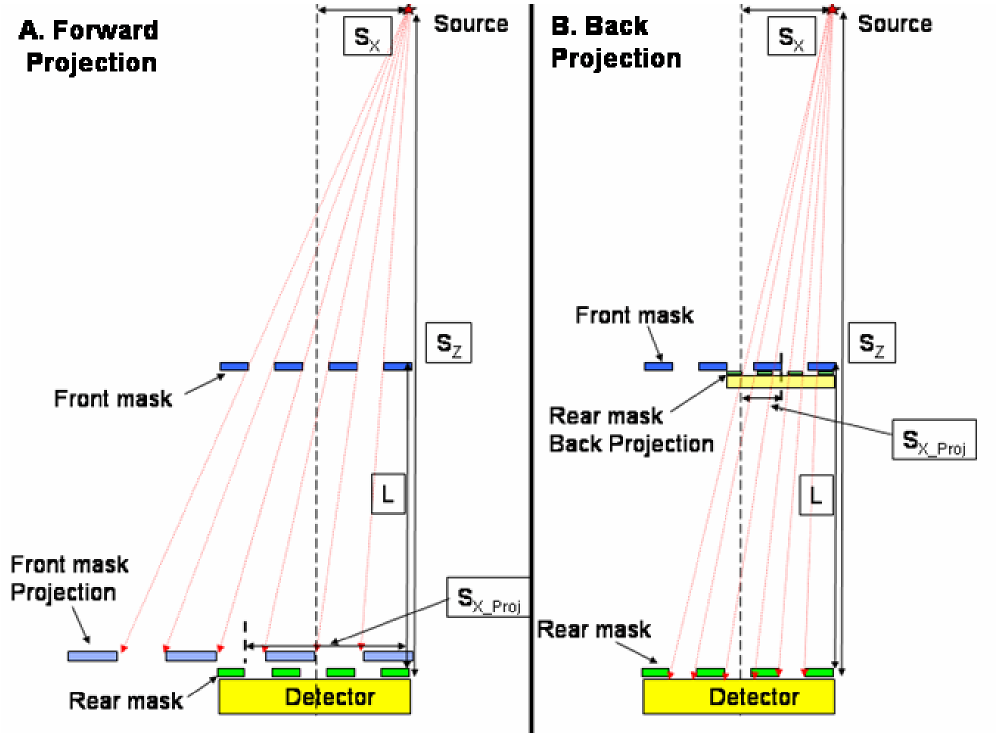

Figure 2-5. When the source is in the near field the forward projection (A) of the front mask is magnified as expected. For the numerical approach taken, it is often easier to consider the back projection (B) of the rear mask and detector up to the top plane of the front mask. Regardless of the direction of projection, both methods produce the same result.

One noticeable feature when looking at Fig. 2-5, is that the open mask elements created by the overlap of the projected front mask and rear mask are no longer uniform, which is the primary reason that far field models are not accurate when used to predict the near field transmission function. The location of the back projected mask centerline with respect to the RMC centerline is given by

$$\left[S_{X\_\mathrm{Proj}}, S_{Y\_\mathrm{Proj}}\right] = \left(S_X - \frac{S_X}{M}, S_Y - \frac{S_Y}{M}\right), \tag{2.11}$$

where S_X and S_Y are the coordinates of the source in the source plane with respect to the RMC axis of rotation. An important note must be made about the quantity M. In the far field, it is often assumed that M=1, however from Eq. 2.11, it is seen that when this far field assumption is made the location of the center of the back projected mask equals zero. This would imply that the model breaks down for far field sources, which is not entirely true. The model in the far field is limited by the number of digits of precision that can be carried when calculating M. For modern computers using 64 bits of precision, this allows the model to still function properly out to ranges on the order of several light years, and therefore is not an issue in this research.

The next step is to consider the behavior of the projected image as the masks are rotated together. The easiest way to think of this is to fix the mask coordinate system in place and instead rotate the source around the axis of rotation as was shown in Fig. 2-1. From this figure it is clear that the number of counts recorded by the detector as a function of the mask orientation will be directly proportional to the fraction of the open area created by the intersection of the two masks. The goal then, is to develop a method to compute the open mask fraction as a function of the mask angular orientation.

At this point it is useful to consider a 2-dimension mathematical definition of a single mask as shown in Figure 2.6. For simplicity assume that mask elements are either open (1) or closed (0) , the mask function is periodic with a period equal to the mask pitch ‘p’, the slots are equal width, and the mask is infinitesimally thin. This follows the same methodology that Wilmore initially used to define the RMC far field model, although in this case the masks are not assumed to have an infinite extent. With these assumptions the transmission function for the front mask can be written as a series of boxcar functions that define the mask elements in x and y,

$$\begin{aligned} G_{front}(x,y) = \sum_{k=0}^{N-1} [\Phi(x+pk+c) - \\ \Phi(x+pk+w+c)] * \\ [\Phi(y+\frac{h_k}{2}) - \Phi(y-\frac{h_k}{2})], \end{aligned} \tag{2.12}$$

where N is the number of slots in the mask, c is the x-coordinate of the left edge of the leftmost slit, w is the width of the slits, p is the slit pitch, h_k is the length of the k^{th} slot, and Φ is the Heaviside function given by

$$\Phi(x) = \begin{Bmatrix} 0 & x < 0 \\ 1 & x \geq 0 \end{Bmatrix}. \tag{2.13}$$

It should be noted that this function can be further generalized by vectorizing the period and slit width parameters and assigning unique values for the k^{th} slit. Thus a mask could be generated with an arbitrary distribution of slat and slit dimensions.

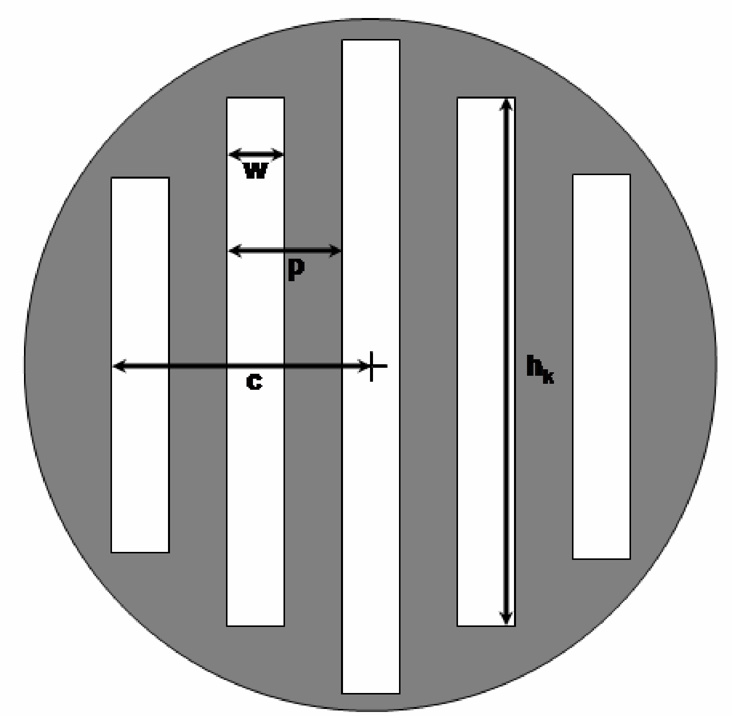

Figure 2-6. This shows the basic pattern for a RMC mask and the required parameters.

The next step is to generate a function for the rear mask $G_{rear}(x)$. The rear mask is defined in the same manner as the front mask, except the parameters used to define the slits, slats, pitch, and slot length must be shrunk by the factor M, due to the back projection for the mask and detector up to the reference plane. With this in mind, $G_{rear}(x)$ can be written as

$$\begin{aligned} G_{rear}(x,y) = \sum_{k=0}^{N-1} [\Phi(x + \frac{pk+c}{M} - S_{X\_\mathrm{Proj}}) - \\ \Phi(x + \frac{pk+w+c}{M} - S_{X\_\mathrm{Proj}})] * \\ [\Phi(y + \frac{h_k}{2M} - S_{Y\_\mathrm{Proj}}) - \Phi(y - \frac{h_k}{2M} - S_{Y\_\mathrm{Proj}})] \end{aligned} \quad , \qquad (2.14)$$

where the argument of $G_{rear}(x,y)$ has simply been magnified and shifted. The transmission function for the combined masks can now be written as their product, and the probability that a photon passes through an open slit is

$$P_n = \frac{\int_{-\infty}^{\infty}\int_{-\infty}^{\infty} G_{front}(x,y) G_{rear}(x,y)\, dx dy}{A_{Det}}, \qquad (2.15)$$

which is simply the ratio of the open slit area to the total area of the detector face (assuming the detector is the same diameter as the masks).

The methodology outlined in Eqs. 2.11-2.15 implicitly makes the assumption that the projection of the front mask will cover the rear mask and detector completely. A review of Fig. 2-1 however, shows that when the two masks are finite and identical only a portion of the front mask will overlap with the rear mask. In this situation Eq. 2.15 now has two components. The first component is the area where the two masks overlap and modulation occurs. The second component is a low frequency contribution related to the modulation from the mask near the detector. If the masks are assumed to have no thickness and are black, the second component will be a uniform additive background to the transmission function that is dependent on the activity of the source and the area of the rear mask that is exposed. If the masks have a finite thickness (discussed in the next section), the rear mask will produce a very low frequency modulation component to the transmission function.

A simple correction is applied by first computing the RMC transmission function for two masks using Eq. 2.15. Rather than dividing by the total area however, the output is scaled by the area of intersection between the two masks. The open area of the single mask is then computed, scaled, and then added to the two mask transmission function. Although approximate, this method will prove to match the measured data very well in Chapter 3.

2.2.3.1 Modeling Mask Thickness

Modeling a mask with finite thickness is a straightforward process with the universal field model. A single thick mask can be represented in the same manner described above for two infinitesimally thin masks. In this case a single mask is defined by a front and rear surface separated by a thickness t, which is now equivalent to the separation parameter L. The equations from above are applied, but an additional constraint is required because the top and bottom of the mask are physically linked. This means that a photon entering a slit at the top of one plane must exit the same slit in the bottom plane. This can be accomplished by constraining Eq. 2.14 so that the projection is only valid when the magnitude of S_{X_Proj} is less than half the grid pitch. When this condition is not met the top plane completely shields the bottom plane and the mask appears closed to the source ($P_n = 0$). In other words, the source has moved out of the single mask field of view. A two mask system with finite thickness masks would then be modeled with four mask planes. A diagram of this process is shown in Figure 2-7.

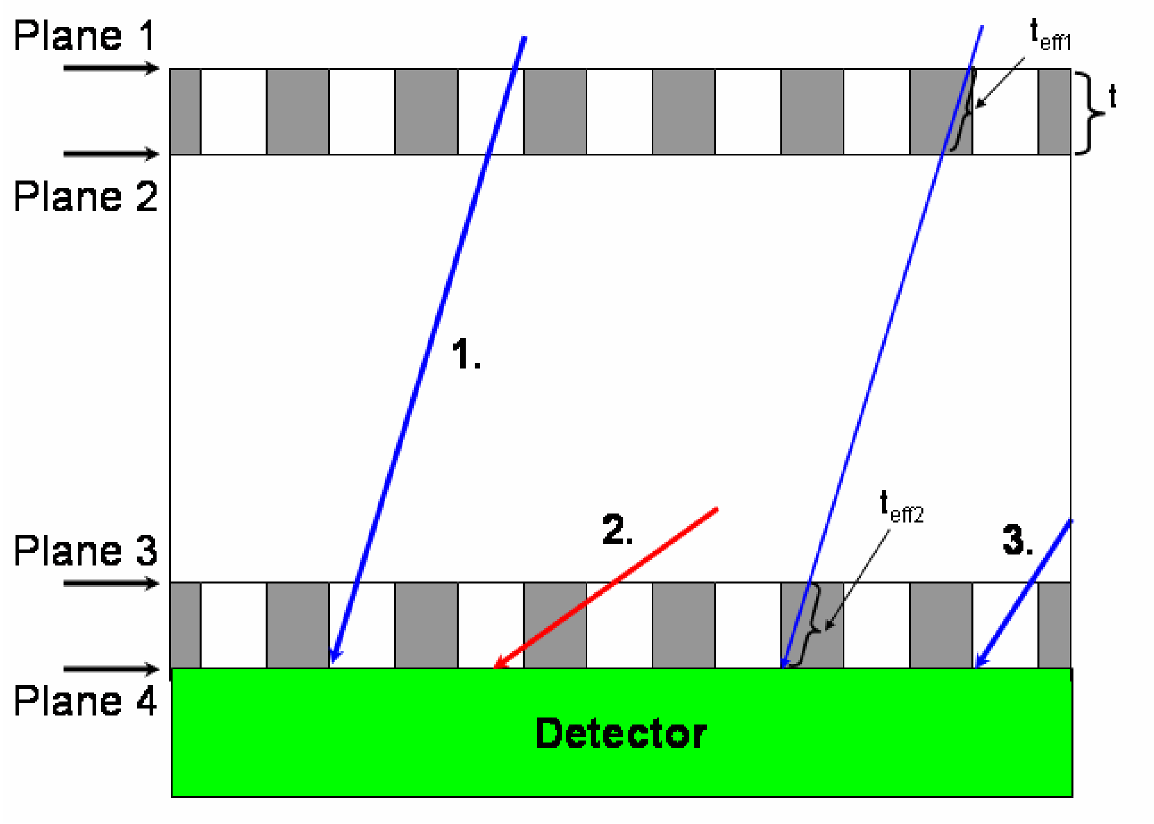

Figure 2-7. This illustrates how the mask thickness is modeled by representing a single mask using the same technique used to define the RMC. Instead of two planes separated by a distance L, there are four planes with the distance between planes 2 and 3 separated by L and the other planes by a distance t. The single mask constraint is understood by comparing photon 1 versus photon 2. The first photon enters the top mask pair in the third slit, but passes through the second slit on the bottom mask. With a single black mask this is physically impossible (see photon 2). For a case like photon 2, the bottom mask would be considered closed and the transmission would be 0.

2.2.3.2 Modeling Mask Penetrations

It is also possible to account for the effects of mask penetrations on the transmission function by considering an energy dependent attenuation parameter λ(E) given in Eq. 2.1. One possible simple assumption is that λ(E) is a constant defined by the thickness and composition of a single mask. In this scenario λ(E) takes on the familiar relationship

$$\lambda(E) = e^{-\frac{\mu}{\rho}(E)\cdot\rho_{mat}\cdot t_{eff}} \tag{2.16}$$

where μ/ρ is the energy dependent mass attenuation coefficient for a specific material, ρ_{mat} is the material density (not to be confused with the polar coordinate given in the definition of P_n in Eq 2.1.), and t_{eff} is an effective mask thickness that is defined by the mask thickness that a beam of far field photons would encounter as a function of the source location (see Fig. 2-7). This model is conservative, because it ignores the fact that near the edges of the slats, the effective mask thickness will be less than this constant value and therefore the photons will experience less attenuation. Additionally, this model assumes a far field source. In the near field the photons will not have the same trajectory and will therefore encounter variable mask thicknesses depending on the position of interaction on the mask and the source location. A possible solution is to compute the distribution of the effective mask thickness across the mask as a function of source position and then using the mean of the distribution. Provided that the edge effects are small this simple model can adequately account for mask penetrations.

2.2.3.3 Computer Implementation of System Model

The RMC transmission function given by Eqs. 2.10-15 can be solved directly using a mathematics software package such as Mathematica, Maple, or Mathcad, although the processing time for several of the functions can be computationally expensive. For this research, an alternative numerical approach is taken using the software package Matlab [Mat07].

The user begins by defining all of the required design parameters such as the number of masks, mask thicknesses, separation distance between masks, slit pitches, slit widths, number and length of slits, mask diameters, etc. These form the input data set for the system model. The reference plane for the system is defined as the mask plane closest to the source (i.e. top surface of the front mask), and is used to compute the magnification factors for the other back projected grid planes (see Fig. 2.5). Once all of the data is input and the magnification factor computed, a length ‘q’ binary grid vector is created for each mask plane using a discretized form of Eq 2.12. The discretization breaks the continuous mask function G(x,y) into ‘q’ equally spaced bins in the x-direction bins across the face of the mask. Each grid vector describes the 1-dimensional transmission through the mask as a function of position on the mask face, where masks elements are either open or closed. Along with each grid vector is a separate length ‘k’ vector that defines the length of each slit in the mask (k is equal to the number of mask slits). Combining these two vectors produces the 2-dimensional map seen in Fig. 2.6 of a single mask plane indicating the positions where photons either pass through or are blocked by the mask. Once these vectors are defined, the total RMC transmission function is computed in a five step process.

(1) The center of each back projected grid is calculated with respect to the reference plane (i.e. top of the front mask) using Eq. 2.11 and the current source position.
(2) Each grid vector is shifted to its new position based on the back projection in step 1, and then each of the binary grid vectors are multiplied together element-wise, producing a new binary grid vector that maps the total transmission through all mask planes.
(3) A scan is performed across the new grid vector to locate the left and right edges of each slit in the combined mask. The top and bottom edges of the slit are determined by comparing the slit length vector for each grid plane and choosing the coordinates that bound the smallest box. These dimensions are then used to compute the area of each slit.
(4) Next the area of all the slits are added together and divided by the total area of the mask, producing the probability for a given source position and mask orientation that a photon incident on the top of the mask system will pass through an open slit to the detector.
(5) Finally, the source is rotated to the next source position simulating the mask rotation and steps 1-4 are repeated. The process continues until the source has moved around the masks a full 360°, producing the complete RMC transmission function seen in Fig. 2.2.b. If the masks are identical and symmetric, only 180° of rotation is required to map the complete transmission function.

There are several strengths and some weaknesses to this numerically implemented model. First and foremost, the model attempts to be very flexible by limiting any assumptions on the mask geometry with the exception that it currently allows only slit/slat features. A modeled RMC system can contain any number of masks and each mask in a system can have unique features from the other masks. The primary weakness is the effect of the grid discretization factor q on the computation time. The size of the discretization factor required for a given system is determined by the width of the mask slits and the magnification given by Eq. 2.10.

2.2.3.4 Computation of Solid Angle

The probabilities calculated using the universal field model only provide the probability that a photon incident on the top of the RMC passes through an open slit and hits the front of the detector. Also required is the probability that a photon emitted isotropically from a point source will be incident on the top of the RMC. This probability is given by the ratio of the solid angle subtended by the top mask of the RMC system and 4π, which represents all possible directions which an isotropically emitted photon can travel. The solid angle for a point source emitted toward a detector can be written as

$$\Omega = \int_A \frac{\cos\alpha}{r^2}\, dA, \tag{2.17}$$

which is the integral over the detector suface facing the source [Kno00]. In this equation r is the length of a vector that extends from a surface element dA on the detector to the source, and α is the angle formed by the intersection of this vector and the detector element plane. For a point source on axis with a right cylinder, this equation is easily solved and takes on a familiar definition. RMC measurements however require that the source be located off axis, which is a more difficult problem. Tryka [Try99] derives a general solid angle formula for a point source incident on a cylinder using elliptical integrals. His formulation breaks the problem down into multiple regions as

$$\begin{aligned}
\Omega(R,\rho,z) &= \Omega_0(R,0,z) \quad z \geq 0, \\
&= \Omega_1(R,\rho,z) \quad 0<\rho < R;\ z \geq 0, \\
&= \pi \qquad\qquad\quad 0<\rho = R;\ z = 0, \\
&= \Omega_R(R,\rho,z) \quad 0<\rho = R;\ z > 0, \\
&= \Omega_2(R,\rho,z) \quad 0 < R < \rho;\ z \geq 0,
\end{aligned}$$

where

$$\Omega_0(R,0,z) = 2\pi\left(1 - \frac{z}{\left(R^2+z^2\right)^{\frac{1}{2}}}\right),$$

$$\Omega_1(R,\rho,z) = 2\pi - \frac{2z}{\left[(R-\rho)^2+z^2\right]^{\frac{1}{2}}} \cdot \left(K(p_P) + \frac{R+\rho}{R-\rho}\Pi\left(q_p, p_P\right)\right),$$

$$\Omega_R(R,\rho,z) = \pi - 2K\left(p_{P,R}\right),$$

$$\Omega_2(R,\rho,z) = -\frac{2z}{\left[(R-\rho)^2+z^2\right]^{\frac{1}{2}}} \cdot \left(K(p_P) + \frac{R+\rho}{R-\rho}\Pi\left(q_p, p_P\right)\right),$$

and the Legendre-Jacobi elliptical integrals are given as

$$\mathrm{K}(\mathrm{p}_\mathrm{P}) = \int_0^{\pi/2} \frac{d\delta}{\left(1 - {p_P}^2 \sin^2\delta\right)^{1/2}},$$

$$K\left(p_{P,R}\right) = \int_0^{\pi/2} \frac{d\delta}{\left(1 - {p_{P,R}}^2 \sin^2\delta\right)^{1/2}},$$

$$\Pi\left(q_p, p_P\right) = \int_0^{\pi/2} \frac{d\delta}{\left(1 - q_p \sin^2\delta\right)\left(1 - {p_P}^2 \sin^2\delta\right)^{1/2}},$$

where

$$\begin{aligned}
{p_P}^2 &= \frac{-4R\rho}{\left[(R-\rho)^2+z^2\right]}, \\
{p_{P,R}}^2 &= \frac{-4R^2}{z^2}, \text{ and} \\
q_p &= \frac{-4R\rho}{(R-\rho)^2}.
\end{aligned} \tag{2.18}$$

In Eq. 2.18, R is the radius of the detector, ρ is a distance from the center of the detector out to the position of the projection of the source onto the detector plane, and z is the distance between the detector plane and the source plane. Note that when ρ=0, the source is located on axis and the formulation is the familiar form that is derived in Knoll [Kno00]. This lengthy expression is set up as a function in Matlab that takes the input variable R, ρ, and z and outputs the solid angle Ω.

The method for combining the transmission function probability P_n and the solid angle probability Ω/4π presented so far is actually an approximation that assumes that the solid angle subtended by each open slit across the mask is fairly constant. When the source moves close to the detector, the solid angle for a slit on one side of the mask may actually be significantly different than for a slit on the opposite side of the mask. To determine whether this effect is significant in the near field, another solid angle formulation was considered.

A precise formulation actually considers the solid angle subtended by each open slit in the mask system from the source. This can be accomplished by computing the solid angle of each open slit using the slit dimensions found in step 3 of the Matlab computer code. Gotoh and Yagi derived the relationship for a solid angle subtended by a rectangular slit oriented parallel to the source plane and separated by a distance z_p as

$$\begin{aligned}\Omega(x,y,z) = {} & \arctan\frac{(x_2-x_p)(y_2-y_p)}{z_p\left[(x_2-x_p)^2+(y_2-y_p)^2+z_p{}^2\right]^{\frac{1}{2}}} \\ & -\arctan\frac{(x_1-x_p)(y_2-y_p)}{z_p\left[(x_1-x_p)^2+(y_2-y_p)^2+z_p{}^2\right]^{\frac{1}{2}}} \\ & -\arctan\frac{(x_2-x_p)(y_1-y_p)}{z_p\left[(x_2-x_p)^2+(y_1-y_p)^2+z_p{}^2\right]^{\frac{1}{2}}} \\ & +\arctan\frac{(x_1-x_p)(y_1-y_p)}{z_p\left[(x_1-x_p)^2+(y_1-y_p)^2+z_p{}^2\right]^{\frac{1}{2}}},\end{aligned} \tag{2.19}$$

where x_p, y_p, and z_p are the coordinates of the source, and x_1, x_2, y_1, and y_2 coordinates represent the left, right, top, and bottom edges of the open slit respectively [Got71].

Finally the two methods are compared to determine at what point the approximation in Eq 2.18 breaks down. For this test a 3.8 cm radius mask is simulated with 4 mm slits and a pitch of 8 mm, and a mask separation of 10 cm. Under these conditions, Eq. 2.18 and 2.19 are consistent until the source is <15 cm from the top plane of the front mask. Because this extreme near field condition is not applicable for the orphan source search task and because Eq. 2.18 is slightly faster than Eq 2.19, it would be possible to just use Eq. 2.18 for all calculations. For the sake of robustness however (and because it is easy to implement), the computer algorithm uses Eq. 2.19 to compute the solid angle when the source is closer than 30 cm from the top mask of the RMC and Eq. 2.18 whenever the source is located further than 30 cm away.

2.2.3.5 Detector Efficiency

The detector efficiency ε(E) is an empirically determined quantity that is dependent on the energy of the gamma ray hitting the detector and the detector material. This quantity represents the fraction of source photons incident on the detector that deposit their full energy into a prescribed energy window. Typically this energy window is set up to bound a photopeak for a given source, and in this case ε(E) is the photopeak efficiency. In this research values of ε(E) are measured by recording the energy spectrum with a known source in front of the detector. The source is removed and a background is measured, which is then subtracted from the energy spectrum with the source. The detector efficiency for a given energy window is then

$$\varepsilon\left(E\right)=\frac{N_{\text{Window}}}{N_{\text{Total}}}, \tag{2.20}$$

which is the ratio of counts measured in the window divided by the total counts in the entire background subtracted energy spectrum. Table 2.1 lists the photopeak efficiency for several sources that are commonly used in this research.

Table 2-1. Listed below are the photopeak efficiencies for three commonly used sources in this research.

	Ba-133 (.356 MeV)	**Cs-137 (.662 MeV)**	**Co-60 (1.17/1.33 MeV)**
$\varepsilon_{pp}(E)$	0.220	0.295	0.121 / 0.104

2.2.3.6 Unmodulated Background – b(E)

The unmodulated background in Eq. 2.1 can be used to account for any additive noise that is present for a given RMC measurement. Ideally, this parameter would only be influenced by a universal uncorrelated background that results from large scale (with respect to the RMC size) environmental processes such as cosmic rays, natural radioactivity in soil, and even large man-made structures such as brick buildings. Because the sources are distributed over such a large area, the probability that multiple photons would be emitted in a small localized area and be modulated is nearly zero. In this regard the background is considered orientation independent since it doesn't matter where the photon originates.

Another contribution to the unmodulated background is from sources (similar to the ones being searched for) that are outside the field of view of the system given by

$$FOV = \frac{d}{L}, \tag{2.21}$$

where L is the separation distance between masks and d is the diameter of the masks. The field of view shown in Eq. 2.21 is the two mask field of view. A single mask field of view also exists, although the imaging capability of a single mask is limited in scope and will be discussed further in Chapter 4. Because the photons from these sources are unmodulated, the transmission function is a constant regardless of mask orientation.

The final contribution to the unmodulated background is an energy dependent effect and comes from high energy photons hitting the masks and losing energy, or only depositing part of their energy in the detector. These down scattered photons then add a background to any lower energy sources that might also be in the field of view. Fortunately it will be shown in Chapter 4 that the down scattered photons are not modulated and are simply an additive process that can be combined in b(E).

The primary difficulty with the background is often it is assumed to be a known quantity for the purposes of position and source intensity estimation. Because the background can be influenced by the same sources included in the search, it is often not possible to know prior to a measurement the magnitude of this parameter. This problem will also be examined more closely using measured and simulated data in Chapter 4 to determine its overall effect on the estimation of the source position and intensity.

2.2.3.7 Comparison of Universal Field to the Wilmore Far Field Model

The first test of model functionality compares the transmission function of a point source for the far field and UM models when the distance between the source and detector is very large. For this study the masks are identical with a pitch of 8 mm and a slit width of 4 mm. The mask separation distance is 24 cm. For a far field source both models should be in agreement, assuming the masks are very thin ($t \approx 0$ mm), as shown in the first two curves of Figure 2-8. As the source moves closer to the detector, the transmission function becomes more compressed in amplitude and stretched in period. For the modeled system, it is seen that the far field approximation is still somewhat appropriate for sources located between 2 and 5 meters from the RMC. When the source moves closer than 2 meters however, the period is stretched so that the peaks are no longer aligned with the far field model and it is at this point that image reconstruction with a far field model becomes less accurate and eventually fails. The stretched transmission functions will also have an impact on the system resolution, modulation efficiency, and dynamic range, which will be discussed later in this paper.

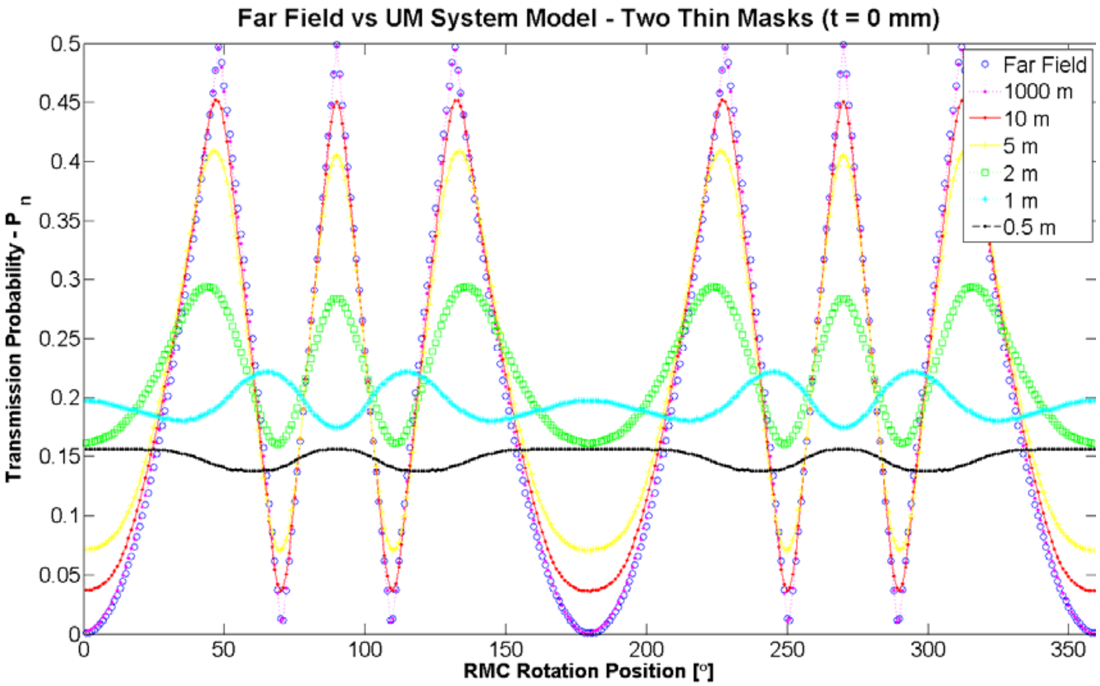

Figure 2-8. Comparison of a point source far field model versus the UM system model at various ranges for two masks with no thickness and a mask separation parameter $L=24$ cm. The source is located at $\rho,\phi = 2.87^\circ$.

The peak compression and stretching is a direct consequence of the magnification at close range. Consider the special case where the top and bottom masks are identical, completely opaque, and the top mask is placed halfway between the source and rear mask/detector. For this special case, the magnification factor equals two and the transmission function is a constant, because the projection of the top mask always shields the same number of lower mask elements regardless of source position. This means that the open slits are the same size for all source positions. Backing away from this limiting case, the transmission functions shown in Figure 2-8 for sources closer than 100 cm are understood. It is therefore seen that an optimal RMC configuration is one where either the magnification is minimized or the mask pattern on either mask is somehow adapted so that the projected front mask matches the rear mask.

Although the universal field model is in good agreement with the far field model when the masks are very thin, there is a significant difference when the mask thickness is modeled. Figure 2-9 illustrates how grid shadowing caused by masks with finite thickness reduces the amplitude of the modulation peaks as well as increasing the width of the large dip. Even the far field source located 1000 meters from the detector produces a slightly different transmission function than the far field model. The effects of mask thickness on the reconstructed image will be discussed further in Chapter 4.

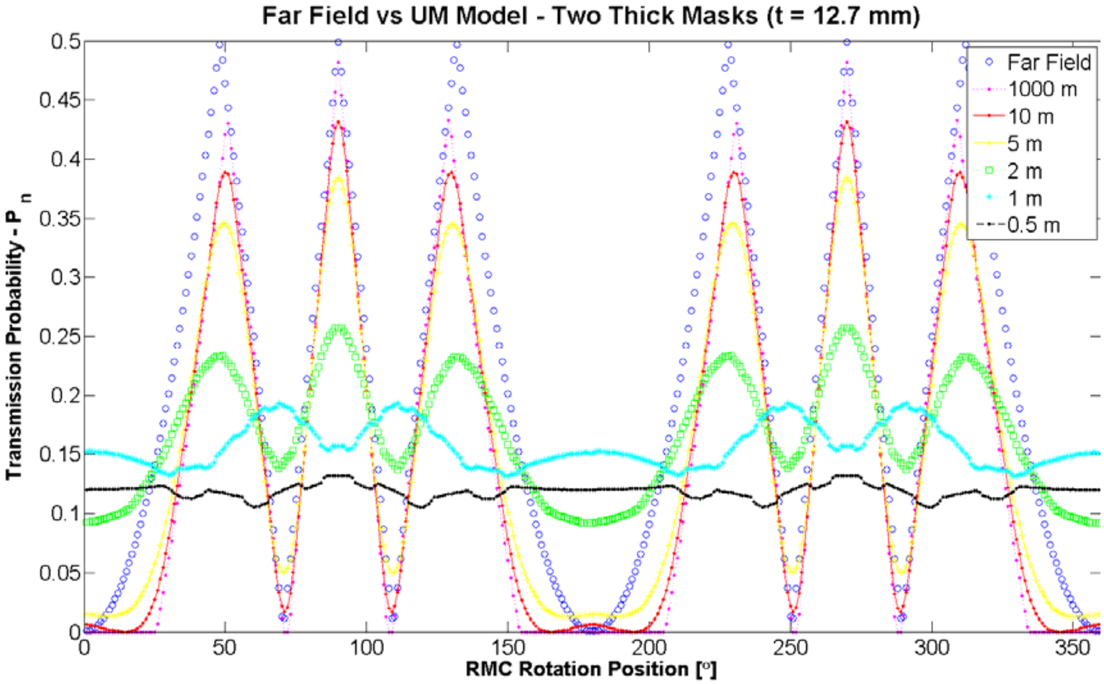

Figure 2-9. The RMC point source transmission function deviates from the far field model when a finite mask thickness is considered. In this case the masks are 12.7 mm thick and the mask separation parameter L=24 cm. The source is located at ρ,ϕ = 2.87°.

2.2.3.8 RMC Response to Complex Source Geometries

Several researchers have studied the RMC response to complex geometries in the far and very near field. Although a single RMC is generally sensitive to point source distributions, it has been demonstrated that a suite of RMCs with different mask properties can be used to image complex objects [Mur89,Fis90,Huf02,Sha07-II]. The implementation of multiple RMCs is not considered for this thesis, but is discussed as a topic of future research. Another method explored further in Chapters 3 is making multiple measurements with different mask separation distances. For now, the focus is on the RMC transmission function that should be expected for more complex source shapes. It has been shown by others, that the transmission function for a complex source can be represented as a superposition of point source responses [Mur89,Huf02]. This is shown in Figure 2-10 for both extended circular sources as well as line sources. The size of the sources are expressed in terms of the theoretical angular resolution given by

$$\Theta = \frac{p}{2L}, \tag{2.22}$$

where p is the pitch between mask slits and L is separation distance between masks. For the plots in Fig. 2-10, the masks have a pitch of 8 mm and are separated by 20 cm resulting in an angular resolution of 1.146°. At a source distance of 214 cm, this translates into a spatial resolution of 4.3 cm. The source position for these models was centered at x,y,z = (0,10,214) cm. The first thing to note from Fig 2-10 is that in both plots, the transmission function is only affected once the extent of the source is greater than one-half the theoretical angular resolution.

When the extended source is smaller than 0.5Θ, it appears point-like to the RMC. Once the source size is on the same order or greater than the angular resolution, the transmission function becomes compressed, because some portion of the source is always visible to the detector regardless of the mask orientation. This is very similar to the near field effect discussed in section 2.2.3.4. For the line source (lower figure in Fig 2-10) there is a slight difference from the extended circular source at the position of the prominent peaks at 0 and 180°. At these points the collimator slits are aligned with the line source and therefore a maximum occurs.

The shapes of these transmission functions are important because they will have an impact on the image reconstruction methods that are discussed in section 2.3. A single RMC measurement of an extended source produces a transmission function that is very similar to the response of a point source. The net effect is that complex sources often reconstruct as a blurred single point source centered at approximately the center of the complex source. Resolving the complex features is accomplished by using multiple RMC measurements taken with different designs. Murphy describes the RMC process in terms of sampling the spatial frequency domain of the image. Resolving a complex image requires that the complete set of measurements adequately samples all of the dominant frequency components of the image [Mur89]. The application of multiple RMCs is discussed in Chapters 3 and 4.

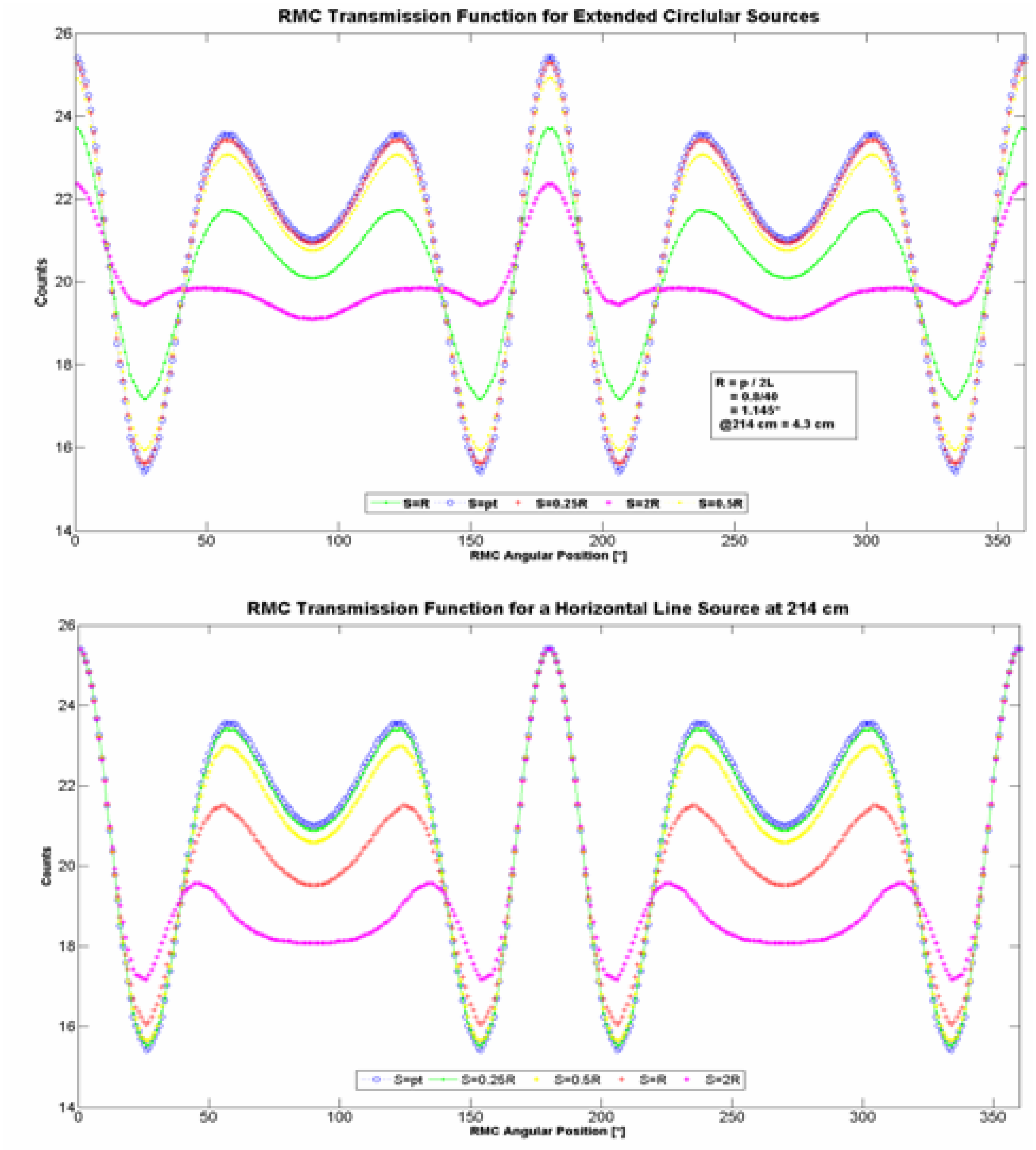

Figure 2-10. The top plot shows the RMC transmission function for an extended circular source, while the bottom plot shows an extended line source. In both cases, the object only appears extended once it is greater than ~0.5 times the angular resolution of the system. Past this point the transmission function becomes compressed, as some of the source is always visible to the detector regardless of the mask orientation. This is very similar to the effect produced when a point source is in the near field.

2.3 RMC Data Analysis and Image Reconstruction

The data measured using a RMC can be thought of as a one-dimensional mapping of a two-dimensional source plane (3D in the near field) and is therefore an indirect measurement of the true source distribution. To translate this one-dimensional signal into a useful position estimate or image, data processing algorithms must be invoked. A variety of data analysis and image reconstruction methods have been applied to RMC data including Fourier analysis, filtered back-projection, and iterative techniques [Wil70,Sch68,Mur89,Huf02,Sha07].

Perhaps the simplest method for estimating the location of a point source given the transmission function is through simple inspection as explained by Gaither [Gai96]. Referring to Figs. 2-8 and 2-9, the estimate of the azimuthal coordinate is given by the location of the low frequency dip. The radial coordinate can be inferred by considering that the geometry of the system fixes the width of each modulation peak equal to the ratio of the slit width and the mask separation. For these images the width of the slits is 4 mm, the separation between masks is 24 cm, and ρ and ϕ are 2.87° and 0° respectively. With this data, the width of a single modulation peak is ~0.955° and there are three modulation peaks between the low frequency dip, which means the radial coordinate of the source is $(3*0.955°) \approx 2.87°$. For real data sets the sources may not be point-like, or there may be more than one source. Additionally, the effects of noise can make the modulated signal very difficult to discern, and therefore other techniques must be employed.

Another technique applicable for point sources is a Fourier analysis technique proposed and used by Schnopper et al. [Sch68]. In this technique Schnopper et al. applies a regularizing function to the transmission function. This regularization takes a transmission function with a non-uniform frequency (see Figs. 2-8 and 2-9) and transforms it into a function with a constant frequency. A Fourier transform of the constant frequency transmission function then produces a peak in the frequency spectrum corresponding to the source location. This frequency peak can then be converted back into polar coordinates. The key is that the transmission function will only become constant when the correct regularizing function is chosen. This method is essentially a search algorithm, where the computer tries a guess at the regularizing function. If it is correct, a peak will appear in the power density spectrum, but if it is not correct the power density spectrum will contain only noise.

Murphy compared the images produced using a filtered back projection (FBP) and a maximum likelihood iterative approach [Mur89]. For simple back projection the number of counts that are recorded at a discrete RMC orientation are back projected onto an image plane. This process is repeated for each discrete angular bin, producing N back projected images corresponding to N discrete RMC angular positions. The superposition of these images produces a peak at the true source position, while suppressing the intensity at other positions. An interesting note about back projection is that it corresponds to the 2-D inverse Fourier transform, blurred by a convolution with 1/r, where r is the radial distance from the source. Filtered back projection removes this 1/r convolution prior to the back projection, so that the final image is equivalent to taking the 2-D inverse Fourier transform [Fis90]. One disadvantage of the FBP approach is it produces ring shaped side lobes, which is problematic in problems with multiple sources or complex source shapes. In these cases, strong sources or source components produce large artifacts that can bury the contributions of weaker sources. These side lobes can be removed using an iterative approach that considers a complex source as a superposition of point sources. For each point that makes up the source, the point source response is computed and then any artifacts related to this response are subtracted [Mur90,Huf02].

Another approach taken by Murphy considers an iterative maximum likelihood (ML) approach which is positively constrained. Murphy's results demonstrated that a maximum likelihood approach produces an image with less noise, no ring artifacts, and therefore greater contrast between strong and weak sources than the FBP and inverse fast Fourier transform (IFFT) techniques [Mur90]. Additionally, Murphy demonstrated that the ML images achieved a higher angular resolution than the back projection method using the same data. Because of the desire for high contrast and high angular resolution in the orphan search problem, a maximum likelihood approach is taken in this research for image reconstruction and source localization.

2.3.1 Log-Likelihood Function, Fisher Information, and Cramer Rao Lower Bound on Variance

The concept of maximum likelihood is extremely useful and commonly applied to many parameter studies. The appeal of ML is that can be applied in a direct approach to many problems and usually produces unique estimators [Her99]. Additionally, for a Poisson model, a ML estimate has a positivity constraint, which ensures that reconstructed image estimates remain physically realistic. Finding a maximum likelihood estimator (MLE) for a RMC system begins by defining the log-likelihood function as

$$\log\left[L\left(\underline{\theta}\right)\right]=\sum_{n=1}^{N}\left[y_n\log\left(\bar{y}_n\left(\underline{\theta}\right)\right)-\bar{y}_n\left(\underline{\theta}\right)\right], \tag{2.23}$$

where y_n is the measured RMC transmission function and $\bar{y}_n\left(\underline{\theta}\right)$ is the expected value of the RMC transmission function provided by the system model in Eq. 2.1 as a function of the unknown parameter vector θ. A more detailed derivation of Eq. 2.23 can be found in Appendix A. In this research the unknown parameter vector $\underline{\theta}$ may include one or more of the following parameters: the source activity 'α', the three position coordinates ρ, ϕ, and z, which are the radial and azimuthal polar coordinates and detector-source distance coordinate respectively, and the unmodulated background.

The MLE is now formally defined as the set of values $\underline{\theta}$, for a measured set of y_n values that maximizes the log-likelihood function or

$$\hat{\theta}=\arg\max_{\theta\in\Theta} L\left(y_n;\underline{\theta}\right). \tag{2.24}$$

As an example of the ML method, consider a problem where the source position is known and the unknown parameter is the source activity α. A data set is measured using a RMC and this data is plugged into y_n in Eq. 2.23. Next the expected value of the transmission function is found by running the universal field model with an assumed value for α. The log-likelihood is computed with this data set. The transmission function is executed again, only this time with a different assumed value of α, which will produce a different log-likelihood value. After several iterations of this process the log-likelihood values are evaluated and the maximum log-likelihood value is selected. The assumed value of α that produced the maximum log-likelihood is the MLE for the measured data set.

An obvious approach to solving the problem at this point would be to set the first derivative of Eq. 2.23 with respect to the each of the unknown parameters in θ to zero, and then solving directly for the unknown parameters. This analytical approach is easier said than done however, because the first derivative for the RMC problem leads to a transcendental equation which is not easily solved analytically. Fortunately there are several numerical methods available that allow the MLE to be computed, which are discussed in section 2.3.2.

Another set of useful concepts related to the log-likelihood function are the Fisher Information and Cramer Rao Lower Bound on the Variance. The Fisher Information, defined as

$$\underline{\underline{F}}\left(\underline{\theta}\right) = -E\left[\frac{\partial^2 \log\left(L\left(\underline{\theta}\right)\right)}{\partial \theta^2}\right], \tag{2.25}$$

provides a measure of the information that the random y_n carries for a chosen set of parameters θ [Kay93-I]. Plugging the log-likelihood function given in Eq. 2.23 into Eq. 2.24 yields

$$\underline{\underline{F}}\left(\underline{\theta}\right) = \sum_{n=1}^{N} \frac{1}{\overline{y}_n\left(\underline{\theta}\right)} \nabla_\theta \overline{y}_n\left(\underline{\theta}\right) \nabla_\theta{}^T \overline{y}_n\left(\underline{\theta}\right), \tag{2.26}$$

which is the matrix form of the Fisher Information for a vector parameter $\underline{\theta}$.

The Cramer Rao Lower Bound on the Variance (CRLB) is a relationship between the Fisher Information and lower bound on the variance of any unbiased estimator, given in matrix form as

$$Cov_{\hat{\theta}} \geq \underline{\underline{F}}\left(\underline{\theta}\right)^{-1} \text{ [Kay93-I].} \tag{2.27}$$

It has been shown that the diagonal elements of the covariance matrix contain the variance bounds for the individual parameters, or mathematically,

$$\operatorname{var}\left(\hat{\theta}_i\right) = \left[Cov_{\hat{\theta}}\right]_{ii} \geq \left[\underline{\underline{F}}\left(\underline{\theta}\right)^{-1}\right]_{ii} \text{ [Kay93-I].} \tag{2.28}$$

The CRLB is a powerful tool for analyzing potential RMC configurations, because it provides the lowest achievable limit on variance for any unbiased estimator for a given system configuration. In this case, the ML principle is especially important, because a MLE will asymptotically approach the CRLB for large data records [Kay93-I]. Additionally, the CRLB depends only on the expected RMC response provided by the system model presented in Eq. 2.1 as a function of the unknown parameters θ. If the system model adequately represents the true system response, then design features in the model can be changed until an optimal system is achieved. This is not a simple task however, as there may be (and probably are) many optimal configurations that depend on the specific objective that the operator is trying to accomplish (e.g. signal detection vs. optimal SNR). Nevertheless, the CRLB can be used to set some general constraints on the system design given some reasonable operating assumptions.

The left two panels of figure 2-11 show maps of the diagonal elements of the Fisher Information matrix across a hypothetical RMC field of view. The right two panels of Fig. 2-11 shows maps of the diagonal elements of the CRLB matrix computed using Eq. 2.28. For this simulation, two identical, completely opaque masks are modeled. The masks have a pitch of 8 mm, a slit width of 4 mm, a thickness of 1.27 mm, and are separated by 25 cm. The map is generated by first creating an N x M system matrix that contains the probabilities that a hypothetical source emitted from the m^{th} pixel of the source plane will be detected in the n^{th} rotational time bin. Therefore, each pixel in the map will have its own (length N) transmission function that describes the detector response as the RMC rotates. The gradients in Eq. 2.25 can be calculated either analytically in the case of the far field models, or analytically and numerically for the universal field model. In the later case, care must be taken to ensure that the pixel spacing is narrow enough so that the gradient of the spatial coordinates which is numerically solved as a 1^{st} order difference between neighboring pixels accurately captures systematic changes as the source moves about the grid. Each pixel in the map of Fig. 2-11 will have a 3x3 Fisher information and CRLB matrix corresponding to the three estimated parameters (source activity, x, and y). The trace of the CRLB matrix contains the variance lower bounds for each of the estimates. That is the $CRLB_{11}$ element contains the lower bound on the variance for the source activity, $CRLB_{22}$ the lower bound for the x-coordinate, and $CRLB_{33}$ the lower bound for the y-coordinate. Because the position estimates have the same units of measure, the CRLB for x- and y- are combined linearly to produce the lower two maps in Fig. 2-11.

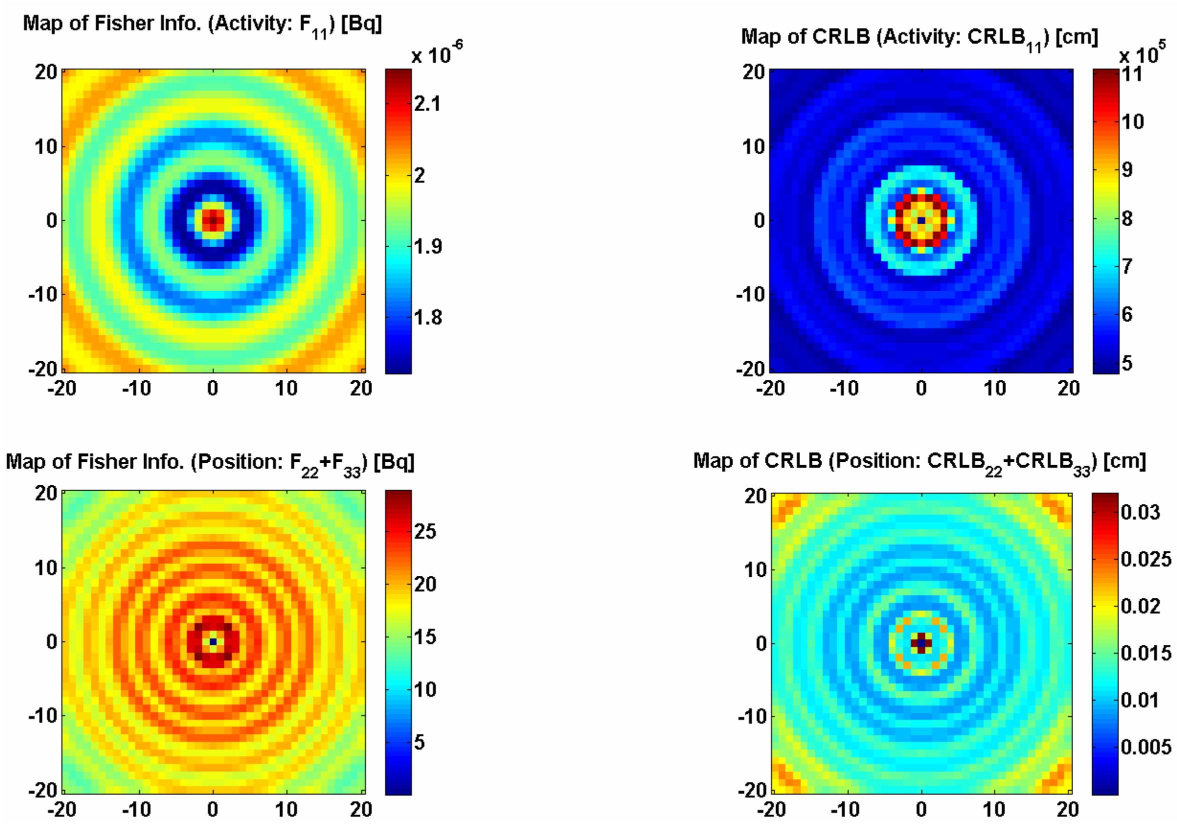

Figure 2-11. These maps show the Fisher information and CRLB for a 2 mCi point source located 250 cm from the RMC. The maps have an expected symmetry, as the information at a given radial coordinate should be the same regardless of the azimuthal coordinate. In the lower right picture, the CRLB at the center pixel has been removed, because it had a value of 10^{12}, which is 14 orders of magnitude greater than the other pixels. This is expected, since the RMC has no sensitivity for sources directly on axis. The values F_{11}, F_{22}, F_{33}, $CRLB_{11}$, $CRLB_{22}$, and $CRLB_{33}$ indicate the location of the estimate in the Fisher Information and CRLB matrices.

Figure 2-11 provides some useful insights into general RMC performance. First as a sanity check on the validity of the figure, the Fisher information for the activity estimate (top left panel) is highest in the center of the image and lowest around the edges simply due to solid angle effects. A point source on axis will emit more photons toward the detector than an off axis source, providing more information on the source intensity. For the spatial estimates, the lower bound on the variance (lower right panel) at the center of the RMC field of view is extremely high as expected. The value at the center of this plot was removed to display the rest of the map. It has a value of 10^{12} Bq, because no modulation occurs for a point source on the rotation axis there is very little information regarding the source location. As the source moves radially away from the center, the variance drops off and then fluctuates slightly out to the field of view edge. It should also be noted that the Fisher information and the CRLB only change as a function of the radial coordinate and are constant in the azimuthal direction. This also is expected, since the only change in the transmission function as a function of the azimuthal coordinate is a phase shift in the data. One would not expect this phase shift to have any impact on the information content of the transmission function. This is a useful property for further system analysis, since it means that the Fisher information and CRLB only need to be computed along the radial direction as opposed to a complete map to characterize system performance. Finally, this figure illustrates that the RMC tends to perform less well for sources located in a broad region around the center for all estimates. The fluctuations as a function of the radial coordinate also imply that the overall performance for a given RMC system will be dependent somewhat on where the source is located.

2.3.2 Estimation of Source Parameters Using Log-Likelihood and Maximum Likelihood Expectation Maximization

The most straightforward numerical approach to finding a set of MLEs for the RMC system is a simple brute force method. For a two dimensional position estimation of the polar coordinates ρ and ϕ, the source plane at a known distance is mapped into a discrete number of pixels. The next step is to compute the log-likelihood function for each pixel in the map using Eq. 2.23 using a measured data set and the transmission function associated with the pixel where the log-likelihood is computed. The final map will contain a log-likelihood value for each pixel. Once the log-likelihood map is created, the MLE of the position coordinates is given by the location of the maximum pixel in the map. Estimating the activity or depth position with this method requires further discretization of the problem in the desired dimension. For example to estimate the distance of the source to the system requires setting an upper and lower bound on the possible source distances and then dividing that up into a set of discrete imaging planes. Figure 2-12 shows how this approach is applied for a single 200 μCi point source located at (x,y,z) = (10,0,300) cm. In this figure the x- and y- dimensions are discretzed into 1 cm x 1 cm pixels, the z- dimension into 4 planes at 100, 200, 300, and 400 cm, and the activity into three bins of 100, 200, and 300 μCi. As expected, the MLE occurs in the 3rd row and 2nd column, when the system model and actual data match. This is highlighted by the red box in Fig. 2-12. It should be noted that each image shown in Figure 2-12 is actually the average image of 100 realizations generated by applying the bootstrap procedure described in section 2.4.3. Without this step, it would be possible to identify a peak in one of the other images as the MLE, because the variance on any one realization is high and the log-likelihood values are close together in magnitude.

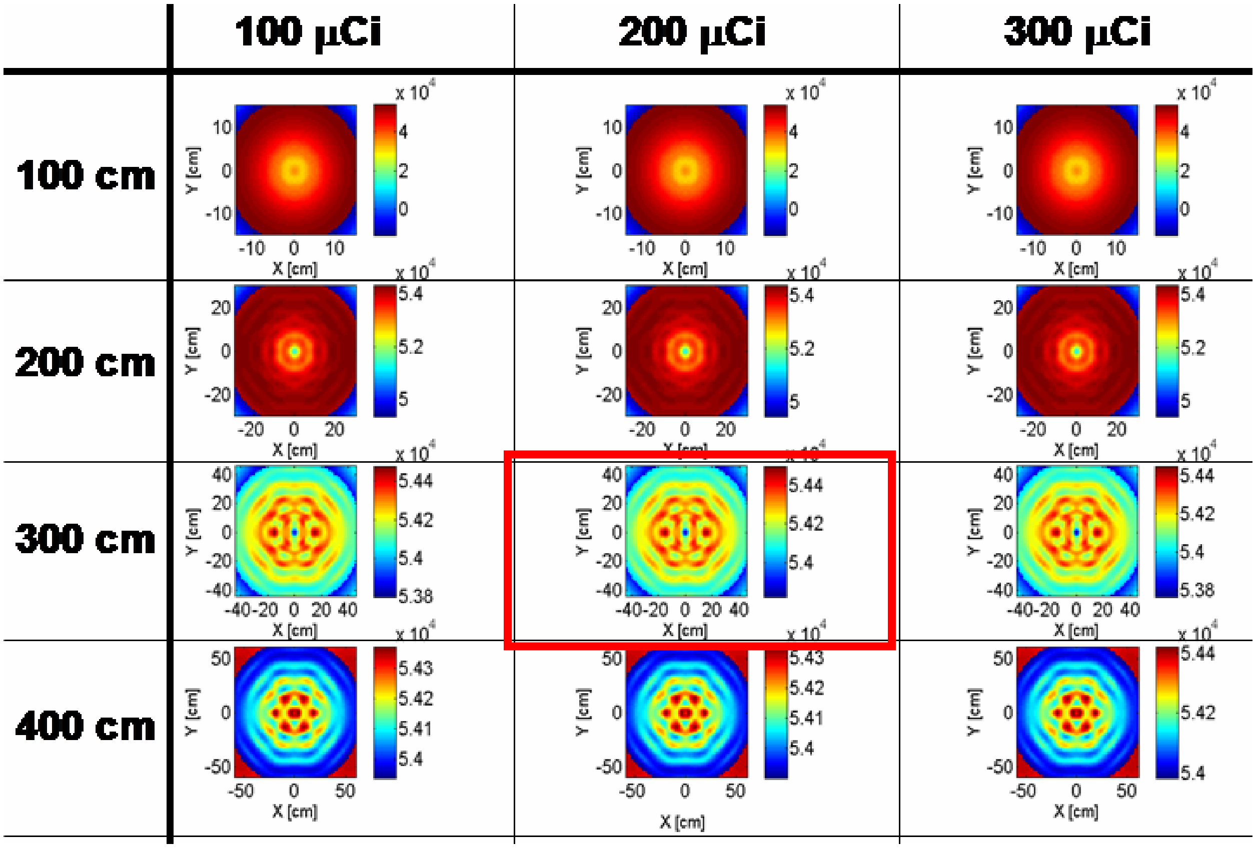

Figure 2-12. Shown here are maps of the log-likelihood function as a function of the three spatial coordinates x,y,z, and the source activity. The MLE for all of the images occurs at x,y,z = (10,0,300) cm and α = 200 μCi, given by the image in the 3rd row and 2nd column (shown in the red box). The MLE matches exactly with the true source coordinates and activity.

Obviously the brute force method outlined above is not practical in any sense for the orphan source search problem, as it would require the generation of many maps and then an algorithm to search through them to locate the MLE. Fortunately there are non-linear optimization programs available that can perform the search in a much more optimal fashion. For this task the Matlab function ‘fmincon’ is used with the log-likelihood function to find the parameters that produce the MLE. [Mat07]. The function ‘fmincon’ attempts to solve

$$\begin{aligned} &\min_{\underline{\theta}} f(\underline{\theta}), \text{ constrained by} \\ &c(\underline{\theta}) \le 0; \quad c_{eq}(\underline{\theta}) = 0 \\ &\underline{\underline{A}} \cdot \underline{\theta} \le b; \quad A_{eq} \cdot \underline{\theta} = b_{eq} \\ &lb \le \underline{\theta} \le ub, \end{aligned} \tag{2.29}$$

where c and c_{eq} are functional constraints and A, A_{eq}, b, b_{eq}, lb, and ub are matrices and vectors containing the parameter constraints. For the RMC problem, the user supplies f(θ), which is the negative of the log-likelihood function, the lower (lb) and upper (ub) bounds on the unknown parameters, and a vector θ_0 containing an initial guess for the values of the parameters. As an example of the upper and lower bounds, it might be reasonable to state that the activity estimate will be bounded by a pre-determined minimal detectable activity (MDA) and a reasonable upper bound (i.e. < 10 mCi). The radial coordinate will be bounded by some finite distance out from the RMC center (due to a blind spot discussed in Chapter 4) and the field of view edge given by Eq. 2.21. The azimuthal coordinate can take on any value since it is a periodic function and can be unconstrained. Finally the depth coordinate might be bounded by the depth of a particular object that is being scanned, or a predetermined range of interest for the orphan source search.

Once these constraints and initial guesses are input, the algorithm computes gradients of the parameterized function and searches for a local minimum. The mechanics of the algorithm are actually more complex than this simple statement, but they are beyond the scope of this thesis and can be referenced in the Matlab online help guide [Mat07]. It can be stated however, that given a reasonable set of inputs the algorithm does indeed locate the MLEs for the unknown parameters.

Some extra attention must be given to the vector of initial guesses for the unknown parameters. This initial guess is very important for RMC estimation and can be understood by again referencing Fig. 2.12. Assume that in a particular application the source activity and depth position are known (200 μCi and 300 cm) and the two polar coordinates ρ and ϕ are unknown (a 2D search on the image in the 3rd row, 2nd column in Fig. 2.12). Because this image has several peaks and valleys, it is very likely that an initial guess of the position far from the true position will result in a local minimum that is not the MLE of the image. The same can also be said if the upper and lower bounds are not selected with some care as a large search region will increase the chances that the algorithm will encounter a local minimum that is not the MLE. This highlights a larger problem with this technique however, since it is apparent that the algorithm needs some a priori information to produce the true MLE. Another method must be introduced that can help bound the problem appropriately.

Fortunately another such method does exist that is also based on the maximum likelihood principle. The maximum likelihood – expectation maximization (MLEM) algorithm is a well known iterative method that has been used on a wide variety of estimation problems and was first applied to radiation imaging problems in a well known paper by Shepp and Vardi [She82]. Kay presents a good overview of how the MLEM method works [Kay93-I]. The underlying theory is that in the imaging problem the user would like to generate a MLE image, based on a set of recorded data. Unfortunately finding this estimate for the entire image requires a large multidimensional optimization, which is not easy to solve. It can be simplified however, by recognizing that the complete image can be decomposed into the individual pixels that make up the image. Assuming that this decomposition is linear, the estimation can be performed pixel by pixel and the combined estimates produce the MLE for the entire image [Kay93-I]. The benefits to using a MLEM method are numerous. It is positively constrained, the algorithm has been shown to converge, produces at least a local maximum on convergence, and increases the likelihood at each step [Kay93-I].

The MLEM algorithm is traditionally given as

$$\lambda_j^{n+1} = \frac{\lambda_j^n}{\sum_i a_{ij}} \sum_i a_{ij} \left(\frac{y_i}{\sum_k \lambda_k^n a_{ik} + b_i} \right), \tag{2.30}$$

where λ is the MLE, a_{ij} is a system matrix that contains the probabilities that a photon emitted from the j^{th} pixel is detected in the i^{th} RMC mask position, y is the measured RMC data, and b is the unmodulated background.

Equation 2.30 can also be written in matrix form as

$$\underline{\lambda}_{n+1} = \underline{\lambda}_n .* \underline{\underline{A}}^T \left[\underline{y} ./ \left(\underline{\underline{A}} \underline{\lambda}_n + \underline{b} \right) \right] ./ \underline{a}, \tag{2.31}$$

where A is the same system matrix as a_{ij} in Eq. 2.30, and the vector 'a' is simply a map of the 2D system matrix 'A' into a 1D vector using

$$\underline{a} = \underline{\underline{A}} \underline{I}, \tag{2.32}$$

where I is a length N row vector of ones. The ./ (or .*) notation in Eq. 2.31 is used to denote division (or multiplication) element by element.

The two formulations in Eqs. 2.30 and 2.31 are equivalent, although Eq. 2.31 takes advantage of modern computer programming conventions to solve this linear system more efficiently. In the above equations, there are several variables that must be predetermined before the MLEM algorithm can be implemented. The first parameter defined in the MLEM algorithm is the system matrix 'A', denoted by a_{ij} in equation 2.30. 'A' is an N x P matrix that contains the probabilities that a photon emitted from the j^{th} source pixel is detected when the masks are in the i^{th} rotational position. Therefore, each column of 'A' contains the RMC transmission function that would be produced if the source were located in the j^{th} pixel. The data vector y, is a length N vector that contains the measured RMC counts. The vector b is a length N background vector, and contains the assumed background value for the measurement. The final parameter is λ, which is the MLE of the source plane, where the j^{th} element of λ contains the source intensity estimate for the j^{th} source. Typically λ is initialized so that all of the pixels have a value of one. As the algorithm iterates the values in λ will converge toward at least a local minimum. When a source is present, this will ideally result in a sharp peak in the image consistent with the true location of the source. Figure 2.13 shows the transmission function and corresponding MLEM image for a point source located at x,y,z = (15,15,250) cm.

One problem encountered with RMC imaging and the MLEM algorithm is that the system is typically under determined. As an example, consider a coarse mask design where the pitch is 8 mm, slit width is 4 mm, and the mask separation is 25 cm, the theoretical resolution is ~0.92°, and the field of view is ~16.9°. When the source is 500 cm from the system, this translates to an ~8 cm resolution and 152 cm diameter field of view. Dividing this area into 8 cm pixels produces a 20x20 grid, or 400 pixels total. Now, assume a RMC sample is measured every 1° of rotation, producing 360 total samples. This means that the MLEM algorithm will be attempting to solve a problem for 400 unknown pixels, with just 360 known measurements. It is actually worse however, because the 360 known values are not linearly mapped to the 400 unknown pixels, but are instead a 1D map of a 2D source scene. Of course as the resolution is made smaller and a depth dimension is added, the system becomes even more under determined which can lead to poor estimates. Sharma used MLEM for image reconstruction, and studied the effects of the under determinedness on the resulting images [Sha07-II]. She found that for very small pixels the resolution was poor due to the similarity of the transmission function from pixel to pixel. Increasing the sampling frequency to collect more data points had no impact on improving this resolution.

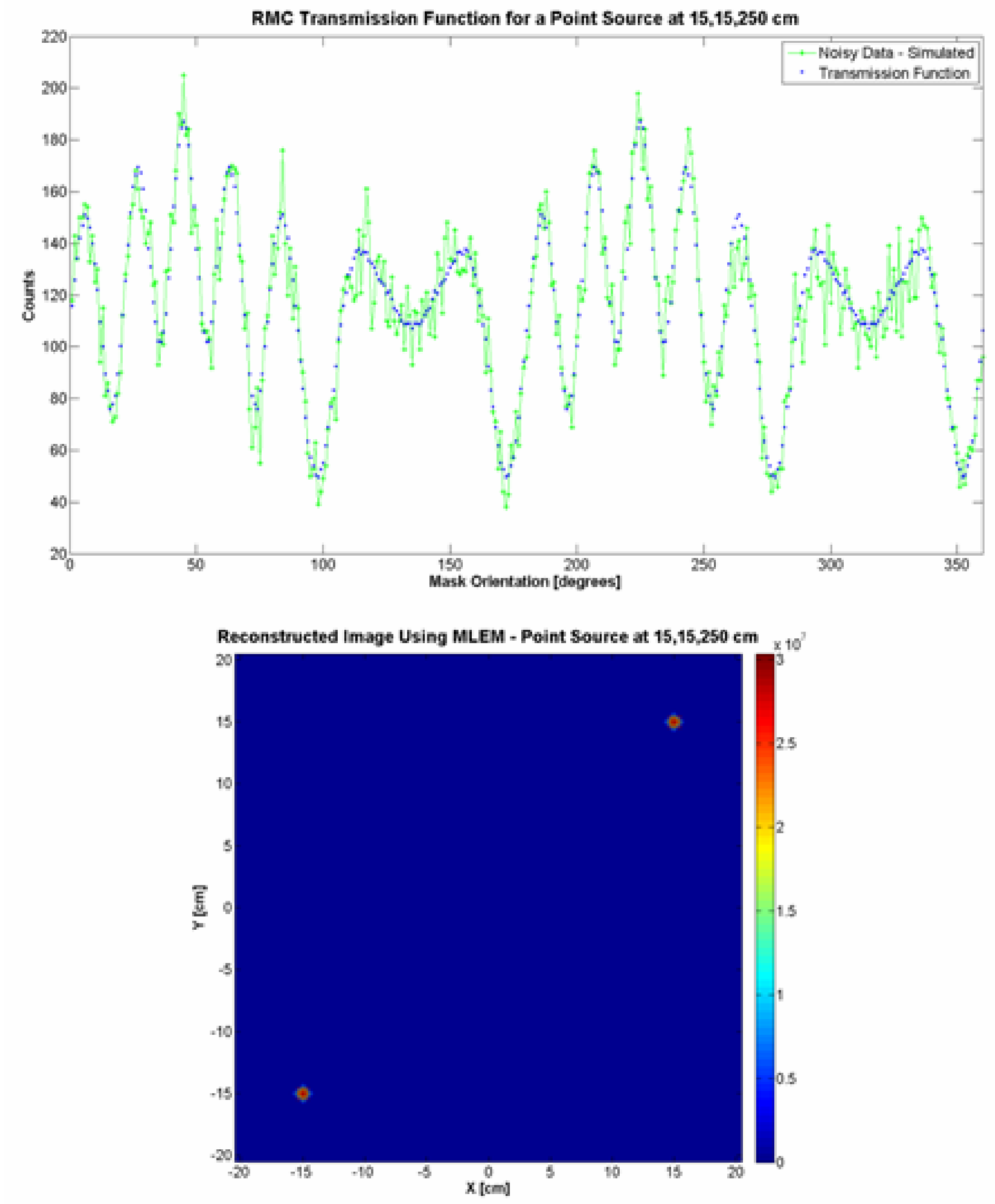

Figure 2-13. This is the RMC transmission function and associated MLEM reconstructed image for a point source located at x,y,z = 15,15,250 cm. The 180° ambiguity results from the symmetric nature of the transmission function. This ambiguity can be resolved by making a second measurement at a different position as proposed by several authors. Alternatively the ambiguity can be resolved by modifying the mask design so it is no longer symmetric. This will be discussed further in Chapter 3.

2.4 RMC Indicators of Performance

The first three sections of this chapter described how a RMC operates, the models used to predict the RMC transmission function, and finally the data analysis and reconstruction algorithms used to generate source strength and position estimates. In this final section, the focus is turned to several figures of merit and measures of performance used to describe the quality of these estimates. These are the tools that will be used with the simulated and measured data in chapters 3 and 4 to make some generalized statements about the suitability of specific RMC configurations as well as RMCs in general to the orphan source search problem.

Several figures of merit (FOM) are often quoted when comparing RMC systems. The system field of view and resolution given by Eqs. 2.21 and 2.22 are the first of these FOMs. Moving the masks close together provides a large field of view which is beneficial, but only at the expense of the angular resolution.

2.4.1 System Angular Resolution, Depth Resolution, and Point Spread Function

The angular resolution is a measure of the system's ability to properly discriminate two or more independent sources within the field of view from each other. Equation 2.22 describes the angular resolution in terms of the pitch between mask slits and the separation distance between masks. This equation can be analyzed via measurements and simulation, using the universal system model developed in section 2.2. Figure 2-14 provides insight into the angular resolution, but showing how the combined transmission function of two separated point sources appears as a function of separation distance.

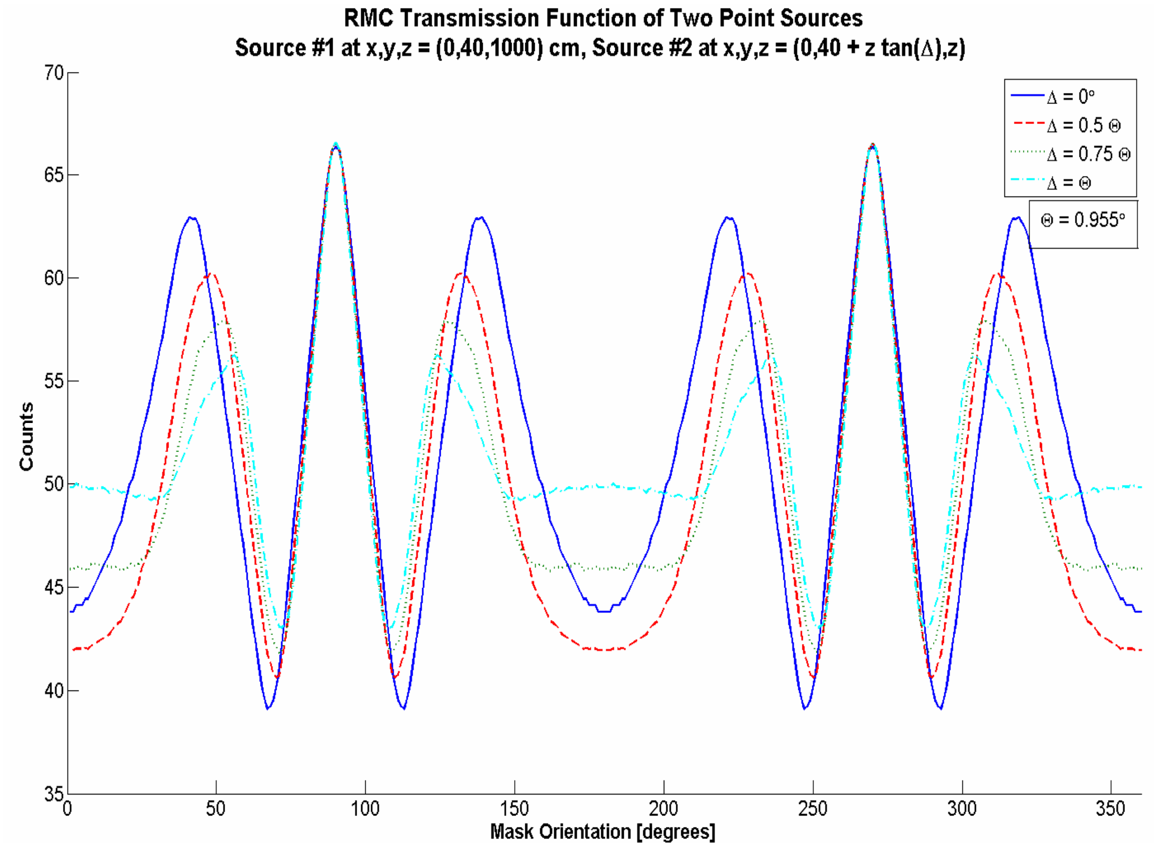

Figure 2-14. The transmission function of two point sources as recorded by a single RMC can be useful for understanding the angular resolution. In this simulation, the theoretical resolution, Θ, is 0.955° shown by the cyan curve. When the source separation is less than 0.5Θ the two sources are not resolved as two independent points.

When the point sources are co-located the transmission function is identical to the single point source response (with more counts) as expected. When the sources are moved apart a distance less than the 0.5 times the theoretical resolution (0.955° in this simulation), the transmission function retains the characteristics of a single point source and the reconstructed image reflects a point source. At some separation distance between 0.5Θ and 0.75Θ, the transmission function begins to take on a shape that is characteristic of two point sources. It is at this point that the two sources can be resolved using the MLEM algorithm. The angular resolution can be measured or simulated, by separating two sources and then finding the distance at which the images are completely resolved. This method is applied in chapter 4 to characterize the system resolution for the prototype RMC.

2.4.2 Modulation Efficiency and Dynamic Range

A third FOM is the modulation efficiency, which is a measure of the difference between the maximum and minimum peaks in the transmission function and is given as

$$\eta_{\text{mod}} = 1 - \frac{\min(y_n)}{\max(y_n)}, \tag{2.33}$$

where y_n is the number of counts measured in the n^{th} discrete rotational bin and is described in more detail in equation 2.1. As shown previously in Fig. 2-10, the modulation efficiency is affected the size of the source with respect to the system resolution. For extended sources the transmission function is flattened and the distance between the high and low peaks is reduced. This same effect occurs with excessive magnification when the source is close to the detector. The transmission function becomes compressed and the modulation efficiency is reduced.

The dynamic range is closely related to the modulation efficiency and is quantified by the ratio between the strongest and weakest sources detectable in the field of view. The limiting factors on the dynamic range are the modulation efficiency of the weak source and the noise on the strong source. Because the two transmission functions will be added together, the weak source will be buried if magnitude of the statistical noise is greater than the separation between peaks on the weak source. The unmodulated background also affects the dynamic range. In a high background environment the statistical noise on the data can bury a weaker source, even though the background has no modulation structure.

2.4.3 Estimator Variance Via a Parametric Bootstrap Routine

Any measured quantity should also have an associated variance with that measurement. The estimators that are found using the iterative maximum likelihood methods are no exception, but determining the source intensity and position variance analytically is a difficult prospect due to the non-linear nature of the problem. For problems such as these, a technique was developed known as the parametric bootstrap.

This concept was first introduced by the statistician Bradley Efron and is based on resampling the available data set with replacement [Joh01].

The bootstrap method for a RMC system is very straightforward. Suppose that for a fixed total measurement time t_{total}, the RMC rotates N times. For each complete rotation, a length P vector is created, where P is the number of discrete RMC rotation bins where data is recorded (i.e. $\omega t_{elapsed}=1,2,\ldots,360$ degrees, $\omega \equiv$ angular velocity of RMC, $t_{elapsed} \equiv$ elapsed time). Each of these vectors will be independent identically distributed (IID) with respect to each other. The measured RMC transmission function is the sum of these N vectors in the order they are recorded. The bootstrap procedure resamples with replacement, N of the complete set of vectors and the sum of these resampled vectors produces a new transmission function that is slightly different than the original measured function. A set of MLEs is generated using the original data and also using the resampled data. If the number of bootstrap iterations is Q, there would be Q sets of MLEs, from which the mean and variance can be computed. Increasing the number of bootstrap samples will improve the accuracy of these statistics. This process is outlined in Table 2.2.

Table 2-2. This shows how the data is recorded as the RMC rotates. The final modulation function is simply the sum of all the counts each discrete rotation angle ωt. For a bootstrap technique, a new modulation function T_{new} is created by random resampling of the columns N times and summing the results. R_n represents the RMC transmission function for the n_{th} rotation.

	R_1	R_2	…	R_N	T_{data}
ωt_1	$R_1(\omega t_1)$	$R_2(\omega t_1)$	…	$R_N(\omega t_1)$	∑ row 1
ωt_2	$R_1(\omega t_2)$	$R_2(\omega t_2)$	…	$R_N(\omega t_2)$	∑ row 2
…	…	…	…	…	
ωt_P	$R_1(\omega t_P)$	$R_2(\omega t_P)$	…	$R_N(\omega t_P)$	∑ row P

2.4.4. RMC Sensitivity and Source Detection

A final parameter of interest when studying RMCs is the tradeoff between generating an image and source detection. When the RMC masks are identical with equal width slits and slats and considered completely opaque, an average of 25% of photons incident on the top of the mask will hit the detector over a complete rotation.

To make these comparisons, the log-likelihood function given in Eq. 2.23 can be used to develop a general detection methodology for RMC systems. In this case, the goal is not to provide an estimate of the source location and intensity, but rather to declare that a source is present or not present in the scanned field of view. Of particular interest, is the impact on detection time when an RMC is added to a bare detector. For the bare detector, Eq 2.1 can be re-written as

$$N_{bare} = \tau \left[\alpha \cdot \varepsilon(E) \cdot \frac{\Omega(\rho,\phi,z)}{4\pi} + b(E) \right], \tag{2.35}$$

which is the equation given for detection of a point source found in a detection text such as Knoll [Kno00]. The only difference between Eq. 2.1 and 2.35 is the removal of the RMC transmission probabilities, P_n (they equal 1 for all n).

Equations 2.1 and 2.35 can now be inserted into the log-likelihood equation given in Eq. 2.23 to perform an equivalent system comparison. The measure of performance used to quantify the systems is the receiver operating characteristic curve (ROC), which provides a measure of the false positive and false negative rate of a system. The ROC for both the RMC and bare detection systems are generated using the following method.

1. Assume a known source position and intensity as well as an unmodulated background intensity. Using a particular set of RMC design parameters, simulate the RMC transmission function using Eq 2.1. This function represent $\bar{y}_n(\underline{\theta})$ from Eq 2.23.
2. Next the value for the “measured” data is simulated by using the function generated in step 1 and the Matlab command ‘poissrnd’. This command takes the input value as the mean of a Poisson distribution and randomly samples a new point in the distribution. This process adds statistical counting noise to the data that would be recorded in a true measurement.
3. Use the noisy simulated data from step 2 along with the transmission function from step 1 to compute the log-likelihood.
4. Repeat steps 2-3, by generating a new noisy data set using the same function generated in step 1. The new data will be similar to the last set, but with the noise

distributed differently across the data, and therefore the log-likelihood will be slightly different. When this step is repeated hundreds or thousands of times the log-likelihood values can be plotted in a histogram producing a distribution as shown by the red data in Figure 2.15a.

5. Repeat steps 1-4, but now remove the source from the simulation, so that only the unmodulated background term is present. The histogram of these data will produce the blue background distribution shown in Fig. 2.15a. The overlap between the distributions will determine the true and false positive fractions.
6. The final step is to generate the ROC. This is done by taking a cut line and positioning it near the far left edge of the background distribution. The true negative rate is the number of background events (blue distribution) that fall below the cut line. The true positive rate is the number of source + background (red distribution) events that fall above the cut line. The true positive and true negative rates are used to define the sensitivity and selectivity given as

$$\mathrm{Sensitivity} = \frac{\mathrm{T_{Neg}}}{\mathrm{N_{bkg}}} \tag{2.36}$$

$$\mathrm{Selectivity} = 1 - \frac{\mathrm{T_{Pos}}}{\mathrm{N_{src+bkg}}}, \tag{2.37}$$

where $\mathrm{N_{bkg}}$ and $\mathrm{N_{src+bkg}}$ are the total number of events in the background and source + background distributions respectively.

7. The cut line is then moved a fixed distance to the right and step 6 is repeated. This process continues until the cut line has progressed to the far right edge of the source + background distribution.
8. The ROC curve is generated by plotting the sensitivity against the selectivity. The degree of overlap between the distributions determines the amount of curve in the ROC. When the distributions completely overlap, the ROC is a straight line running from 0,0 to 1,1.

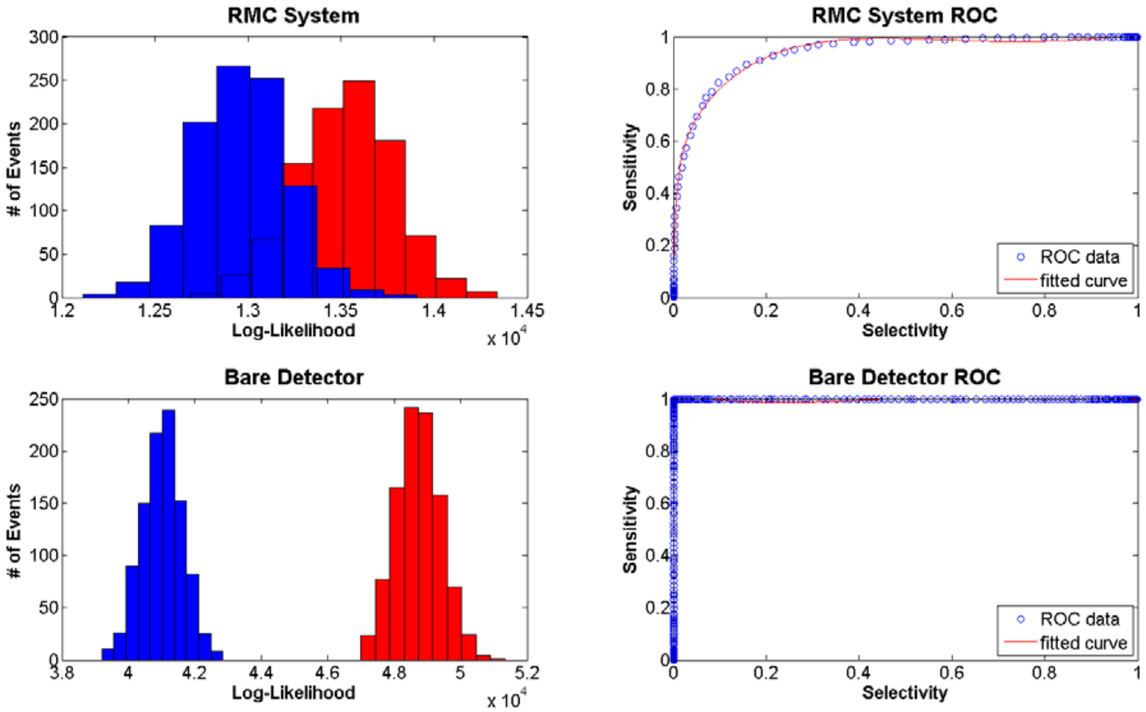

Figure 2-15. The histograms shown above are used to compare the performance of an RMC system against a bare detection system. The red distributions represent the source + background, while the blue distributions are background only. These distributions are then used to generate receiver operating curves (ROC) that are indicators of the separation between distributions. When the two distributions overlap the ROC curves will be a straight line between 0,0 and 1,1. The area under the ROC curve can be used as a metric to compare the two systems.

The same process is also repeated for the bare detector using Eq. 2.23. The results for a particular system are shown in Fig 2.15b. In this research the ROC is a useful tool because the RMC ROC will change with the mask design and operating parameters. A goal is then to search for designs that optimize the RMC ROC so that it moves closer to the ROC of the bare detector, while maintaining good imaging characteristics.

2.5 Summary of RMC Theory

The theory behind the operation of RMCs is very well developed after several decades of research on the subject. Most research has been focused on imaging sources in the far field, with only a small body of work done in the near field. The near field imaging done to date has focused at very close range, and therefore a new model needed to be developed that can accurately predict the transmission function when the source is at a wide array of distances.

Several methods have been proposed and implemented for translating the RMC transmission function to a useful image or set of position and intensity estimates. For this research a maximum likelihood approach was chosen because it has demonstrated superior imaging signal to noise qualities over competing methods such as filtered back projection and other Fourier methods. The drawback to the ML methods are that the likelihood function given the RMC data can have many local minima and maxima, all which make finding the absolute maximum difficult. A MLEM approach is also taken, although this method suffers because the system is generally under determined (more unknowns than knowns). Nevertheless, MLE produced using these methods and the RMC data have so far proven to be very accurate with good noise properties.

Finally, several measures of performance have been highlighted that can be used with the measured and simulated system studied in chapter 4 to assess their suitability for the orphan source search. Among these are the field of view, system angular and depth resolution, position accuracy, dynamic range, and the receiver operating curve. Furthermore, the Fisher information and Cramer Rao lower bound on the variance are powerful tools for assessing several different system designs.

CHAPTER III

RMC SYSTEM DESIGN AND OPERATIONAL PARAMETERS

The design of a rotating modulation collimator system requires consideration of the tasks to be performed by the machine as well as practical physical constraints such as size and mass. For this research, a prototype RMC was designed and constructed to study their performance for imaging and locating terrestrial sources in the mid-range (1-20 meters). This system was also used to validate the universal field model presented in section 2.2. The prototype is designed around a standard 3”x3” sodium iodide (NaI) detector. This size and geometry was selected, because it matches well with several commercially available portable spectroscopic systems such as the ORTEC DETECTIV. Measurements taken with the designed system are then compared against theoretical predictions using the universal field model. These results show that the transmission functions generated by the universal field model match very closely with the measured data.

Along with the system design, it is also important to include a discussion of the some of the different ways in which RMC data can be collected and processed. Previous RMC designs for astronomical observations have relied on a continuously rotating RMC to produce the characteristic transmission function [Sch70,Huf02]. In a terrestrial setting however, it is possible to adaptively change the sampling profile of the RMC by adjusting the dwell time parameter τ in Eq. 2.1. Optimizing τ can help to maximize the amount of information recorded by the RMC, which in turn can increase the accuracy of the RMC image with a shorter sampling time.

For a single RMC system there are several possible degrees of freedom available besides just the mask rotation. Equation 2.32 states that changing the separation between the masks has an effect on the system resolution. There is no requirement that the mask separation remain a constant for the duration of a measurement. The final portion of this chapter explores several of these potential configurations and some limitations useful for operating a RMC system.

3.1 Design Requirements

There are a few universal design requirements for all RMC systems that must be considered during the system design phase. Among these requirements are: (1) RMC structural design including a frame to hold and rotate the masks, (2) the mask design, (3) automation, control, and feedback systems, (4) a data acquisition and processing system, and (5) system calibration.

3.1.1 RMC Structural Design

The RMC structural design for this research is relatively simple. The system, shown in Figure 3.1 consists of an aluminum outer support tube (6” OD) that is set into an aluminum ring mount. Two large bore bearings (5” OD, 4” ID) are pressed and locked into this support tube, and are used to support a second “driver” tube. A timing belt pulley is mounted onto the midsection of this driver tube which is used to transmit power from a motor to rotate the driver tube and a third “flight” tube that contains the masks. The first mask is set into the end of the flight tube closest to the detector locked into place. A second mask is secured in an aluminum carrier that is inserted into the other end of the flight tube. This aluminum carrier can slide freely down the length of the tube until locked in place, and allows for the distance between masks to become a free parameter when imaging (from 0-50 cm for this system). As seen from Eqs. 2.21 and 2.22, this allows the user to change the system field of view and resolution adaptively to sample a given source scene in an optimal fashion.

At the back of the support tube are a set of plastic mounts that can be adjusted to support and align the center of the detector with the center of the RMC masks. When the flight tube and detector are in place, the rear mask is adjacent to the front face of the detector.

It should be noted that in this prototype design the only shielding around the sides of the detector in this design are from the 1” walls of the aluminum support tube. The reasoning behind this decision is that only photons passing through one or both masks will be modulated and produce the signal of interest. Any source outside the system field of view will contribute a uniform Poisson distributed background that is added to any modulated signal. The net effect is more noise added to the modulated signal, which can reduce the dynamic range and maximum achievable angular resolution. These background effects are considered more carefully in section 4.1.

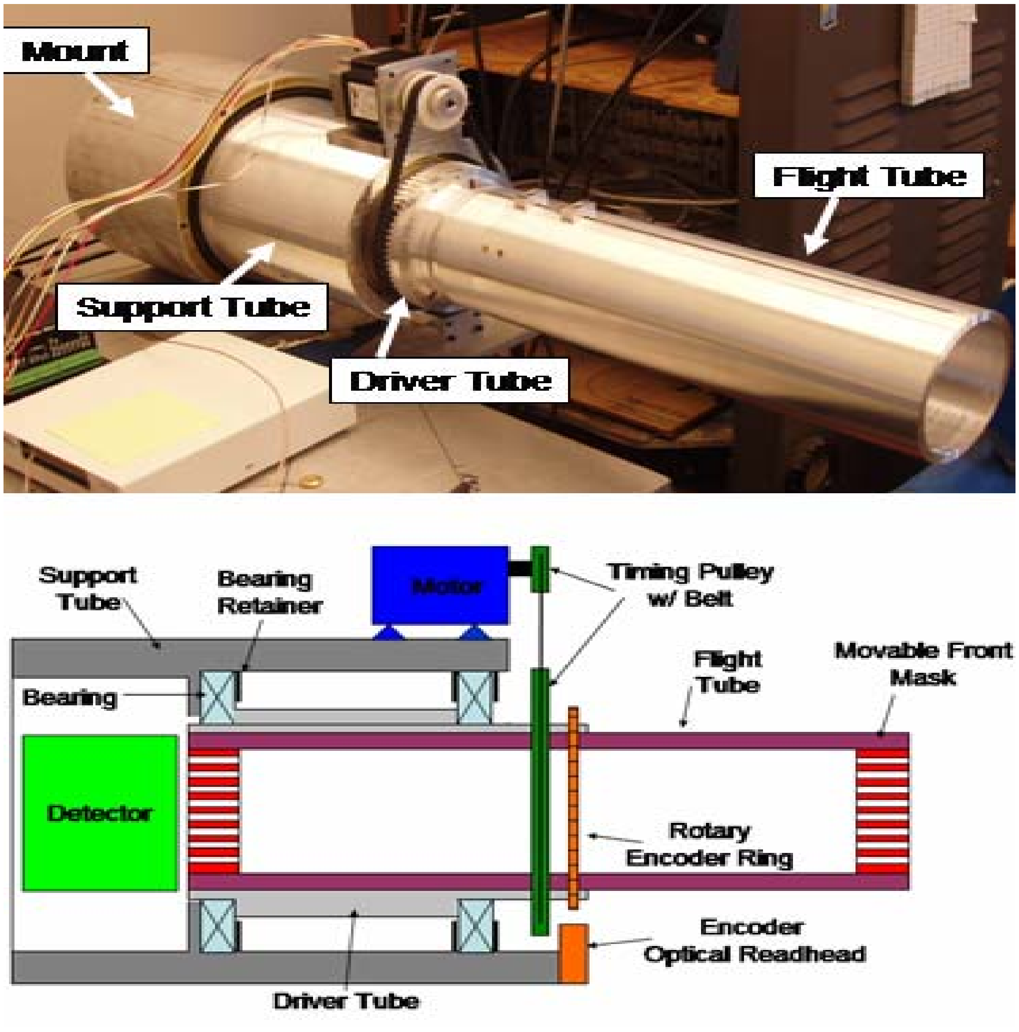

Figure 3-1. Illustration of the RMC system design.

3.1.2 RMC Mask Design

The design of the RMC masks has a direct influence on the system field of view, angular resolution, detection time, and dynamic range. As with all mechanical collimation systems, it is desirable to have masks that are as opaque to the incident photons as possible. A tradeoff occurs however, between the mask field of view, which is reduced with thick masks and the modulation efficiency (Eq. 2.33) and dynamic range (discussed in section 2.4.2), which are reduced by photons that penetrate the masks and are counted in the detector. Figure 3.2 shows a plot of the RMC modulation efficiency versus mask thickness when the unmodulated background is zero at several photon energies for lead and tungsten.

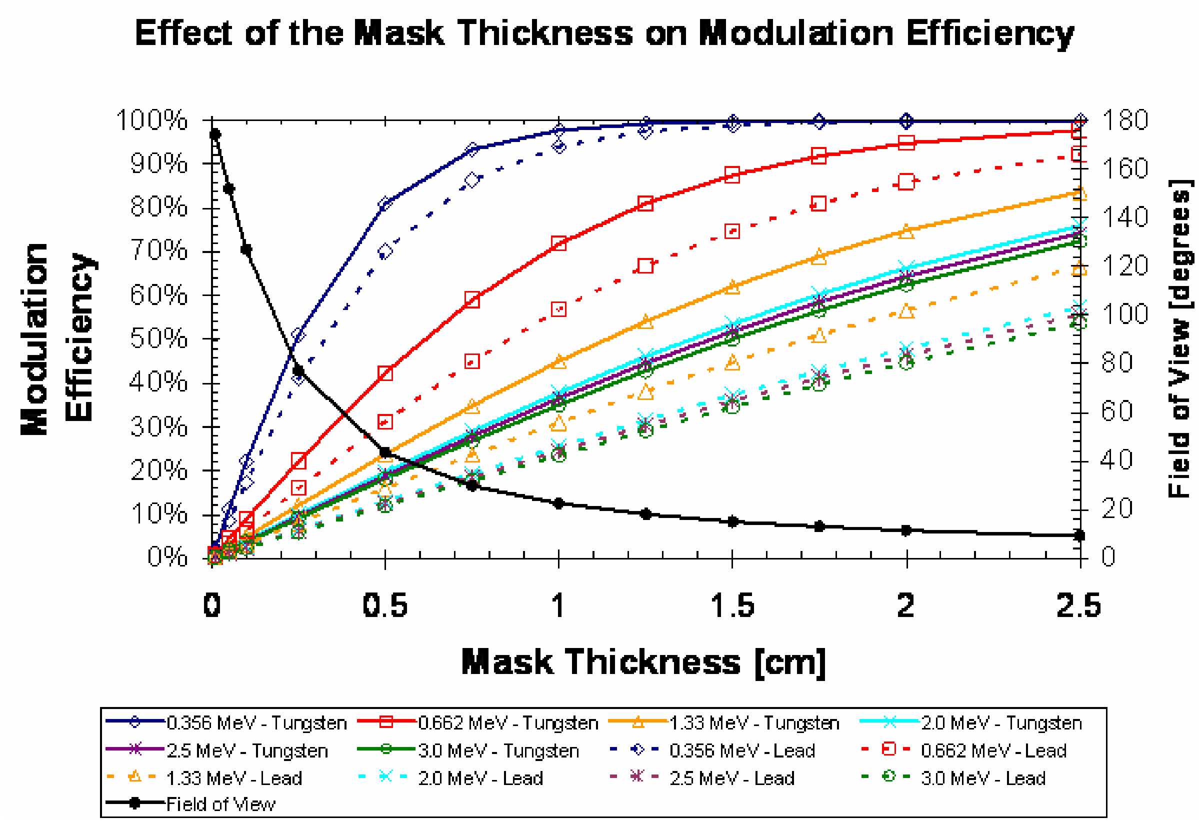

Figure 3-2. This figure illustrates how the modulation efficiency changes as a function of mask thickness for both tungsten and lead masks. The black line shows how the field of view changes with thickness when the slits are 4mm wide.

Figure 3.2 highlights one of the key disadvantages when considering an RMC system for the orphan search problem. When searching for unknown sources, it is desirable to have a large field of view so that a large area can be scanned with a single measurement.

The field of view is given by Eq. 2.21 when the masks are infinitely thin (an assumption often made in far field models), but is reduced once the masks have a finite thickness. For masks with finite thickness, the field of view is defined by

$$FOV_{mask} = 2\arctan\left(\frac{w}{2t}\right), \tag{3.1}$$

where w is the slit width and t is the thickness of the mask. Therefore, even though moving the masks closer together results in a larger two mask field of view, the overall field of view will still be limited by the thick mask effect given in Eq. 3.1. Referencing Fig. 3.2 it is seen that it would require a 2 mm thick mask to produce a mask field of view that is ~90°. At this mask thickness, the modulation efficiency has a maximum value of ~50% for Ba-133 and a minimum value of ~5% for the 1.33 MeV line of Co-60. Because the modulation efficiency is reduced, it will require more photons in order to resolve an image, because the peaks in the measured transmission function will be very close together.

The mask pattern is another important design parameter that fundamentally determines the detector response that is measured. Wilmore demonstrated that the RMC mask pattern did not need to be limited to slits and slats, and derived the predicted performance for 2D checkerboard masks as well as curved slits [Wil70]. Novel mask patterns are beyond the scope of the questions considered in this thesis however, and only traditional RMC masks with simple slits and slats are considered. The research did highlight potential for some different mask patterns and these will be discussed in Chapter V of this thesis under future work.

There is one mask design feature that will be discussed here, that is useful when considering a single RMC system for the orphan source search problem. Recall that when symmetric masks are used to image a single point source there is a 180° ambiguity caused by the symmetric nature of the masks. Previous work has demonstrated that the ambiguity can be removed by making multiple measurements with the RMC at different locations or orientations [Sch67]. The 180° ambiguity can also be removed by changing the design parameters of the masks so that the system is no longer symmetric. Figure 3.3 shows simulated RMC transmission functions and reconstructed images when the masks are symmetric (left panels) and asymmetric (right panels) for a point source located 1000 cm from the RMC. In the symmetric case the masks are the same those described in the RMC system design. In asymmetric case the grid pattern in the front mask is shifted 2mm off axis, so that the mask pattern is not symmetric about the RMC centerline, causing the two masks to be out of phase with each other. Using the simulated curves shown in Fig. 3-3, the cost for making the masks asymmetric in this case is a reduction in modulation efficiency (Eq. 2.33) by <1% and a reduction in the geometry efficiency (fraction of photons incident on the top of the RMC that hit the detector) by <3.6%.

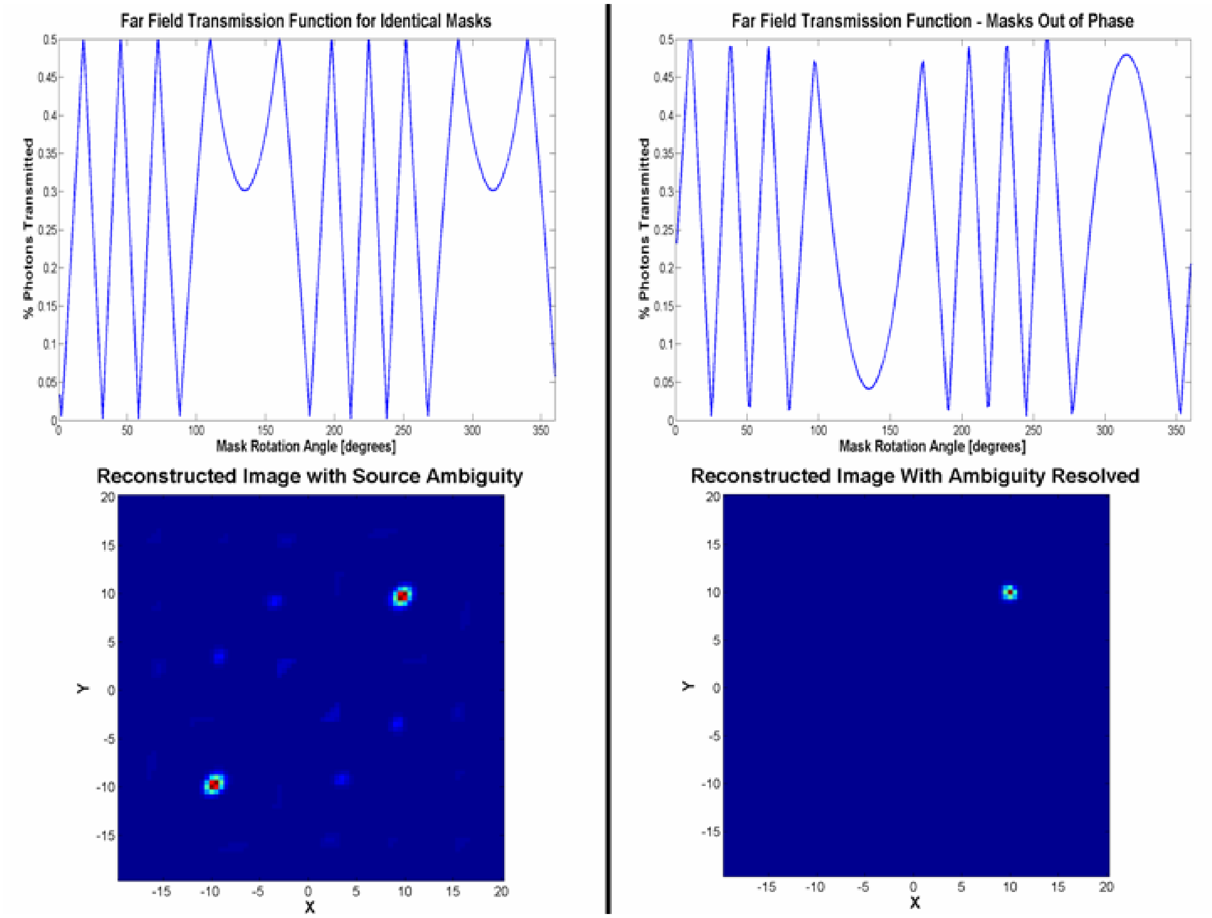
Far Field Transmission Function for Identical Masks

Far Field Transmission Function - Masks Out of Phase

Reconstructed Image with Source Ambiguity

Reconstructed Image With Ambiguity Resolved

Figure 3-3. When the RMC masks are symmetric (left panels) the 180° ambiguity is apparent. When the masks are made asymmetric (right panels) the ambiguity can be resolved with a single measurement. The cost of making the masks asymmetric is a reduction in the RMC modulation and geometric efficiency.

The sets of RMC masks built for this study were not optimized, but instead selected to ensure a relatively wide field of view with an angular resolution of ~1°. The first set of masks was cut out of a 12.7 mm thick piece of lead using wire electrical discharge machining (EDM). The slits and slats are equal width of 4 mm and a pitch of 8 mm. The diameter of the masks is 38.1 mm for a total of 8 slits and 8 slats per mask. Using Eqs. 2.21 and 2.22 and a mask separation parameter of 50 cm (limited by the length of the flight tube), the maximum resolution for these masks is ~0.5° with a ~9° field of view. The maximum field of view of ~18° occurs when the mask separation is ~24 cm at which point the angular resolution is ~1°.

3.1.3 Automation, Control, and Feedback Systems

Another important RMC design consideration is the system used to power and control the tube rotation and provide feedback on the instantaneous angular orientation of the masks. The most practical and inexpensive solution for driving the tube was a HT23-397 Applied Motion stepper motor that is powered and controlled by an Applied Motion Si3540 driver. The driver is capable of micro-stepping the motor in increments less than 0.01° per step. The pertinent design parameters for the motor and driver are listed in Appendix B [App08].

The stepper motor is mounted on top of the support tube as shown in Fig 3.1 and transmits power to the driver tube via a timing belt, with a conversion factor from the motor pulley to the driver tube of 3.27 to 1. That is, the stepper motor must rotate 3.27° to rotate the driver tube 1°. Because the stepper motor can move in very precise increments, it is possible to crudely estimate the angular orientation of the masks based on the distance the motor has rotated. This feature is limited however by backlash in the timing belt as well as the fractional conversion factor between the stepper motor and driver tube pulleys. A more elegant solution is the addition a high resolution rotary position encoder device to the driver tube. The selected encoder is a large bore Renishaw optical encoder ring that mounts onto the driver tube. The perimeter of the encoder ring is marked with lines every 20 μm which are read using an optical read head that is attached to the support tube. The optical read head outputs two square wave signals in quadrature (90° phase shift between signals) that indicate the position of the read head with respect to the marks on the optical ring. These two signals are decoded using a custom built decoding circuit to produce position information in useful angular units such as degrees. The decoding circuit contains of an Avago HCTL-2016 quadrature decoder/counter integrated circuit [Ava06]. For each line on the encoder ring, the counter will be incremented four times representing the low-high and high-low transitions of two quadrature signals. When the ring has completed one rotation, a magnetic reset on the encoder ring sets the counter back to zero. If the RMC rotates backwards the counter is decremented using the same procedure. The angular position of the RMC in degrees is computed by dividing the IC counter output by four and then multiplying by 360 divided by 18000 (# of marks on the encoder ring). A picture of the decoding circuit can be seen in Appendix B.2.

When properly calibrated, the encoder system provides the angular orientation of the masks with 1.2 arc minutes of resolution [Ren08]. The rate at which the angular position can be updated is limited by the decoding circuit, which is controlled using a Labview 8.2 interface. Labview is a graphical programming language used to automate and control laboratory systems [Nat08]. In order to read the IC counter, a trigger must be sent to the decoding circuit. This trigger causes the IC to lock the instantaneous position of the counter into a buffer. The buffer is read out in two parts: a high byte and a low byte. A reset trigger is then sent to the decoding circuit that clears the buffer and allows it to accept another value from the counter. The total time to perform this operation is measured using a profiling tool in Labview. This profiler runs the decoder read routine 100 times and each iteration records the time it takes to complete the routine. The mean of these results indicate it takes ~50 ± 5 ms to complete a single read operation. This places a limit on the rate at which the RMC can be rotated given a desired sampling resolution. As an example, assume that a given measurement requires a sampling resolution of one sample per degree (360 total samples per revolution). The decoding circuit has a maximum recording rate of ~20 samples per second, which means that the RMC must rotate slower than 20 degrees per second to maintain the desired sampling resolution.

3.1.4 Data Acquisition

Another attractive feature of RMCs is that the data acquisition and processing systems can be made relatively simple depending on the objective. For a non-spectroscopic system, the only data requirements are the mask orientation as a function of time (provided by the decoder system in section 3.1.3), and the number of counts recorded as a function of the mask orientation. In some of the earliest astronomical RMC observations, simple Geiger counters and even films functioned as the detector [Bra68]. The primary reasons to move to a spectroscopic system for the orphan source search problem are: (1) improved signal to noise due to discrimination of low energy, high count rate background, and (2) isotope identification. Therefore a third piece of information used in this problem is the measured energy spectrum as a function of mask orientation.

The data acquisition and pulse processing schematic for this research is shown in Figure 3.4 and a list of the equipment and typical settings used is given in Appendix B.3. First the detector signal passes through a pre-amplifier and into a shaping amplifier. This signal is then fed into one or more single channel analyzers (SCA) that are operated in an energy window mode. Any pulse that enters the SCA and is within the set energy window will trigger the generation of a 5 volt logic pulse. This logic pulse is then sent to a National Instruments data acquisition board that counts the logic pulses as they are generated.

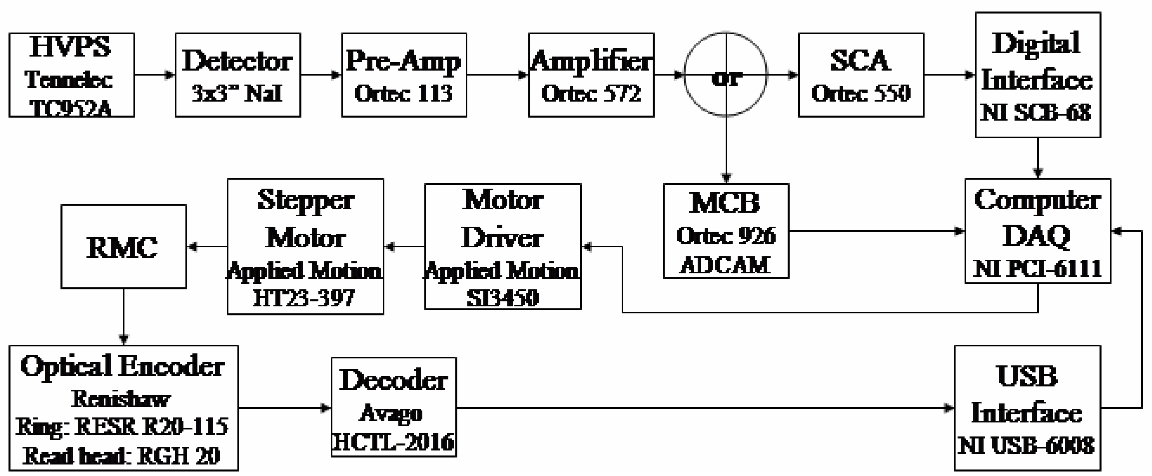

Figure 3-4. Block diagram of the RMC data acquisition system.

As mentioned above, for the orphan source search, it is desirable to use a multi-channel analyzer rather than a single channel analyzer since it allows a search over the entire energy spectrum simultaneously. This will be highlighted further in section 4.3, where the effects of multiple sources at different energies are discussed. The SCA method was initially chosen for simplicity, and is adequate for characterizing the RMC system given that the source position and activities are always known quantities and are controlled in the lab setting. Prior to recording a RMC transmission function, all sources used in the experiment are placed as they would be during a measurement. The output of the shaping amplifier is fed into a multi-channel analyzer that records a pulse height spectrum. The spectrum is analyzed to locate the photopeak associated with the source and the channel numbers bounding the peak are recorded. These numbers are converted into volts by dividing the channel number minus the MCA offset by the MCA resolution, which was set to 4096 bins for these measurements. The resulting values are then used to set energy windows on the SCA.

During a measurement, the data acquisition board records the number of counts from the SCA, while the decoder system records the angular orientation of the masks. When the system is rotated continuously, the data recording process occurs in a sequence. First the system queries the decoding circuit to get the instantaneous angular orientation of the masks. Next the counter is queried and the current number of counts is recorded. This process repeats, and each operation can occur only after the previous datum has been recorded. The measured RMC transmission function is now constructed by merging the position and counter data, to define the number of counts recorded as a function of mask orientation.

3.1.5 System Calibration

The system calibration consists of all the RMC features that must be aligned and set correctly in order to produce a position estimate that correctly matches the true source location. For this research this not only includes calibrating the system itself, but also developing a method of accurately positioning the reference source with respect to the RMC.

3.1.5.1 Mask Alignment

Proper alignment of the RMC masks is important not only to ensure that the system response matches the system model, but also to maximize the geometric and modulation efficiencies. Grid alignment for all measurements is accomplished using two methods. In the first method, the rear mask is inserted into the flight tube and locked into place. The front mask is then set in the mask carrier so that the masks will be roughly aligned when the carrier is placed in the flight tube. Once the carrier and front mask are placed in the flight tube, the carrier is locked in place near the front of the tube. A calibrated flat aluminum bar is then inserted into the middle slot of the front mask and fed through the tube so that it rests on the corresponding slot on the rear mask. If the masks are out of alignment, the bar will not rest flat on both slots. In this situation, the front mask is rotated in the carrier slightly and the bar test is repeated until the bar rests flat on both the front and rear slot. Given the uniformity of the flat bar, and the uniformity of the two masks, this method is sufficient for aligning the masks to within 0.5°. This is validated by fixing the flight tube to a rigid flat surface and then using a digital level with 0.1° of accuracy to measure the angular displacement of the rear mask. The measurement is repeated on the front mask, with the difference representing the total angular offset.

3.1.5.2 Setting the RMC Initial Position

Once the masks are aligned, the flight tube is inserted into the driver tube and locked in place. Before a measurement can be made however, the position of the starting orientation of the masks must be set to a known reference position. First the front mask is extended so it is almost to the end of the flight tube. The flat calibration bar used to align the masks is inserted into a slot on the front mask and fed through the flight tube and into the corresponding slot on the rear mask. The digital level used to align the masks is placed on the bar sticking out of the front mask and the flight tube is rotated until the bar is level. The decoder system is then queried for the current angular position of the tube, which represents the angular offset that must be supplied to the post-processing algorithm to ensure a proper position estimate.

3.1.5.3 Source Positioning System

Knowledge of the absolute source position with respect to the centerline of the RMC is important for measuring any bias that might exist between the true source location and reconstructed position estimate. The Velmex Bi-Slide 2-axis linear stage is used to provide this high level of position accuracy. Figure 3.5 shows the positioning system and the source holder used to accurately move the source.

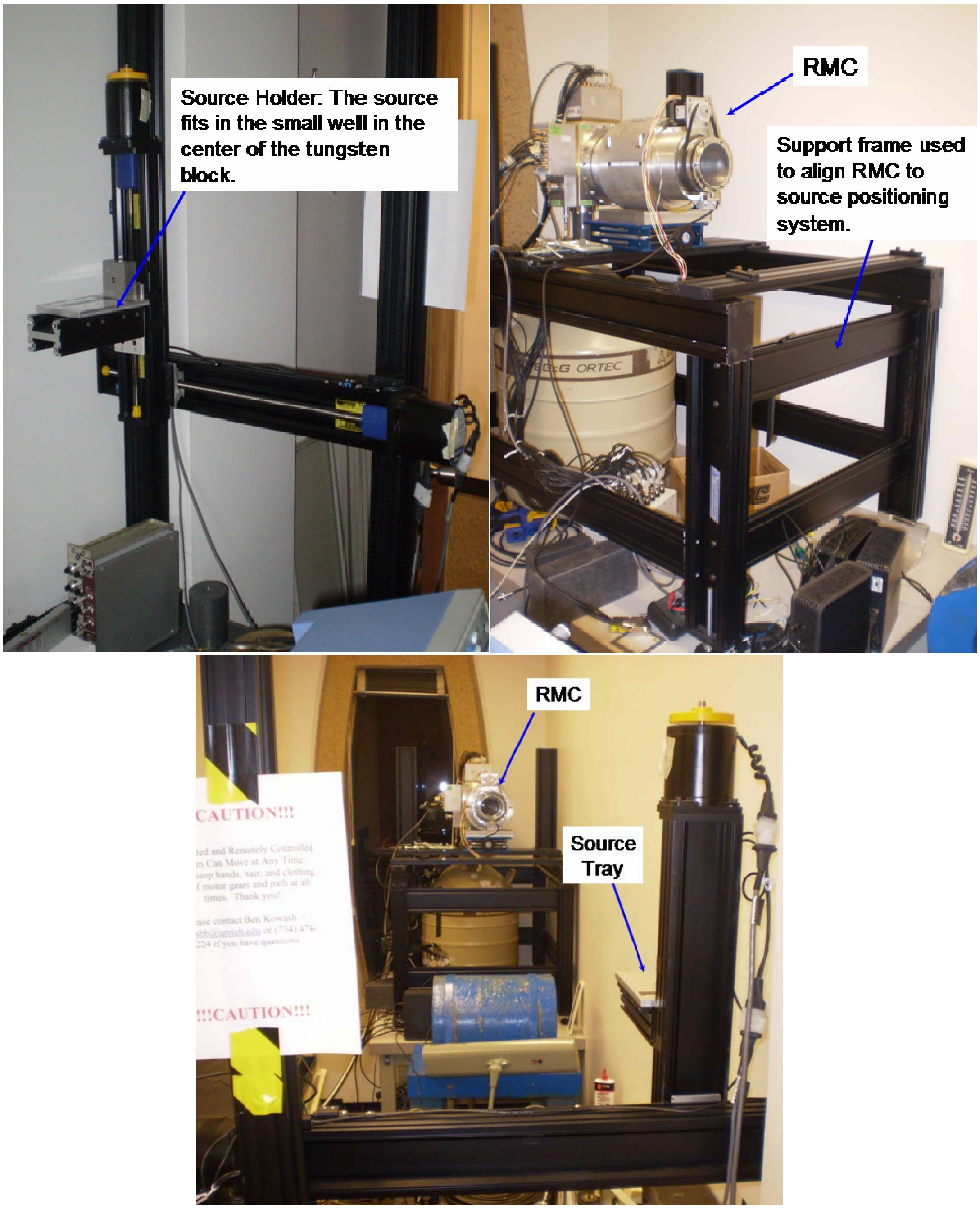

Figure 3.5. A picture of the Velmex source positioning system used to accurately position the source with respect to the RMC is shown in the top right panel. The RMC (top left) is mounted on a frame that can be aligned to the Velmex system. Once the frames are calibrated and aligned, the source can be positioned with 5 μm of precision. The bottom panel shows the RMC as seen from behind the source positioning system.

The Velmex system is a frame that supports two crossbars (one vertical and one horizontal) with threaded screws. The screws are used to move a small table containing the source in the x- and y- dimensions and are driven by two stepper motors that can be controlled using Labview. This system allows the source to be positioned to ~5 μm of precision in either dimension. The current system is limited to 50 cm of translation in the x-direction and 25 cm in the y-direction, making this tool primarily useful for near field measurements.

Once the Bi-Slide is set up at some distance from the RMC, it must be properly leveled and aligned to ensure that the source plane remains perpendicular to the RMC axis of rotation for all potential source positions. This alignment is accomplished by mounting and aligning the RMC to its own fixed frame seen in the upper right panel of Fig. 3-5. A flat bar is attached horizontally to the front of the RMC frame. Next a laser is mounted on the source tray and the tray is moved so that the laser is centered on the horizontal bar. A laser range finder with an accuracy of 0.5 mm at 45 meters is used to measure the distance from the source tray to the bar. The source tray is then translated in the x-direction a known fixed distance and the distance between the source tray and the bar is again measured. This process is repeated along the length of the bar, and horizontal adjustments are made to the source positioning frame if the range begins to drift. Once completed, the procedure is repeated for the y-axis of the system. After the two systems are aligned, the range finder is used to measure the distance from the source to the detector, which is used in subsequent imaging experiments.

3.1.6 Validation of the Universal Field Model

In section 2.2.3.3 the new universal field system model was compared to an existing far field model, and result indicated that the models match when the source is in the far field. In this section, the universal field model is compared against measured data taken with the RMC system presented above. These results demonstrate that the universal model accurately matches the measured transmission function.

For this experiment the 1.27 cm thick mask pair is used with a mask separation of 24 cm. A 1.7 mCi Ba-133 source is placed at $(\rho,\phi) = (2.86,-90)°$ and measurements are taken with the source at 1, 2, 5, and 10 meters from the RMC. For Ba-133 the measured photopeak efficiency at 356 keV is ~22% and the unmodulated background is ~7 counts per second. The total measurement time was 360 seconds, with a sampling frequency of 1 sample per degree. The transmission function generated by the universal field model is plotted against measured data illustrating its ability to predict the system response as seen in Figure 3-6. For this particular set of images the masks were assumed to be completely opaque. This is why there is a slight discrepancy between the measured data and the model at the bottoms of the valleys as well as in the low frequency dip.

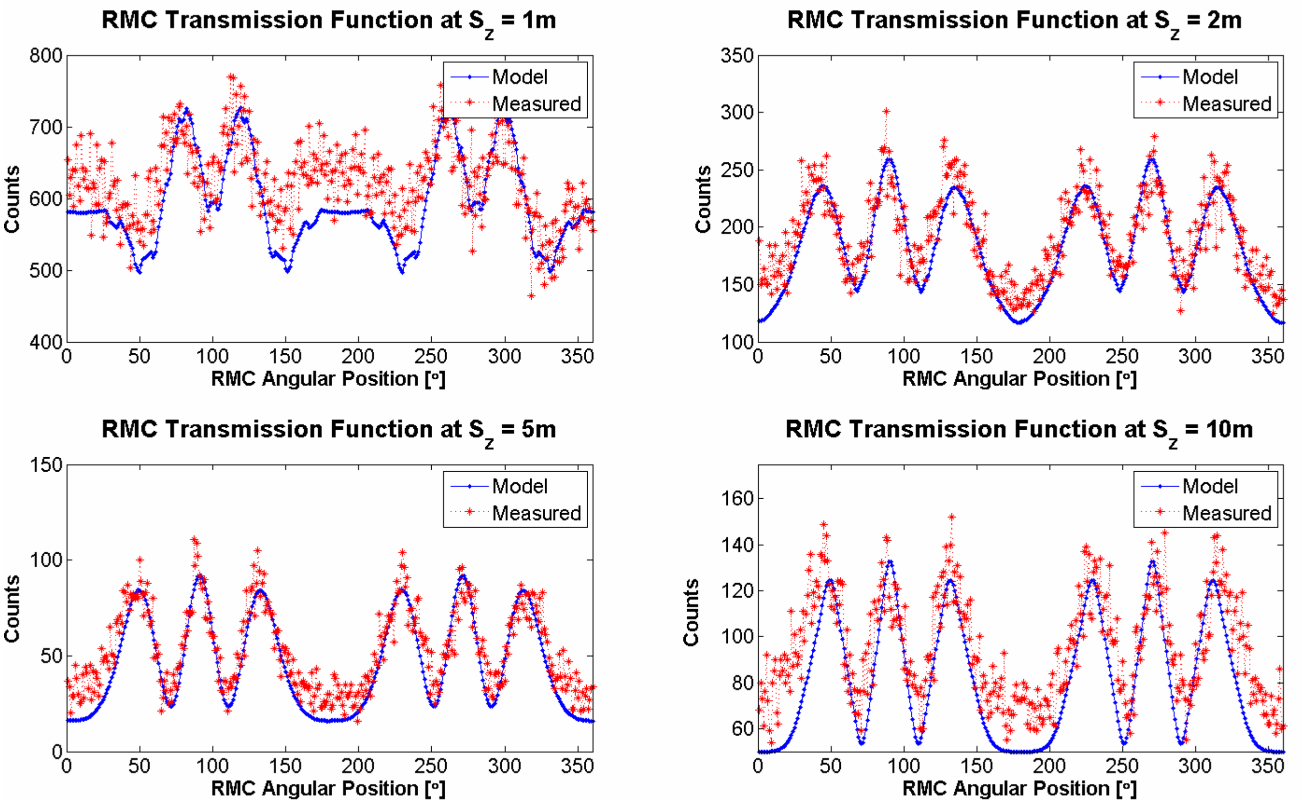

Figure 3-6. The universal field system model described in chapter 2 is plotted against data measured using the RMC system outlined in chapter 3. The model is accurate even when the source is 1 meter from the RMC. The discrepancy between the model and data at the large dip is caused by the model's assumption of black masks.

The next test compares the universal and far field models when they are used with the MLEM algorithm and the measured data to reconstruct images. The two indicators used to assess the model sufficiency are the reconstruction accuracy and the standard deviation of the position estimate calculated using the bootstrap method. Table 3.1 lists these parameters for the four source scenes shown in Fig 3.1. The data highlights that the universal field model accurately locates the source at each of the four positions. The far field model is capable of locating sources accurately at three of the four positions, although with less precision than the universal model. When the source is located at 100 cm the far field model breaks down and fails to locate the source correctly. Some of the error at 100 and 200 cm may come from systematic source positioning errors. For these measurements it was not possible to use the Velmex positioning system, so the sources had to be placed by hand. At a very close range such as 100 cm, a shift of only 1 cm can change the radial source position by as much as 0.6°. Compare this to 1000 cm, where as 1 cm shift results in a radial position shift of only 0.06°.

Table 3.1. The data listed below are the estimates of the polar coordinates for a source located at $\rho,\phi = (2.87,-90)°$. The universal field model produces superior estimates based on the position accuracy and standard deviation. The far field model becomes more accurate as the source moves further from the detector toward a far field condition.

	Universal Field Model			**Far Field Model**		
Sz [cm]	**Position Estimate (ρ,ϕ) [deg]**	**Error (ρ,ϕ) [deg]**	**1σ St.Dev (ρ,ϕ) [deg]**	**Position Estimate (ρ,ϕ) [deg]**	**Error (ρ,ϕ) [deg]**	**1σ St.Dev (ρ,ϕ) [deg]**
100	2.48, -83.8	0.39, -6.2	0.02, 0.6	1.37, -73.7	1.49, -16.4	0.18, -15.3
200	2.94, -88.9	-0.07, -1.1	0.03, 0.6	2.81, -86.9	0.06, -3.1	0.06, 1.6
500	2.80, -89.2	0.06, -0.8	0.02, 0.3	2.66, -86.6	0.20, -3.4	0.03, 0.45
1000	2.82, -86.8	0.04, -3.2	0.03, 0.4	2.72, -86.8	0.14, -3.2	0.22, <0.1

3.2 RMC Operational Parameters

There are a variety of operating parameters that can be modified with regards to RMC imaging that may be beneficial for locating orphan sources. In this research three adjustable parameters considered are: the separation between masks, the angular velocity of the rotating masks, and the position and pointing vector of the RMC centerline. The mask separation affects both the system resolution and field of view as given by Eqs. 2.21 and 2.22. Changing the resolution is advantageous, and simulation results will demonstrate that an RMC can image distributed sources by making several measurements with different mask separations and then combining the data for a single image reconstruction. The same procedure is also shown to improve the quality of the image when multiple point sources are in the field of view.

3.2.1 Mask Separation Parameter

Changing the mask separation distance during a RMC measurement is a powerful tool for improving the imaging performance of the RMC, because it allows the system to make measurements of the source scene at different resolutions. This in turn allows for imaging of complex source scenes containing extended sources with more complex geometries. Mertz et al. first proposed building an array of RMCs as a way to sample multiple Fourier components of a given source scene [Mer86]. This was first put into practice by Fisher et al. with the WINKLER spectrometer, which consisted of an array of 9 RMCs coupled to high purity germanium detectors [Fis90]. Each mask pair had a different number of slits and slats, allowing the detectors to record different frequency components of a particular source distribution. The mask design was straightforward with each mask pair containing 1 more slat than the mask pair before it. For example the first mask pair consisted of a single large slat. The second mask pair had two slats that were evenly distributed, while the third mask pair had three slats. This pattern continued so that the ninth mask pair had nine thin slats and nine thin slits. The single slat collimator will record very low frequency transmission functions and the nine slat collimator will have a very high frequency response, but each response is still unique to a particular source position. Combining the data from all nine collimators produces a reconstructed image with significantly less noise and the removal of image artifacts (particularly ring side lobes that are produced using Fourier reconstruction methods) [Mer86]. This same concept was applied to the RHESSI satellite, which built upon the early success of the WINKLER spectrometer and shares many of the basic design concepts. RHESSI uses the measurements of the different frequency components as a way to create images of elongated distributed sources [Huf02].

This same principle can be achieved with a single RMC by changing the mask separation parameter during a measurement. When the masks are close together the transmission function for a given source position will have a lower frequency than when the masks are far apart. This effect is seen in Figure 3-7, which shows how the separation distance between masks affects the transmission function for a point source at x,y,z = (0,-10,241).

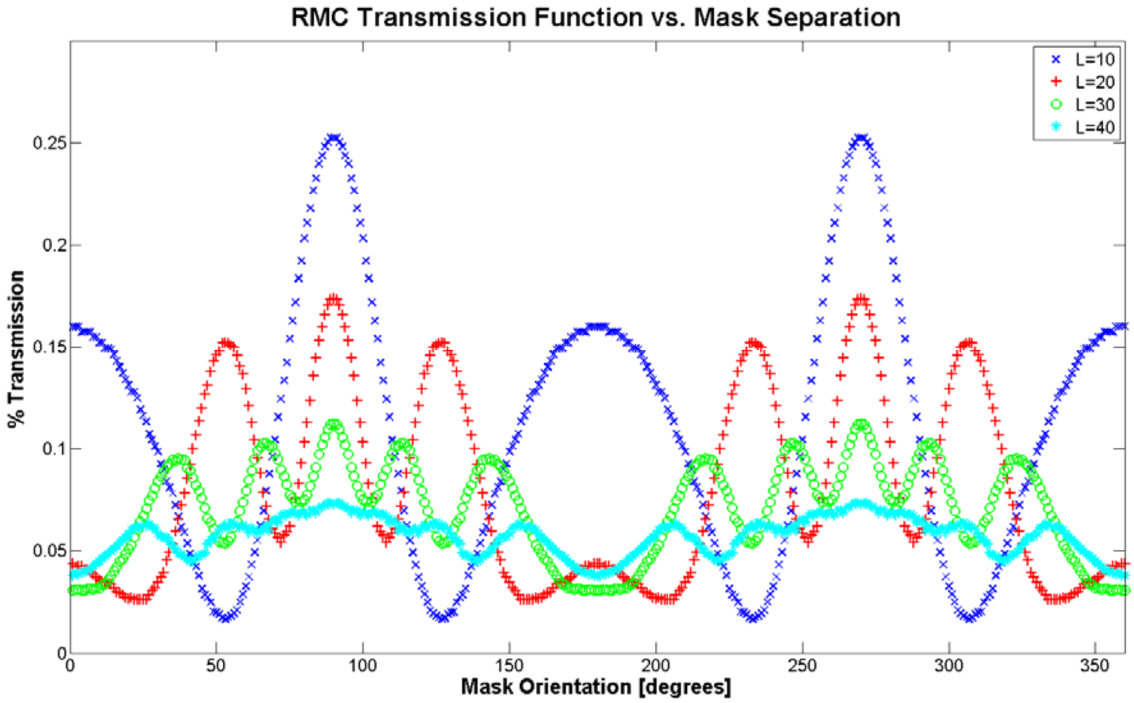

Figure 3-7. The separation between the masks impacts the frequency of the transmission function as shown here for a point source at x,y,z = (0,-10,241) cm. When the masks are close together the transmission function has a lower frequency than when they are further apart.

Another way to study the effects of the mask separations is to plot the CRLB for the polar coordinates for several different mask separations as shown in Figure 3-8. The plot shows the CRLB as a function of the radial coordinate ρ, which has been converted into the Cartesian coordinate x at 241 cm.

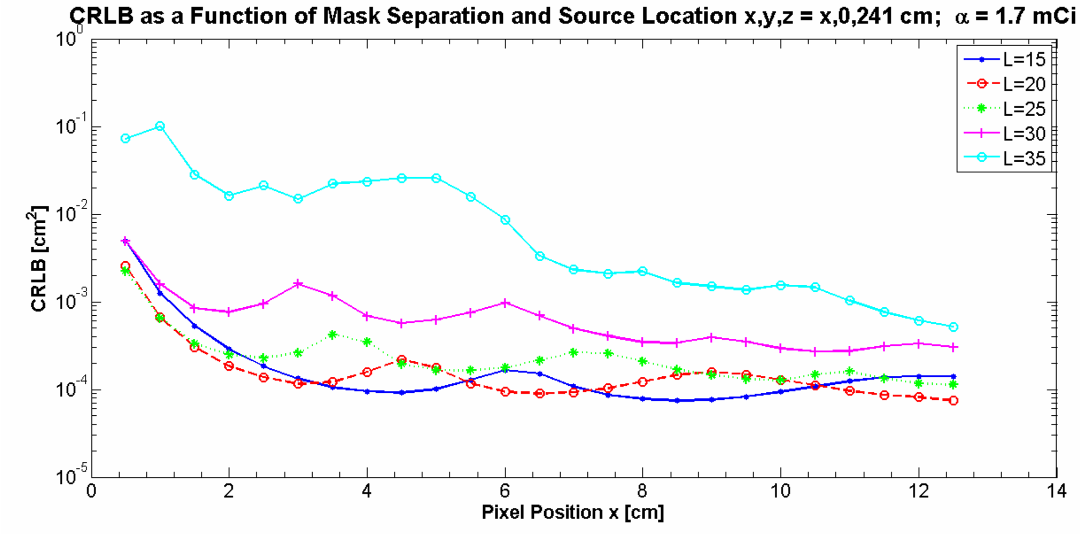

Figure 3-8. The CRLB on the source position is affected by the choice of mask separation. It is seen that no single mask separation parameter has the best variance properties at all positions. This reflects the fact that each mask separation parameter is most sensitive to a particular set of spatial frequencies in the source scene. The magenta and cyan curves representing L=30 and 35 cm mask separations have poor variance properties because of excessive magnification values when the source is in the near field.

The different curves in Fig. 3-8 demonstrate that there is no single mask separation that can provide the best performance at all positions in the field of view. This effect is seen experimentally in Chapter 4, when the RMC field of view is mapped. For a given mask separation some source locations will produce better images than others. The benefit of making multiple measurements with multiple mask separation parameters is that more spatial frequencies of the image can be scanned which reduces the noise in images caused by pixels that have similar frequency characteristics as the one containing the source. In the near field care must be taken when choosing which mask separation values to use. The cyan and magenta lines are created when the mask separation is 30 and 35 cm respectively. When the source is only 241 cm from the detector, these larger separation values produce a higher degree of magnification, which in turn reduces the image quality. This is reflected by the CRLB, which shows that the achievable lower bound on the variance is much higher than for the smaller mask separation parameters.

This technique is now applied to a couple of scenarios to demonstrate how changing the mask separation parameter is useful for enhancing the imaging performance of the RMC. The first scenario simulates a 16 cm long rigid ruler source. The rigid ruler contains 8 source pellets that are 100 μCi each and are 1 cm long. Each source pellet is separated by 1 cm of lead, so that there is a 1 cm space between sources. The ruler is simulated at y,z = (5,241) cm and is symmetric across the y-axis. This puts a source at x = -7, -5, -3, -1, 1, 3, 5, and 7 cm. A series of RMC simulations are then run using different combinations of the mask separation values used in Fig. 3-8 for the CRLB. In order to be consistent, each simulated measurement uses the same total scan time of 30 minutes. If a simulated measurement uses two different mask configurations, then half of the total time will be spent with the masks at position 1 and the other half of the measurement time at position 2. Figure 3-9 shows the reconstructed images as a function of the mask separation parameter.

The first image (A) is simulated with the mask separation equal to 15 cm. The strong point response in this image is characteristic of reconstructed RMC images where the sources are closer together than the angular resolution. Recall Fig. 2.14, which illustrated that when two point sources are close together, the combined transmission function can resemble the transmission function for a single point source. The superposition of sources in Fig. 3-9 has this effect and therefore the peak appears in the image. Once two measurements are made with different mask separation parameters (B), the lateral dimension of the source appears clearly in the image, although the individual sources are not resolved. As more mask measurements are made with different mask separations (C & D), the individual sources begin to be resolved. For this image there is a limit to the resolution however, because of the range where the source is imaged. As Fig. 3-7 shows, the CRLB is much poorer when the masks are separated by 35 cm due to magnification in the near field. The theoretical angular resolution given by Eq. 2.22 when the mask separation and slit pitch are 35 cm and 8 mm respectively is ~0.655°. This translates to a spatial resolution of ~2.75 cm when the source is located 241 cm from the detector. Because each source is located 1 cm apart, it is reasonable that only every other source is apparent in image D of Fig. 3.8. Image D is noisy because of the presence of the remaining unresolved sources.

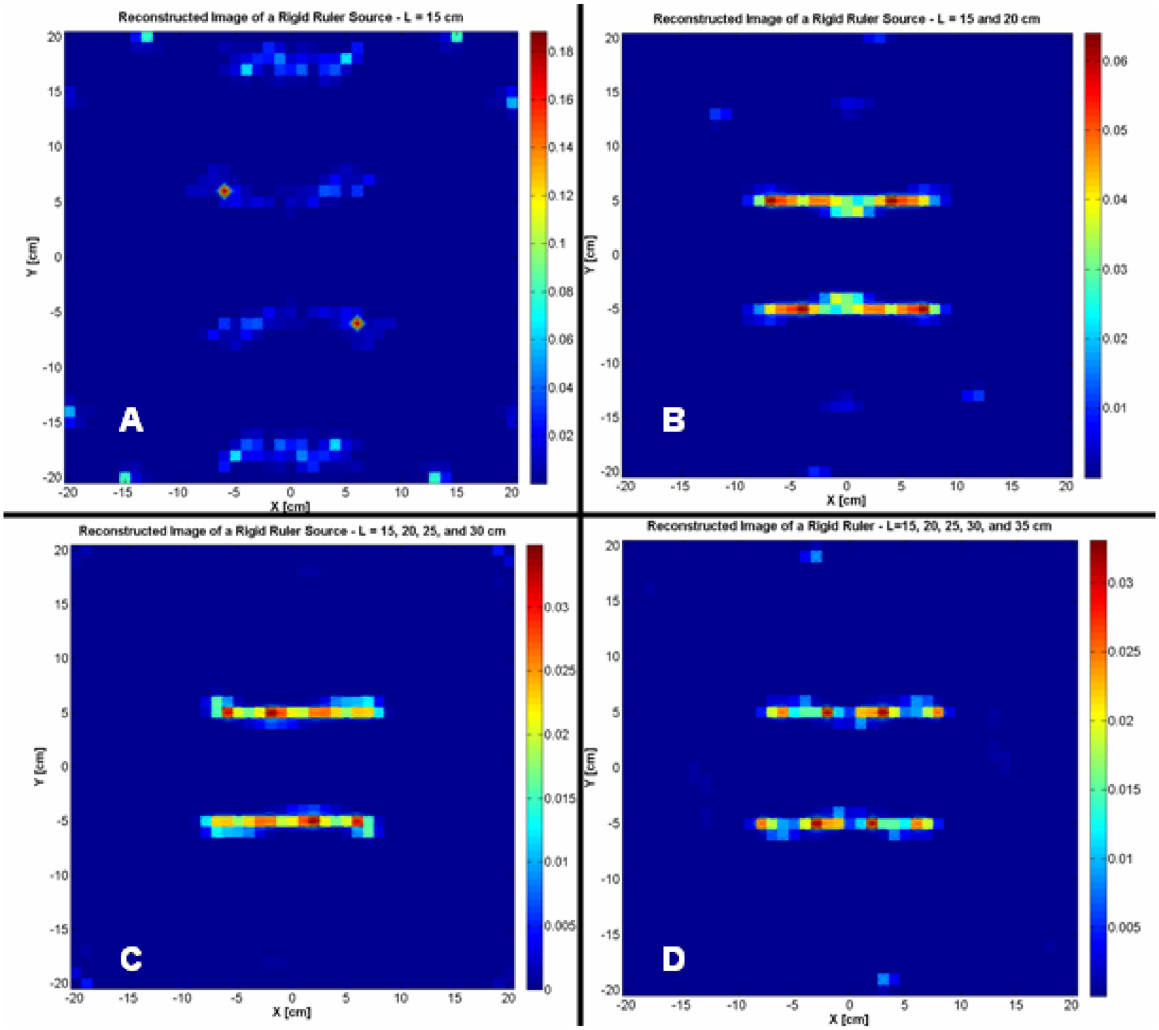

Figure 3-9. The images above illustrate the benefits of measuring a source scene with different values of the mask separation parameter. The simulated rigid ruler source contains 8 independent sources that are 1 cm long. There is also a 1 cm separation between each source. The image becomes better resolved as more mask separation values are added.

These results raise the question as to whether there is an optimal selection of mask separation parameters that should be used for a given source scene. This question is beyond the scope of this thesis, but a few statements can be made that might help guide future research. First, consideration must be given to the amount of information that a particular mask separation parameter provides to imaging a given scene. For the problem shown above, it is apparent from the CRLB shown in Fig. 3-8, that the larger values of L will produce estimates that have poorer statistical properties than smaller values of L, again due to the magnification. This can't be the sole deciding factor, because Fig. 3-9.D shows that adding the 35 cm mask spacing improves the ability of the system to resolve the individual sources. Also, each source scene will most likely be unique, so it isn't clear that a single universal sampling pattern can be developed. It therefore appears that an adaptive scheme as described in section 3.2.3 may be the best method for properly identifying the optimal mask separations to use for a given source scene.

The ability to successfully image extended sources is helpful in the orphan source search problem as it allows for the discrimination of nuisance sources in the field of view that contribute to the lumpy background. Because these nuisance sources are often unknown parameters prior to a measurement it is important to be able to determine whether peaks in a reconstructed image are from a true target source or from a larger distributed object. Consider Fig. 3-9.A again, where the mask position was fixed at 15 cm for the entire measurement and the resulting image was peaked. Without the additional information provided by other measurements, it could be possible to identify this peak as a target source. By using several measurements, the spatial structure of the source is measured and can be rejected as a background nuisance source. This is a problem often encountered with bare detectors. Many false positives often seen in bare detection systems come from these large distributed nuisance sources, and imaging allows discrimination of these large sources from the true sources of interest [Zio02].

Once a nuisance source is identified, it is possible to remove its effect directly using the MLEM algorithm. This is tested by simulating an extended T source seen in the first panel of Figure 3-10. This simulation used a sampling time of 30 minutes and 6 different mask separation parameters of 15, 20, 25, 30, 35, and 40 cm. The top bar of the T extends from -5 cm to 5 cm and the vertical bar runs from 5 to 15 cm, with a total activity of 1 mCi distributed through the entire source.

The second panel of Fig. 3-10 shows the same extended T source, except now a weaker 100 μCi source is placed at x,y = (10,-5) cm. This weak sources is not visible in the second panel because the stronger T source dominates the image. Once the T source has been identified, it can be removed from the image, by making a change to the way the background term, b is defined in Eqs. 2.30 and 2.31. Rather than assuming a uniform distribution, this background term is now defined by the measured transmission function of the extended T source plus the uniform background (that is, the measured transmission function used to generate the image in the far left panel). When the MLEM algorithm is executed again with this new assumed background, the T is removed from the image and the weak point source becomes visible (panel 3, Fig. 3-10). This process is summarized in the following 3 step procedure.

1. Measure a background scene that is free of any true orphan sources. This might occur in a site monitoring situation, where it is known that an area is orphan source free, but there is a potential for a source to be injected into the field of view at a later time.
2. The measured transmission function now represents the nuisance source background. The nuisance source transmission function is now assigned to the variable b, in Eqs. 2.30 or 2.31.
3. Re-run the MLEM algorithm using the new nuisance source background. The resulting image will not contain an image of the nuisance source as the algorithm now assumes that it is a part of the background. Any sources that were previously buried under the nuisance background may now be revealed.

The procedure does introduce some error into the image however, as the reconstructed source position is biased slightly low. This is a result of statistical noise caused by the extended T source. Although the extended T is removed from the image using this technique, the noise injected by the T source still remains and biases the reconstructed location of the hidden point source. The true source position is shown by the white Xs in the 3rd panel of Fig. 3.8, while the reconstructed position is ~4 cm to the right of this position. The magnitude of the bias will depend on the relative strength of the nuisance source with respect to the orphan source. If the nuisance source is very strong (compared to the orphan source), the bias will be greater than if the nuisance source is relatively weak. Future research should be conducted to quantify the relationship between the position bias and the strength of the nuisance source.

This technique can prove useful in scenarios where the RMC is placed at a fixed site and used to make multiple measurements over a long period of time. Examples of this could be outside a waste facility or at a remote border crossing. The RMC spends most of the time recording background data, and it is only when an event happens (accident, car enters field of view) that sources are injected into the field of view. During the background scans, the RMC may detect these extended nuisance sources from things such as railway lines, overpasses, or even waste lines in the case of the waste facility. Once the sources are injected, the background suppression technique can be applied to enhance the sensitivity of the system for locating weaker target sources.

It should be noted that this background suppression technique is not unique to an RMC system, but rather is directly related to the way in which the background is defined in the MLEM algorithm. As a result, provided the system matrix could be defined, this same approach can be applied to other imaging modalities such as coded aperture.

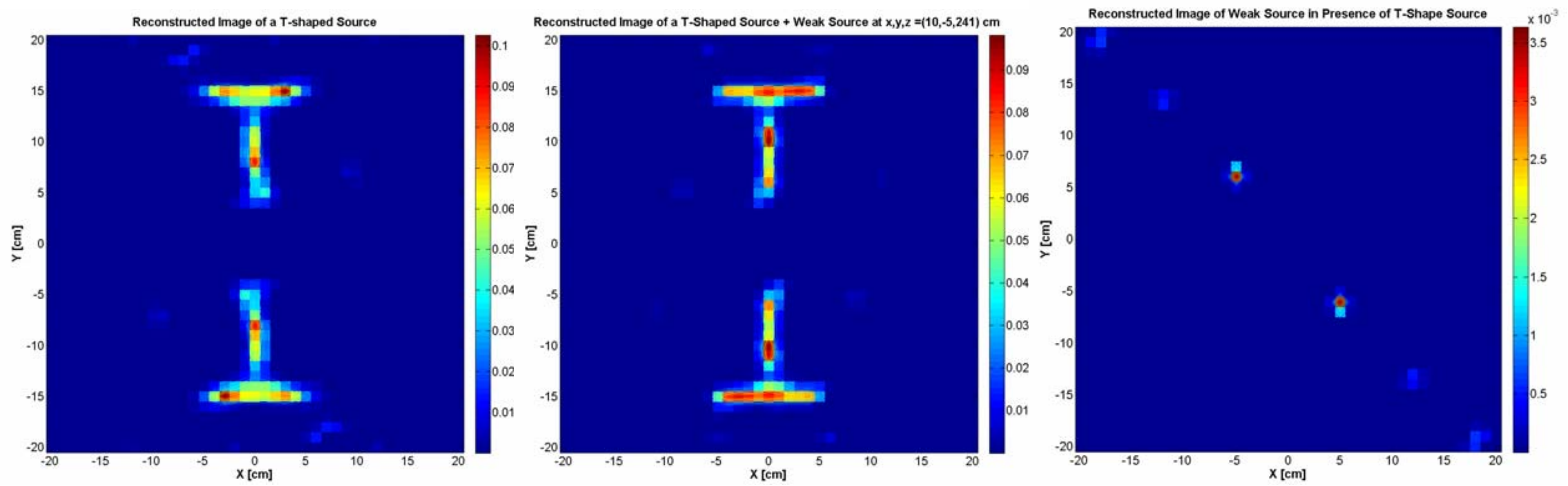

Figure 3-10. The three panels here demonstrate how a stronger nuisance source (T shaped source) can be removed during the MLEM algorithm to reveal a weaker target source. The first panel is the image when just the nuisance T-shaped source is present. The second panel contains both the nuisance source and weak point source. The third panel shows the weak source once the nuisance source is removed by adding its transmission function to the unmodulated background variable.

3.2.2. Adaptive Imaging Using the Dwell Time Parameter

Adaptive sampling techniques have been applied to a broad class of problems such as detecting the presence and position of a lost satellite in the sky or for locating small tumors in breast cancer patients [Pos63]. In a general sense adaptive sampling is a method where some operational characteristic of the system is modified during a measurement to enhance performance. These techniques often incorporate a fast uniform scan of the source scene allowing a prior estimate of the source location to be computed. This information is then used to develop a cost function, which is used to weight the importance of the search regions. These regions are then sampled according to the respective weight and a posterior estimate is computed. This new estimate is used to modify the cost function, which then is used to update the weights on each sample region. The regions are sampled again with the new profile and the process is repeated. As more information is recorded, the search scheme becomes more efficient at estimating the pattern necessary to locate the source. In the imaging community adaptive sampling has most recently been applied by Barrett et al. to pinhole imaging as well as SPECT imaging problems [Bar08,Fre08].

When considering the RMC system there are many parameters that can be adaptively changed to improve the imaging performance for the orphan source search problem. The optimal selection of mask separations is a good example of a parameter that lends itself to adaptive sampling. For the purposes of this research however, the focus will be on adaptively changing the dwell time τ_n from Eq 2.1, which is the amount of time the RMC spends sampling the n^{th} rotational bin. An adaptive scheme for the sampling time parameter is highlighted in Figure 3-11.

Results from this study show that adapting the sampling profile results in an increase in performance measured using a ROC curve, provided the true source position can be found reliably with sparse data. It is shown that this last constraint makes it difficult and possibly not practical to apply adaptive sampling for the unknown source problem.

For adaptive sampling with the RMC, one can imagine a system configuration where the masks rotate and data is recorded at a constant rate. After each rotation, an estimation algorithm such as MLEM is run with the current data set to generate an estimate of the source scene. This estimate is then analyzed for any statistically significant peaks, which are used to modify the dwell time vector τ for the subsequent scan. Regardless of how the vector τ is modified the length of each individual scan is held constant, or rather $\sum \tau_n \equiv$ constant for all scans. This process is repeated, until the total time allocated for the measurement has elapsed. The motivation for adaptively modifying the dwell time parameter is to locate sources faster, or for a fixed scan time, with more precision and less noise.

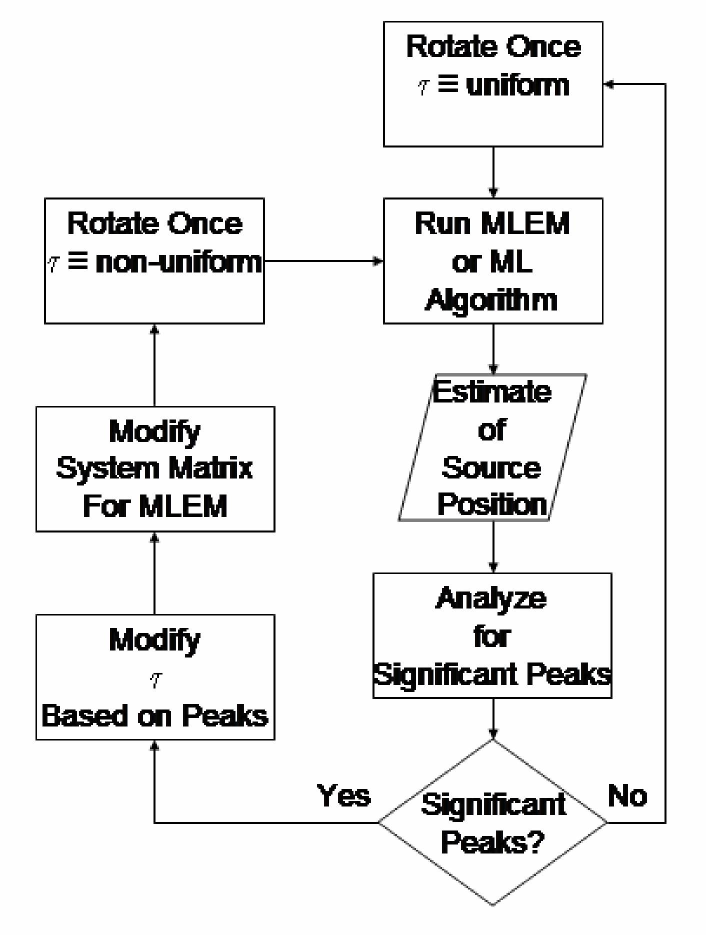

Figure 3-11. For each rotation the sum of the elements of τ remains constant. This process is repeated until the total time allocated for the measurement has elapsed.

The first step in the adaptive imaging chain is to take a measurement of the RMC for a single uniform velocity rotation. Once the first data set is recorded the MLEM algorithm is used to create an image, which is then scanned with a search algorithm to locate potential peaks. The method employed in this thesis for peak detection is the signal to noise ratio. The signal to noise ratio is given by

$$SNR_i = \frac{\lambda_i}{\frac{1}{N-1}\sum_{\substack{j=1 \\ j\neq i}}^{N-1}\lambda_j}, \tag{3.2}$$

where λ_i is the MLEM estimate for the ith pixel in the image. If only background is present, then the resulting image should be relatively uniform with no peaks and the SNR will be ~1 for all pixels. A peak is defined as any pixel that has a SNR greater than a user defined threshold. This threshold can be used to control the number of peaks allowed when adapting the sampling time. If a peak or peaks meets the detection criteria, then the sampling time for the next measurement is modified by increasing the dwell time at locations related to those peaks and decreasing the dwell time elsewhere. Once the dwell time is modified, another single rotation RMC measurement is recorded. The measured transmission function now consists of data from the first uniform scan plus the data from the second adaptive scan. This process is repeated until the total time allotted for the measurement has passed.

The measure of performance used in this research to compare the uniform and adaptive models is the ROC curves created by computing the log-likelihood distributions for source plus background and background only conditions. When the adaptive model outperforms the standard model, the distributions should separate and the area under the ROC curve should approach one.

Before proceeding it is useful to compare the ROC curves of a system where the source activity and location are known prior to the measurement. For this simulation, the source activity is 250 μCi and it is located at x,y,z = (0,50,1000) cm from the RMC. The tube rotation rate is 60 degrees per second, the total sampling time is 360 seconds, and the sampling resolution is 1 degree per sample. This results in 60 independent 6 second scans. The adaptive sampling time profile is very straightforward because it assumes the same profile as the transmission function for the target source. The 6 second scan time is divided up among the 360 angular bins and then scaled using the transmission function. Figure 3-12 shows the log-likelihood source plus background and background only distributions for both the uniform and adaptive sampling profiles. The ROC curves for each set of distributions are also shown.

The relative performance of both systems is evaluated by comparing the area under the ROC curves. The area under the uniform sampling ROC curve is 0.91, while the area under the adaptive sampling ROC curve is 0.97. These results indicate that the adaptive scheme is superior in the case where the source activity and position are known and the sampling profile is adaptive from the beginning of measurements. A few other pieces of information were also gathered during this study. First as the source moves closer to the detector, the benefits from using the adaptive scheme were diminished. When the source is located at x,y,z = (0,10,250) cm and scaled down to maintain the same detector count rate (α = 15 μCi), the area under the uniform ROC curve is 0.97, while the area under the adaptive ROC curve is 0.97. The advantage for far field imaging in this case comes from the sharper peaks of the transmission function as well as the larger modulation efficiency in the far field. The contrast between the peaks and valleys is much stronger, which translates directly to the strength of sampling in the adaptive scheme.

The positive results from this simulation were encouraging and the next step is to apply the same process to a scene containing an unknown point source. For this scenario the sampling pattern remains uniform until a significant peak or peaks is detected in the scout images. It is at this point that complications arise with this form of adaptive sampling.

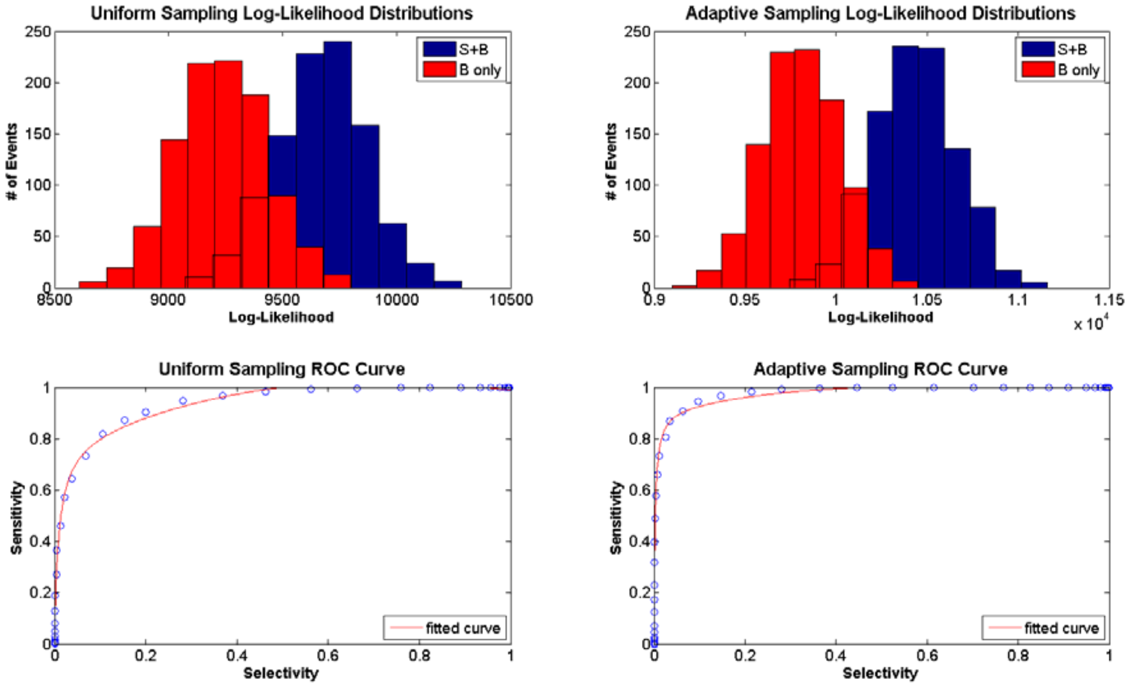

Figure 3-12. The log-likelihood distributions and their associated ROC curves are shown in this figure. The panels on the left assume the uniform sampling scheme, while the panels on the right assume the adaptive sampling scheme. These figures are generated for the case where the source activity and location are known exactly, and the purpose is to illustrate that the adaptive scheme is superior if the true source position can be located quickly. The area under the curve for the uniform scheme is 0.91 and the area under the curve for the adaptive scheme is 0.97.

The rate of false positives in a detection system is directly related to the amount of time spent recording data. For the RMC this is no different, and for data sets with low counts the RMC images have a tendency to contain spurious peaks that meet the SNR requirement, but are not real. Section 4.4 outlines a new method for predicting the time it takes to detect a source using the log-likelihood distributions. In this study, it was seen that when the sampling time is short, the source plus background and background only distributions overlap, as they do in Fig. 3-12. When the data is sparse, the images produced can show a variety of features. Sometimes the image will show true source location, sometimes it will produce a uniform background field, and sometimes it will produce an image with peaks that are not related to the true source location. When the dwell time is adapted using incorrect peaks, the resulting transmission function can become more distorted because the system is searching in the wrong location. When this occurs the adaptive sampling scheme actually performs worse than the uniform scheme.

Several methods were employed to eliminate this problem. In the first scenario the adaptive routine was not allowed to modify the dwell time parameter until half of the allotted measurement time had passed. This allows the transmission function to become better defined before the peak search is implemented. The problem of spurious peaks still persists however with some scans corrupted by the spurious peaks, while others find the true source. Even when the true source is located, too much time is spent on the initial uniform scan that the areas under the two ROC curves are nearly identical. Applying the bootstrap routine to the data could help to smooth out the spurious peaks, but the bootstrap as implemented in this research requires a well sampled set of data. The bootstrap smoothing approach was not yet implemented in this research, but could be a next approach to solving the problem of spurious peaks. Until this problem can be resolved, adaptively modifying the dwell time to locate sources faster is not practical.

3.3 Summary of RMC System Design and Operational Parameters

This chapter outlined the design of an RMC system used to support the research in this thesis. The design phase addressed five primary requirements: (1) RMC structural design including a frame to hold and rotate the masks, (2) the mask design, (3) automation, control, and feedback systems, (4) a data acquisition and processing system, and (5) system calibration.

The section on mask design discussed some of the tradeoffs that must be made between the mask field of view and modulation efficiency. High modulation efficiencies require thicker masks, which reduce the field of view. A large field of view is desired for the orphan source search problem however, so that a large area can be scanned with only a few measurements. It was also shown that making the mask pair asymmetric is sufficient for removing the 180° source ambiguity that is present with symmetric masks.

Measured data from the designed RMC was then compared against predictions from the universal field model. First the transmission functions for sources located 100, 200, 500, and 1000 cm from the detector were generated and plotted against the measurements demonstrating relatively good agreement. The universal field model is then compared against the Wilmore far field model using the measured data. The universal field model produced results with better precision than the far field model at all locations. Additionally the far field model produced a very inaccurate and noisy image when the source was located 100 cm from the detector.

The final portion of this chapter looked at a couple of ways that the RMC can be modified during the course of an experiment to produce better images. It was shown that changing the mask separation parameter allows the RMC to measure different spatial frequencies of a given source scene. By making multiple measurements with different mask separation parameters, it is possible to produce images of extended sources with more complex geometries. Simulations of a rigid ruler and extended T-shaped source demonstrated the effectiveness of this technique. A method was also demonstrated for removing nuisance sources from the image as a way to locate masked weaker sources. In this case a weak source was simulated next to the stronger extended-T source, which effectively masks the presence of the weak source. The RMC transmission function for the T-shaped source is generated and then applied to the unmodulated background term used in the MLEM algorithm. When this technique is applied, the extended-T shaped source is removed from the image and the weak source appears. A negative effect however is that the reconstructed location of the weak source is biased by ~4cm. The bias is introduced by statistical noise from the extended T source, which is not suppressed using this technique. The magnitude of the bias is related to the strength of the nuisance source relative to the orphan source. If the nuisance source is very strong (compared to the orphan source), then the bias will also be large. The bias is small if the orphan source is strong relative to the nuisance source. More research needs to be conducted in this area to quantify the relationship between the bias and the nuisance source strength.

The final topic of Chapter 3 was adaptive imaging techniques. When the source activity and position are known, adaptive sampling is superior to uniform sampling based on the area under ROC curves generated using the log-likelihood distributions. It was also seen that the adaptive sampling performance deteriorates as the source moves closer to the detector. This results because the transmission function of the known source becomes compressed and smoother at near field distances. The shape of the transmission function is used to adapt the dwell time parameter, which explains the loss of performance in the near field. Adaptive imaging for the unknown source scenario becomes much more difficult. Spurious sources produced by a sparse data set easily confuse the algorithm, which can begin searching in the incorrect location. The result is that the adaptive scheme often performs worse than the uniform scheme. An attempt was made to fix this by constraining the adaptive algorithm so that it can not modify the dwell time until half of the total measurement time has passed. This allows the source plus background and background only distributions some time to separate. Unfortunately the spurious source problem still exists although less frequently. When the source is correctly identified however, the area under the ROC curves for both the adaptive and uniform schemes are nearly identical.

CHAPTER IV

MEASURED PERFORMANCE OF AN RMC FOR THE ORPHAN SOURCE SEARCH PROBLEM

This chapter looks at the measured and simulated performance of a single RMC as described in Chapter III. The results are then used in Chapter V to assess the capability of an RMC system for the orphan source search problem. The first section of this chapter focuses on the response of the RMC when there are no sources present in the system field of view and the only signal is the unmodulated background. The ML methods presented in Chapter II produce a different set of results given different assumed background intensities. Incorrectly modeling the unmodulated background can result in incorrect source activity and position estimates.

The second section looks at the system response to a single point source both inside and outside the field of view in three dimensions. First, the system accuracy and bias for a point source in two dimensions (ρ and ϕ) is measured, and the system response as a function of source location within the field of view is discussed. Next several methods for estimating the depth position are presented as well as the limitations of accurately estimating this coordinate.

The third and final section in this chapter discusses the system response when two or more point sources are located in the system field of view. Initially the sources are assumed to be the same isotope (i.e. emitting the same energy photons). The system angular resolution is measured and compared against theoretical and simulated results and the impact of multiple sources on the position accuracy and bias is considered. Also the dynamic range is measured and the results are compared to theoretical predictions discussed in section 2.4.2. The last portion of this section highlights the system response when multiple point sources with different energies are measured.

4.1 RMC Response to an Unmodulated Background

Characterizing the RMC system response to the unmodulated background is important for understanding the response when a source is in the field of view. Before continuing, it is important to describe what exactly is meant by the background in this thesis. For mechanical imaging systems, the system background is often broken into two separate components [Smi98]. The first component is an unmodulated background that is caused by sources that are located outside of the system field of view and is represented in Eq. 2.1 by the energy dependent symbol b(E). Because this background is unmodulated, it will cause a shift in the dc level of the RMC transmission function resulting in additional statistical noise. The second background component comes from sources that are located in the system field of view and is caused by photons that penetrate the masks and are detected. This background is also unmodulated, but is accounted for by the system model when mask penetrations are properly modeled as discussed in section 2. The final section of chapter 4 discusses results from measurements of the RMC detection time. Using the log-likelihood distribution methods described in sections 2.4.4 and 3.2.3, a simulated RMC system viewing a source scene is compared against a RMC system viewing a background scene. It is shown that the separation between the source plus background and background only scenes can be used to determine the minimum amount of scanning time that is required to detect a source of a known activity. This information is useful for understanding the detection limits of the RMC. Closely associated with the mask penetration background is the down scattering background from higher energy sources. In this case photons from a high energy source scatter off of the mask and in the detector itself. These down scattered photons add background to the lower energy bins. These down scattering effects will be discussed further in section 4.3.3. There is a third understanding of background that must also be clarified at this point. This background is in reference to noise in a reconstructed imaged caused by nuisance sources located in the field of view. This background component was presented in reference to extended source in section 3.2.1, and several methods were presented for properly modeling its effects on the system response. The focus of the next section is on the first background component; the unmodulated background from sources outside the system field of view.

4.1.1 Known vs. Unknown Uniform Background

When no sources are present in the RMC field of view the only contribution to the RMC transmission function is the uniform background, which will be Poisson and distributed about the mean background level. This unknown background can be either a known or unknown quantity. The known background scenario might be encountered if the RMC were set up in a fixed location such as a remote border crossing or as part of a monitoring network at an industrial site. The detector spends most of the time recording the assumed background and it is not until an event occurs (car passes in front of the detector, site accident with release of material) that sources are injected into the field of view. Figure 4-1.c shows the reconstructed image when a uniform background field is measured and the true value of the background is used in the MLEM algorithm. Because the MLE is influenced by the presence of a source, the values for each pixel are near to zero, indicating there is no source present. Furthermore, the SNR for the image is distributed about one, which also confirms that absence of a source. Figure 4-1.a and c highlight the effect when the background is either under- or over-estimated by the user in the MLEM algorithm. In the case of underestimation, the MLEM algorithm assumes that counts not attributed to the additive background, are considered source counts. This means that for a single source estimate, underestimation of the background can produce peaks in the image that aren't related to actual sources as shown in Fig 4-1.a. This is remedied by applying the bootstrap technique to the data. Because the peaks are not caused by any particular source, they are instead numerical aberrations and will change from image to image. When the bootstrap method is applied, the mean image generated from multiple realizations (Fig 4-1.b) is distributed in a fashion similar to the exact background case in Fig 4-1.c. The value for each pixel in this mean image however, is higher than the exact case, again because the excess counts not attributed to background must be placed somewhere. The issue is resolved by considering the SNR of the mean underestimated image, which is distributed slightly above 1, indicating no source is present.

When the background is overestimated, the large background term in the MLEM algorithm (Eq. 2.29) reduces the impact of the source term Aλ. This effect is seen in Fig 4-1.d where the number of counts in each pixel is on the order of 1x10^{-3}. These pixel values will decrease linearly as the overestimation of the unmodulated background increases. Unlike underestimation, overestimation will always produce a background response similar to the exact case, with a SNR that is distributed about 1.

Besides producing numerical aberrations when no sources are present, both over- and underestimating the unmodulated background has an impact on the source activity estimate when sources are present. When the background is overestimated the activity estimates of a real source are biased low. Conversely, when the background is underestimated the activity estimates are biased high. This is problematic for the orphan source search in three dimensions when using the RMC. In order to constrain the possible range of solutions, source activity is often constrained to a range of acceptable values. This technique is applied in section 4.2.2 as a method for estimating the depth coordinate of the source. If the bias on the activity estimate caused by a poorly modeled background is high or low enough, it could push the source out of a window of acceptance. The effect is a reduction in the overall sensitivity of the system.

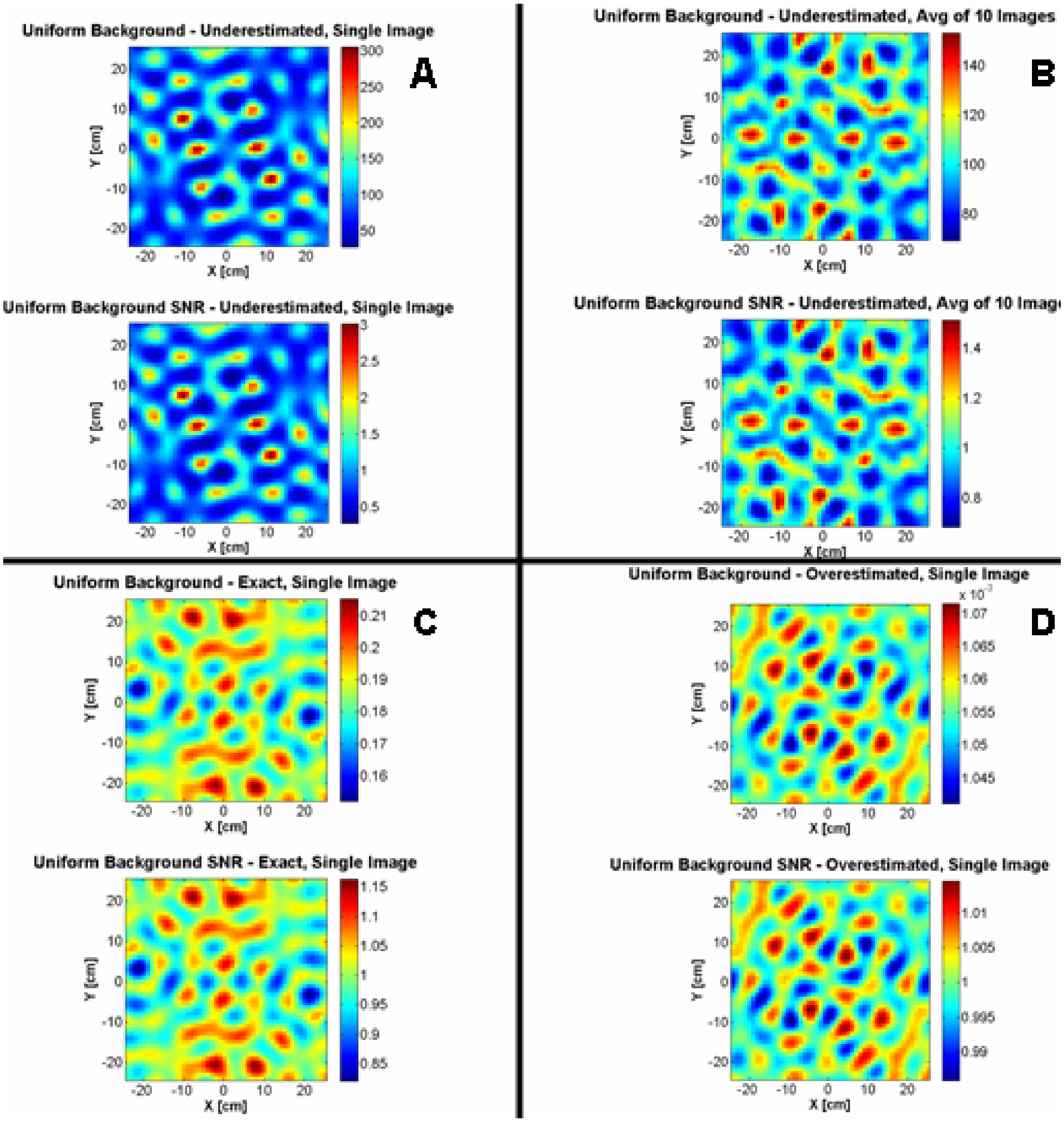

Figure 4-1. Shown is the simulated RMC response to a uniform background, when different values are assumed for the background in the ML-EM algorithm. Plot (A) shows when the background is underestimated for a single image, producing a slightly elevated SNR. This can be resolved by using the bootstrap method to generate multiple images (B) and using the mean image to produce a SNR, which is ~1. Plot (C) is the MLE when the assumed background for the ML-EM algorithm is exact, and (D) shows when the background is overestimated.

4.1.2 Measuring the Unmodulated Background

Measuring the unmodulated background can be done in several different ways. If the RMC is a stationary system that is constantly monitoring a fixed region the unmodulated background can be derived from background measurements made before point sources are injected into the field of view. Another scenario is one where the RMC is brought in to a previously unmeasured region and tasked to locate orphan sources. In this case a measurement can be made with solid lead plugs in place of the masks. These plugs will block any photons entering the RMC from the field of view. The measured background will then only come from sources located outside the system field of view.

4.2 RMC Response to a Single Point Source

4.2.1 Measurement of RMC Accuracy and Bias for a Single Point Source in Two-Dimensions

The simplest task for an RMC is to locate a single point source in a uniform background. The purpose of these first measurements is to identify the position accuracy of the RMC in the radial and azimuthal directions. A two-dimensional mapping of the system is accomplished using a 2 mCi Ba-133 source located 215 cm from the front mask of the detector. The source was mounted on the Velmex bi-slide stepper shown in Chapter 3 for accurate source positioning. The system response is then measured at a variety of positions within the right lower quadrant both inside and outside the system field of view. Due to the symmetric nature of the system, the mapping of a single quadrant is sufficient to determine the system response in the other quadrants. Table 4.1 lists several parameters that were used in this experiment.

Table 4-1. Experimental Setup for 2-D mapping of the RMC response to a single point source.

SCA Window Settings		Background Rate [cps]	Total Scan Time [sec]	Mask Separation [cm]
Lower Level [V]	**Upper Level [V]**			
1.33	1.63	15	360	24

For each map location the standard deviation on the position estimate is obtained using the bootstrap procedure outlined in section 2.4.3. The results from these measurements are best explained by looking at three distinct response imaging zones.

The first region is a blind zone that starts at the center of the RMC FOV and has a measured extent equal to the theoretical resolution of the RMC given in Eq. 2.22. When the source is located at $\rho=0$ (i.e. RMC centerline) the RMC transmission function is flat because the masks remain stationary as viewed by the source. Because of this flat pattern is it impossible to distinguish a source located on the central axis from background when using a single RMC. As the source moves off axis, the transmission function begins to develop but is not fully developed until it is past a certain threshold given by the RMC angular resolution Eq. 2.22. Due to weak modulation and statistical noise on the data, the location of sources in this region can be difficult if not impossible to estimate. Figure 4-2 shows the results of mapping data points every cm in x-, y- and x-y. From the data it is seen that the RMC blind spot (L=24 cm) extends to ~0.7°. Additionally, the region from 0.7 to ~1.0° could be said to be fuzzy, since the position estimate is still not accurate, but is clearly approaching the true position. The theoretical angular resolution for the system (p=8 mm, L=24 cm) is 0.955°, which matches very well with the measurements.

Because the width of the blind zone is defined by the system resolution, the simplest way to minimize its extent is to reduce the slit pitch or increase the mask separation at a cost of field of view. Multiple RMCs or taking measurements with overlapping fields of view can also be employed to completely eliminate the blind zone.

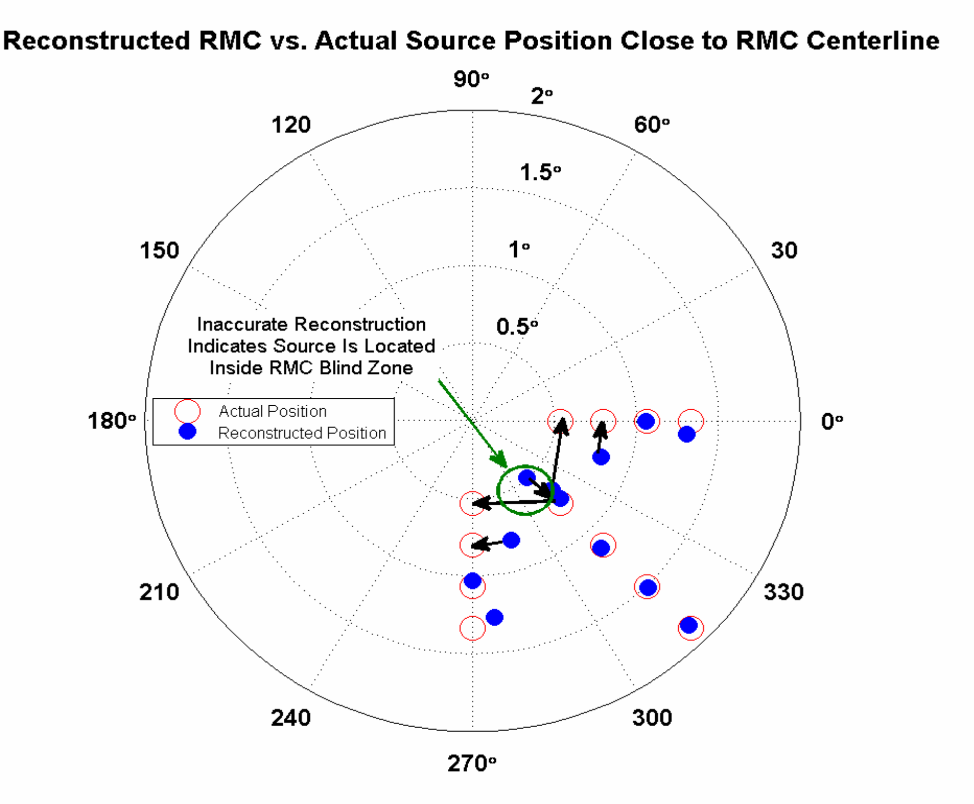

Figure 4-2. The RMC blind spot is illustrated here as the region from ρ=0 to ~0.7°, where the modulation pattern is too uniform to allow for accurate reconstructions. The system resolution, which defines the width of the blind zone is 0.955° and matches well with the measured data.

Once the source is located outside the blind zone the RMC transmission function takes on the distinct RMC pattern with the low frequency dip, and MLEM reconstruction typically provides a very accurate position estimate. Figure 4.3 shows the RMC map for sources located in this active region, and with the exception of the source measured at ρ=0, all of the position estimates are very accurate. Table 4.2 summarizes some of the key statistics for this data generated using the bootstrap method discussed previously.

The data in Table 4.2 demonstrate the RMCs ability to pinpoint the location of the source with a very high level of accuracy. As reported by Schnopper et al. the uncertainty in the azimuthal angle is higher than the radial position, which can be understood by referencing the transmission function shown in Fig. 2-13 [3]. The radial position information is contained in the periodic peaks, while the azimuthal position information is contained in the broad dip. When counting statistics and background are considered it is obvious that the broad dip will be less resolved than the peaks, leading to higher uncertainty in azimuth, ϕ.

Table 4-2. Statistics of Interest for RMC Position Estimation in the active sensing region.

	Max Error	**Avg Error**	**Max Std Dev (1σ)**	**Avg Std Dev (1σ)**
ρ **[arc min]**	3	-0.24	2.01	1.12
ϕ [deg]	6	0.16	4.56	2.44

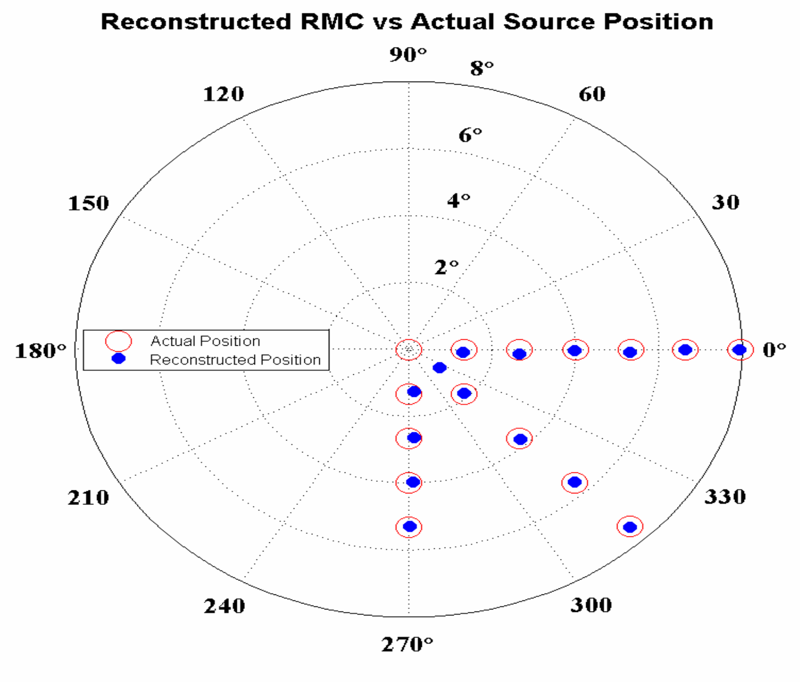

Figure 4-3. In the RMC active sensing region, position estimation using the MLEM algorithm is very accurate. With the exception of the source located at ρ=0, the average standard deviation on the position estimate for sources located between the blind zone and field of view edge is ~1.6 arc minutes.

The final region of interest is for sources located outside of the RMC field of view. Once the source moves beyond the two-mask FOV, the projection of the front mask no longer overlaps the rear mask and detector. Photons still hit the rear mask however, and for masks with finite thickness they will be slightly modulated as the RMC rotates producing a transmission function like the one shown in Figure 4-4.

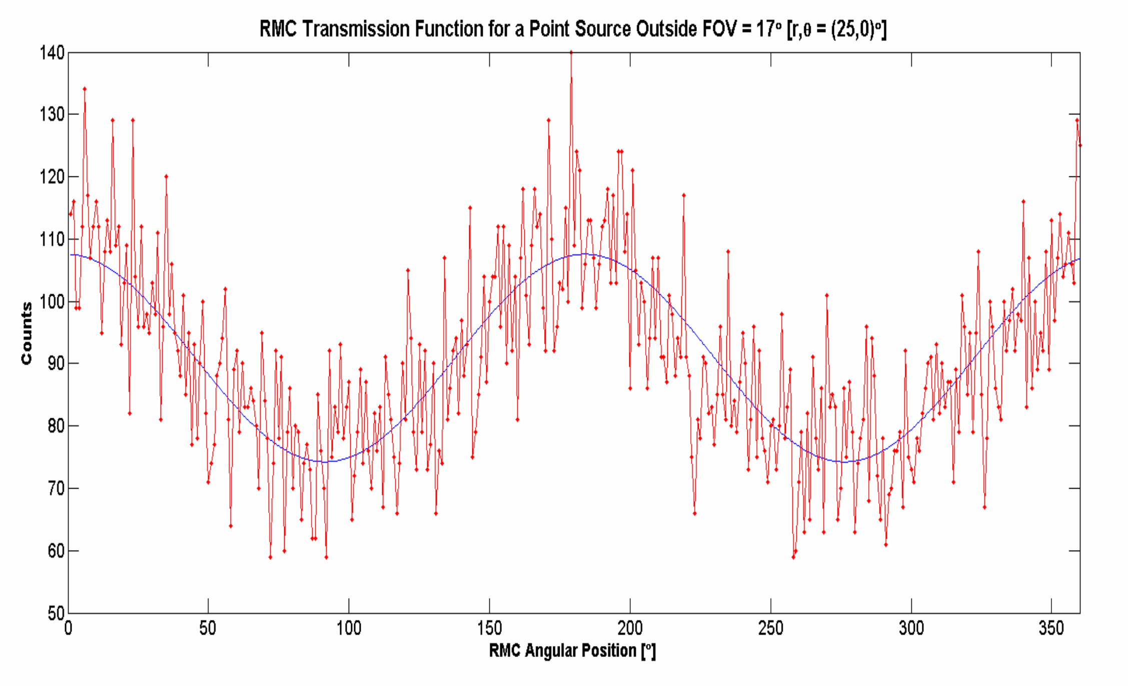

Figure 4-4. A slight modulation occurs for sources outside the system FOV (Eq. 2.32) that is caused by photons passing through the single mask closest to the detector. In this figure the source is located at ρ,ϕ = (25,0)°, while the FOV is ~17°.

Through a simple inspection of geometry, it is possible to define the single mask field of view as

$$FOV_{mask} = 2\arctan\left(\frac{s_{\max}}{2t}\right), \qquad 4.1$$

where $s_{\max}$ is the length of the longest mask slot and t is the mask thickness. For the masks in this experiment, the longest slot is 6.693 cm producing a single mask field of view of ~138°. Unfortunately the transmission functions in this region are too ill defined to produce a point location estimate using the MLEM algorithm. It was found however, that when only a few iterations of the MLEM algorithm are used, the general direction of the source in this region becomes known as shown in Fig. 4-5.

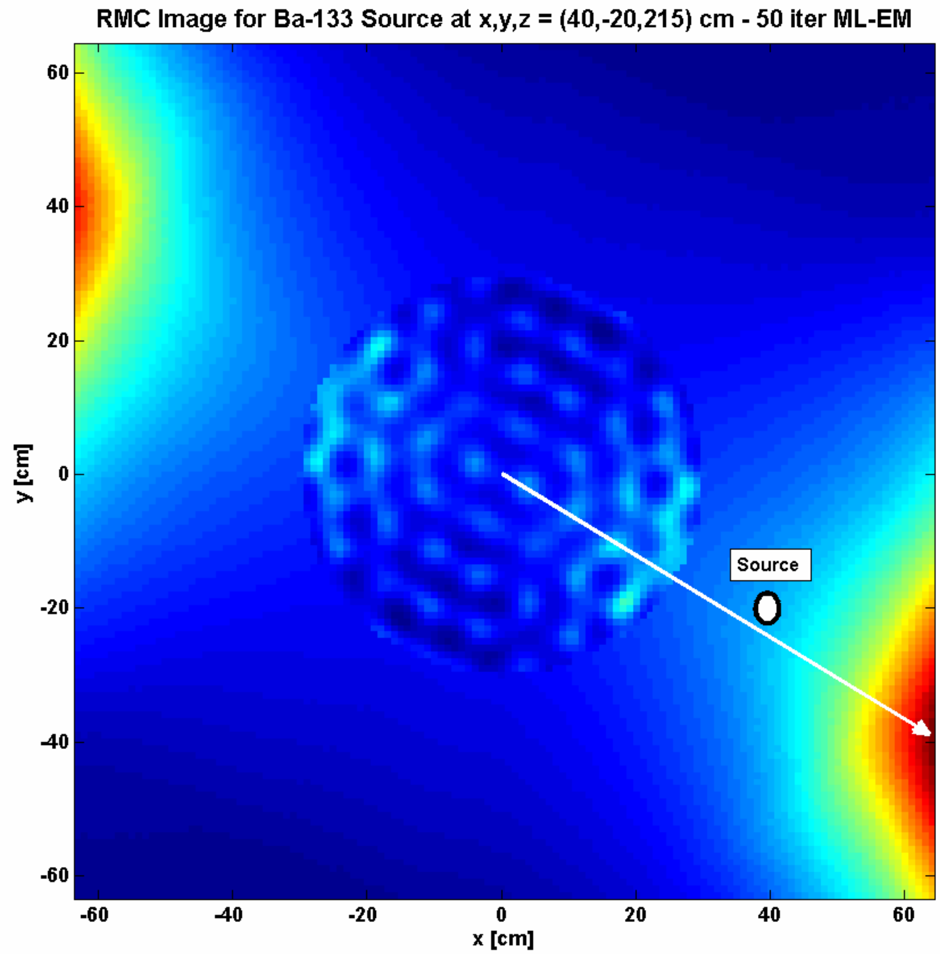

Figure 4-5. Result from 50 iterations of ML-EM algorithm for a source at x,y,z = (40,-20,215) cm. The point location estimate is not produced, but the broad edge region does point in the direction of the source shown as a white circle.

This general pointing information could presumably be used to position the RMC for a subsequent measurement. As the source moves further off axis toward the edge of the single mask field of view, the modulated component becomes increasingly small until it moves into the unmodulated background region. At this point the transmission function is a constant as discussed previously.

4.2.2 Estimation of the Depth Coordinate and Associated Accuracy and Bias

One of the desired goals for moving to a universal field model was the added capability of estimating the source depth coordinate using a single RMC. Referring again to Eq. 2.1, the two variables that are depth dependent are the RMC transmission function and the solid angle. Figure 2.8-9 show that near to mid range sources (1-10 meters) produce transmission functions similar to the far field model, except they have lower overall modulation efficiencies due to the effects of magnification and the finite thickness of the masks. Furthermore when the magnification is greater than a certain threshold (~ >1.125), the transmission function is stretched out so that the peaks no longer align with the far field model peaks. It is apparent that when the source is in this mid-field region that the transmission functions are at least somewhat unique as a function of depth. This is further tested by comparing the log-likelihood distribution using the universal field model against the log-likelihood distribution using the far field model.

In this particular comparison, the only difference is the system models used to generate the transmission function. The log-likelihood values are generated using only the transmission functions, assuming that α=1000, b(E)=0, ε=1, and τ_n=1 and is uniform for all bins (listed variables are defined in Eq. 2.1). Simulated data sets are generated by computing the transmission function using the above parameters and then using the Matlab command ‘poissrnd’ to add counting statistics noise to the data. The polar position of the source was fixed at (2.87,0)°, which causes the transmission functions to be similar in structure at all distances from the RMC. In theory, when the universal field model becomes identical to the far field model, the distributions should overlap completely. Figure 4-6 shows an example of the transmission functions (a) and separation between the distributions (b) when the source is located 200 cm from the RMC.

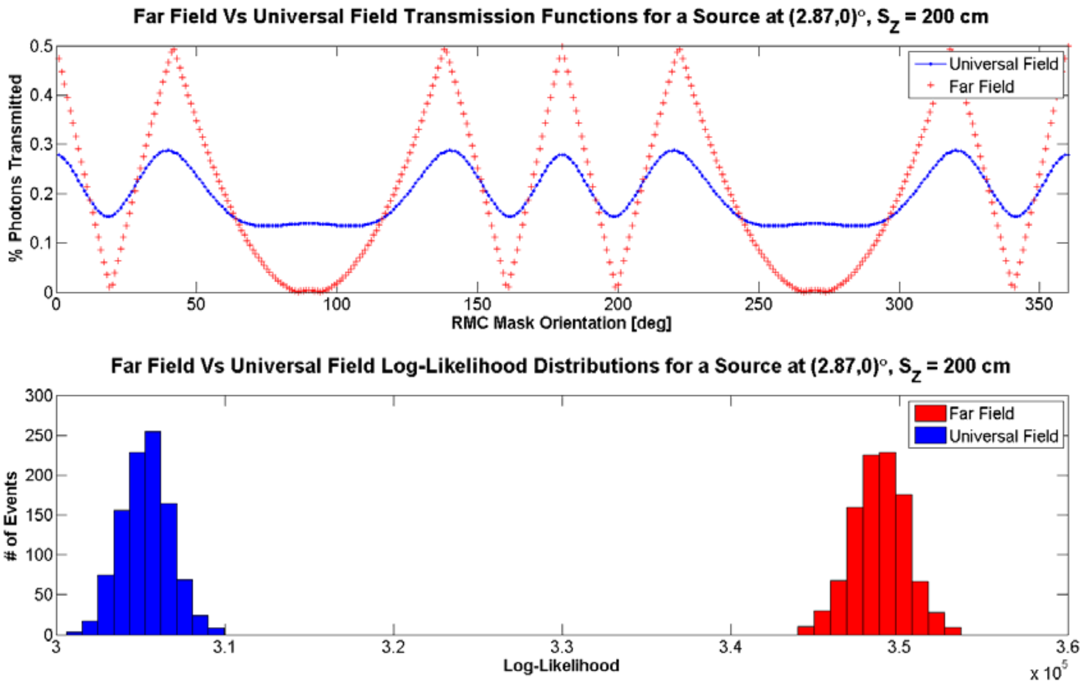

Figure 4-6. The difference in the universal and far field models for a source located at (2.87,0)° and 200 cm is apparent in both the transmission functions shown in the top plot, and in the distributions of the log-likelihood value for both models. As the source moves further from the RMC, both transmission functions begin to appear the same and the separation between the distributions decreases. At very large distances the universal and far field models are identical, and the distributions overlap completely.

The similarity (or difference) between log-likelihood distributions is quantified by taking the ratio of the distribution means at a fixed distance. Again, when the two models are identical the mean for each distribution should be approximately equal and the ratio should approach one. As the models diverge, the ratio should head asymptotically toward 0. Figure 4-7 shows the how the distribution mean ratio changes as a function of the distance parameter S_Z.

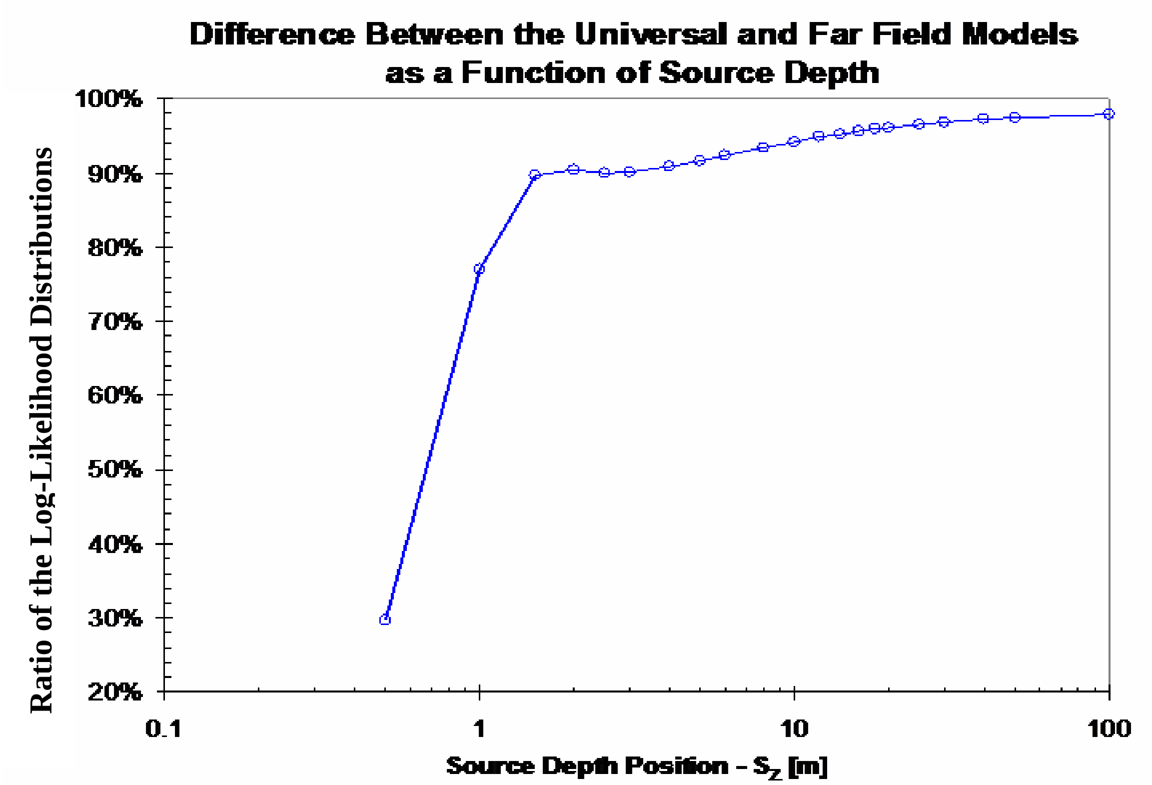

Figure 4-7. This plot illustrates the difference between the universal and far field model as the source moves from the near- to mid- and finally far field.

Figure 4-7 confirms that there is a dramatic difference between the universal and far field models when the source is located less than 200 cm from the RMC. This is consistent with the visual inspection of the transmission functions seen in Figs. 2.8-9 and Fig. 4-6, where the peaks in the transmission function become stretched to different positions in the near field. These results imply that the far field model is not suitable for image reconstruction in this near field region, which occurs when the magnification is greater than 1.125.

When the source moves out of the near field into the mid-range field (>200 cm) the change in the ratio of the log-likelihood mean as a function of S_Z is much less dramatic. A more useful comparison at this point is the difference in the mean log-likelihood ratios between two different planes. This is shown in Figure 4-8, which compares the relative differences between the transmission functions at various depths. This figure is understood by choosing a fixed reference distance S_Z and then considering how much difference exists between the transmission function at this depth and at different depths.

Each plotted function in Fig. 4-8 will equal zero when the function equals the reference distance.

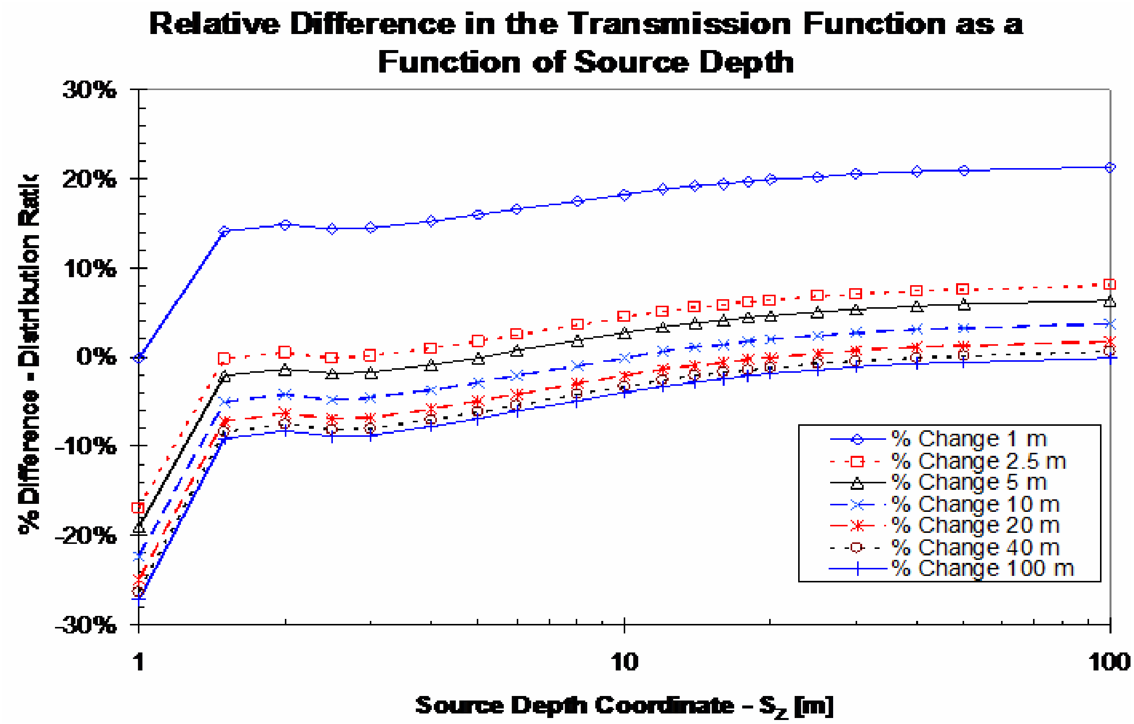

Figure 4-8. This figure illustrates how the RMC transmission functions change as the source moves from one depth to another, by considering the difference between the different log-likelihood distribution mean ratio. The two most important characteristics to note are that for near field sources the RMC transmission function changes dramatically as a function of depth. As the source moves very far from the detector, the change in the transmission function versus a change in depth is very small and approaches the far field limit.

Figure 4-8 also illustrates the large difference between near field and mid-field transmission functions. The top line in the figure (reference plane equals 100 cm) shows that going from 100 cm to 150 cm produces a 15% change in the log-likelihood function. Furthermore, the change in the transmission function past 150 cm is much more gradual, with a change of less than 1% in the log-likelihood function when going from 150 cm to 400 cm. The 10 meter curve shows that the change from 10 meters to 100 meters results in a change in the log-likelihood function of less than 4%. This effect is also illustrated by studying the trend in the curves as the reference plane moves further from the source. The curve at 40 meters is not that far separated from the curve at 100 meters, and it is apparent that the curves are converging toward a true far field condition. For depth position estimation these curves can help provide insight into the limits of converging on a true solution. This will be demonstrated using a series of measurements that were taken to test the ability of the RMC to locate a source in three dimensions.

In this experiment, a set of eight independent measurements using the RMC system were taken. For these measurements, a 1.7 mCi Ba-133 point source was measured at distances of 100, 200, 300, 400, 500, 600, 800, and 1000 cm from the front mask of the RMC. At each distance, the source was located at approximately $\rho,\phi = (2.87,0)°$, so that the transmission function is consistent across all measurements. The minimum sampling time was fixed at 360 seconds, which was used at distances of 100, 200, 300, and 400 cm. In order to record a sufficient number of counts at greater distances, a scaling factor was applied to the acquisition time for the distances beyond 400 cm. The scaling factor is a simple $1/r^2$, which ensures that the total number of photons recorded at the far distances is approximately equal to the number recorded at 400 cm.

Because this experiment did not use the Velmex source positioning system, the source had to be repositioned for each measurement. The experimental arrangement is shown in Fig. 4-9. First the centerline of the RMC was referenced with respect to the nearest wall and the floor. A laser capable of projecting a straight line onto the floor was attached to the flight tube and aligned with the RMC centerline. Tape was then placed on the floor along the laser line to indicate the pointing orientation of the RMC. The depth coordinate was measured by attaching a laser range finder with an accuracy of ~0.5 cm at 50 m to the source holder. The source holder was then moved away from the RMC along the tape line, while distance measurements were taken. A piece of tape was then placed when the source holder was at one of the positions listed above. Once these positions were marked out, the source was mounted on the source holder and the distance from the source to the floor was adjusted so that the angle between the RMC centerline and a vector formed from the source to the center of the front mask was ~2.9° ± 0.5°.

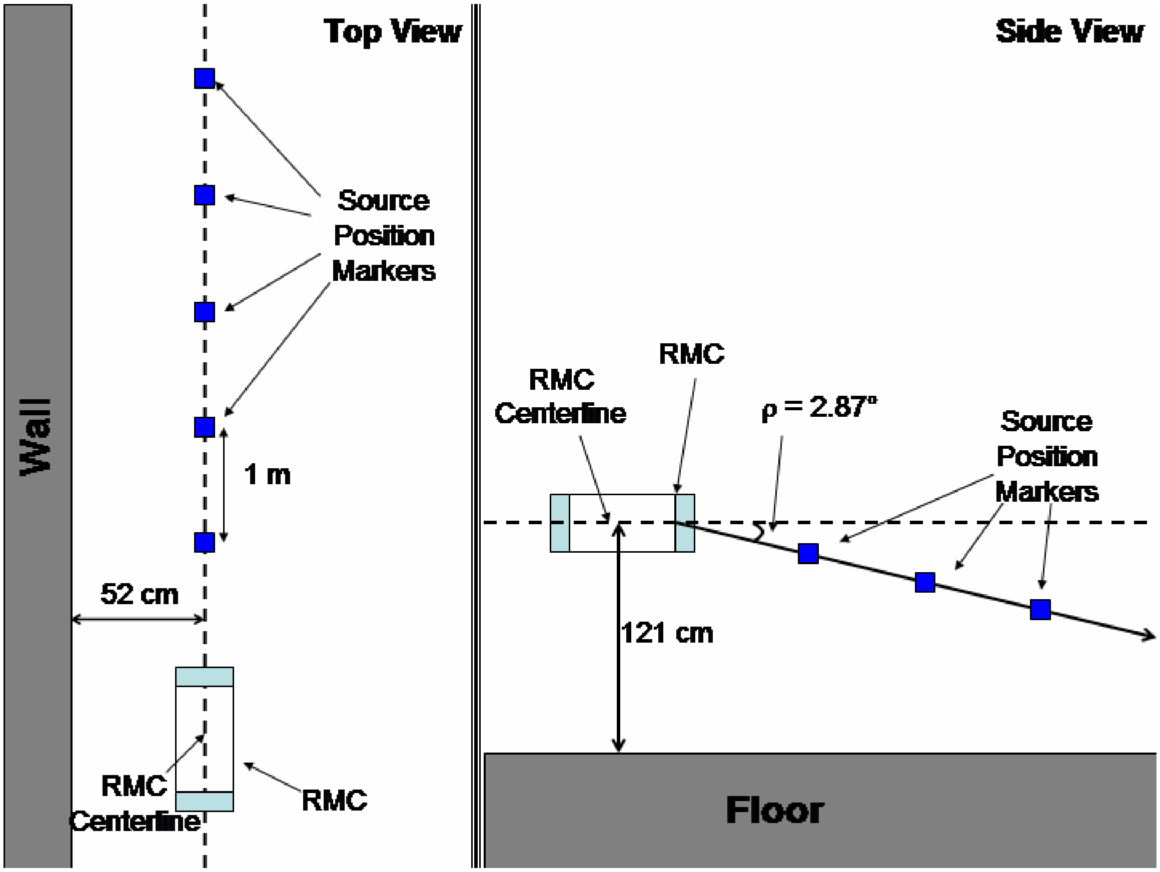

Figure 4-9. This is the experimental setup used to test the ability of the RMC to locate point sources in three dimensions.

Several different reconstruction methods were tested with the measured data to see which would produce reasonable estimates. The first method applied was the MLEM algorithm. In order to generate the system matrix for the MLEM algorithm, the predicted detector response was computed at 10 different depths ranging from 100 to 1100 cm in increments of 100 cm using the universal field model. Each plane was then divided coarsely into 21x21 pixels, with the size of the x- and y- dimensions set by distance from the source to the RMC. For example, when z equals 100 cm, the x- and y- pixels are 1x1 cm, but when z equals 500 cm, the x- and y- pixels are scaled appropriately to 5x5 cm. The goal with this method is to try and generate an image map for the entire 3D space described by this system matrix. Figure 4-10 shows 10 different slices of the reconstructed image, when the source was located 500 cm from the RMC. The algorithm was run until the change between iterations was less than 0.1% in all pixels.

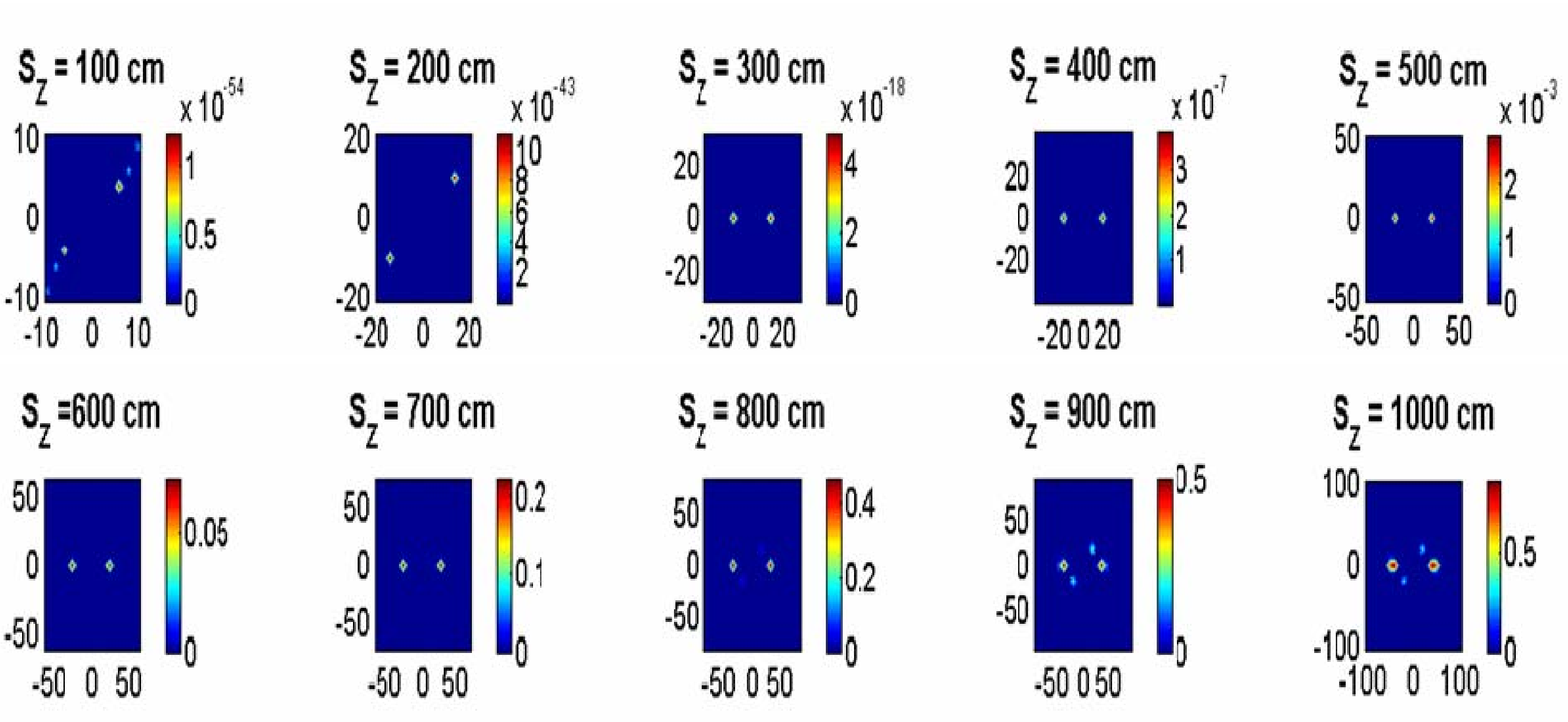

Figure 4-10. Shown above is the MLEM image using 20x20 pixels and ten image planes from S_Z=100 to 1000 cm. The true source position is ρ,ϕ,S_Z = (2.87°,0°,500 cm) and the activity is 1.7 mCi (corresponding true image is shown in the red box). Every image with the exception of S_Z=100 cm accurately predicts the polar coordinates ρ and ϕ, while the depth and activity estimates remain ambiguous. The colorbars on each image have units of mCi. It is apparent that this method alone is insufficient to locate the source in 3D.

The images shown in Fig. 4-10 show that applying the MLEM method alone is not sufficient for estimating the depth coordinate and source activity. The first two images at S_Z = 100 and 200 cm produce somewhat expected results, because the transmission functions at these distances are significantly stretched due to magnification effects. There is some discrepancy however, because the ϕ coordinate should still equal 0 even with magnification considered. At all other depths however, the polar coordinates shown in the images correspond to the true source location of (2.87,0)°. Unfortunately based on these images, there is no clear indication which depth is the correct position of the source. This is not surprising given the relative separation between the log-likelihood distributions given in Fig. 4-8. The distributions indicate that there is a difference of less than 5% between the log-likelihood distribution at 300 and 1000 cm. It is interesting to note however, that the two final images in Fig. 4-10 at 900 and 1000 cm, begin to show some additional noise, and the peaks in the 1000 cm image are slightly broadened. This indicates that the data favors a source position somewhere between 300 and 800 cm.

Another problem with these images is that the source activity estimates are not correct. The colorbar in the 500 cm image (true source position – red box) should show that the peak has a value of ~1.7 mCi, but instead indicates the maximum peak value is ~$3\text{x}10^{-3}$ mCi. This appears to be directly related to the problem of trying to solve an underdetermined system. Each of these measurements consisted of 360 data points (knowns), but the system matrix described has 4410 unknown elements. This hypothesis is tested by breaking the problem up into eleven independent MLEM runs. Each run is performed at a fixed distance from the RMC, so that the first run assumes the source is located at 100 cm, the second run at 200 cm, and the other runs at their respective distances. The system is still underdetermined (441 unknowns), but not as badly as before, and the results from this test are shown in Figure 4-11.

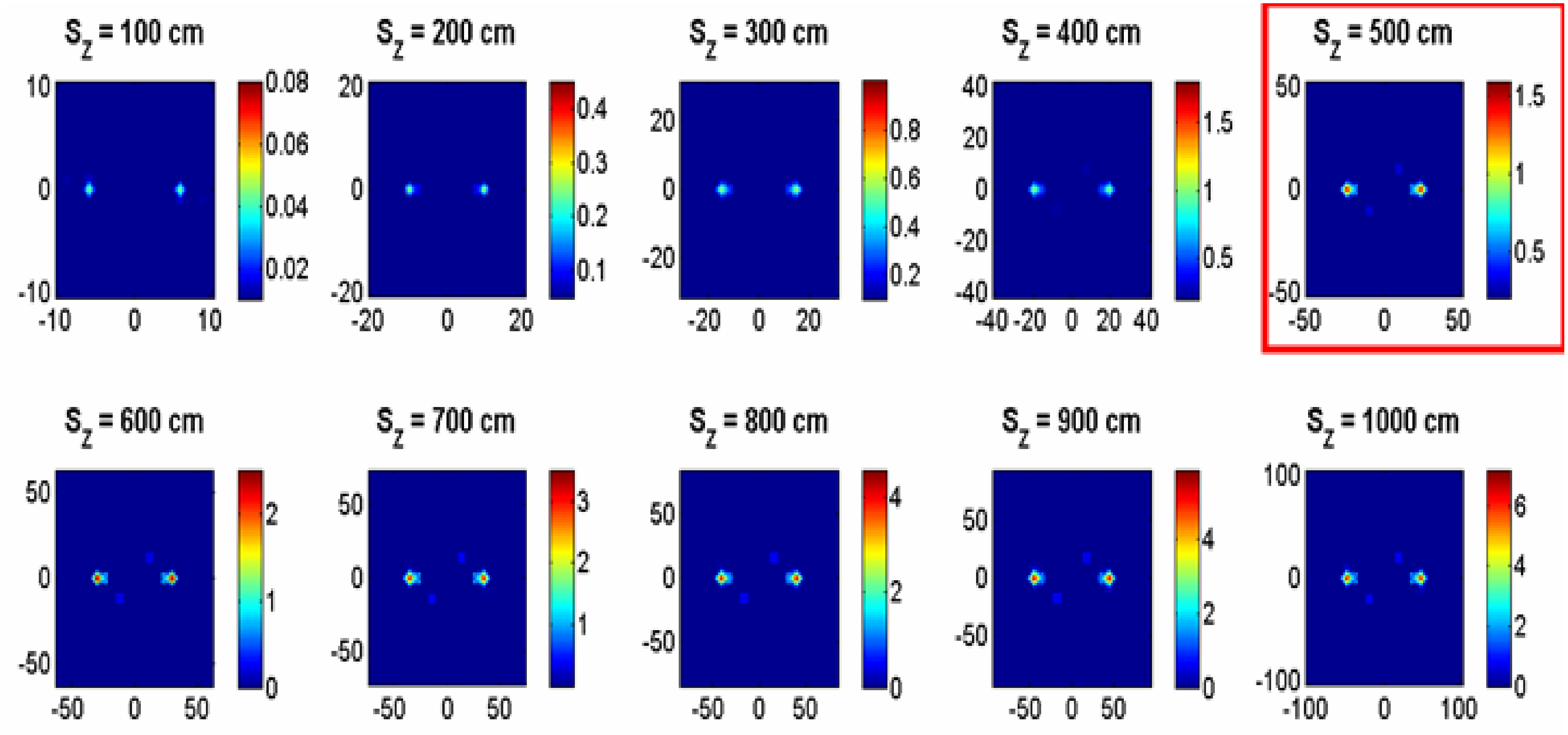

Figure 4-11. The above images are generated by executing 10 independent runs of the MLEM algorithm, at a fixed source to detector distance. Unlike Fig. 4.10, the true source position is reflected in all images. Additionally, the images are less resolved at distances less than the true source position shown by the red box. This can be used to constrain the depth coordinate search to distances above this cut line.

The first issue to note from Fig. 4-11 is that all of the images now show the correct position, although the radial coordinates at 100 and 200 cm are larger than the true source position of 2.87° which is expected again due to peak stretching caused by magnification. The source activity estimates are also correct, with the estimate in the 500 cm image (red box) equal to 1.71 mCi. Another beneficial feature is that the images are not as resolved in the imaging planes where S_Z is 400 cm or less. This indicates that this method has some sensitivity to the true depth position based on how well the images are resolved. As a test of this theory, the same MLEM procedure is applied, but the 1000 cm RMC measurement is now used. In this case, the images are less resolved below at distances below 600 cm. This method could be used to at least provide a lower bound on the true range of the source. An upper bound can be set based on the source activities. Consider for example the image shown in Fig. 4-10, when a 1.7 mCi source is located 500 cm from the RMC. The change in activity from image to image scales at $1/r^2$. Therefore, if the source were located 2000 cm from the detector, it would require an activity of ~27 mCi in order to produce the measured transmission function. In many cases such as the ruptured source in Juarez, Mexico in the introduction, the activity of the sources may be a known quantity. In this case, the search can be limited by stating that only sources between certain ranges are realistic. Therefore the upper limit on the distance is set by an upper activity bound. This information can also be used with another ML technique to further pinpoint the true source position.

The information provided by the MLEM method can be used to constrain the problem so that a gradient search algorithm like the one outlined in section 2.3.2, can be used to find a more precise estimate of the source activity and depth coordinates. As discussed in section 2.3.2, ‘fmincon’ is a non-linear gradient search algorithm in Matlab that attempts to find a minimum value of the negative log-likelihood function given the measured data set. Because there can be many local minima in the map of the log-likelihood function it is necessary to start the algorithm in the vicinity of the true source position in order to converge on the true result. Fortunately ρ and ϕ are known from the MLEM algorithm and potential a priori knowledge about the source scene can be used to set a range on realistic source activities.

The method uses the values of ρ and ϕ provided by the MLEM method for each of the eight measured data sets. The source activity is bounded between 0.1 and 2 mCi and the depth dimension is bounded between 100 and 1200 cm. The initial guess for the activity and depth coordinate are selected at random from the respective bounded intervals using the Matlab command 'rand', which selects a random number between 0 and 1 on a uniform distribution. The gradient search routine is executed 10 times, with the initial guess changing at each execution. The reasoning behind this decision is an attempt to negate problems associated with selecting a starting point near a local minimum that is not the global minimum. For example, suppose that a local minimum was located near S_Z = 400 cm and the initial guess were always set to 400 cm. There is a possibility that the gradient search would always converge to that local minimum value, even though the source was really located at 500 cm. By randomizing the starting location and running the routine multiple times, these local minima traps are more likely to be avoided and can at least be quantified by looking at the standard deviation of the mean estimate. Table 4.3 shows the results when the gradient search method is applied to the eight measured data sets.

Table 4-3. This table shows the depth and activity estimates for eight measured data sets taken at various distances from the RMC. The results were obtained by taking the mean of 10 different runs of the Matlab gradient search algorithm 'fmincon', when the initial starting guess for both depth and activity were selected randomly. The polar coordinates ρ and ϕ for each data set are found using the MLEM procedure shown previously and then used as inputs to the gradient search routine.

S_Z Actual [cm]	S_Z Estimate [cm]	S_Z Standard Deviation [cm]	S_Z Bias [cm]	Activity Estimate [mCi]	Activity Standard Deviation [mCi]	Activity Bias [mCi]
127	143.44	15.85	-16.44	1.67	0.412	0.030
227	221.75	22.51	5.25	1.42	0.340	0.276
327	280.17	43.22	46.83	1.23	0.427	0.474
427	403.75	90.73	23.25	1.46	0.622	0.236
527	425.44	105.86	101.56	1.16	0.587	0.537
627	530.09	86.87	96.91	1.37	0.472	0.333
827	604.23	132.42	222.77	1.12	0.495	0.577
1027	696.88	165.66	330.12	1.16	0.528	0.541

The data in Table 4.3 indicate that the estimates are fairly accurate when the source is located within 4 meters of the RMC system. As the separation distance increases the depth and activity bias and standard deviation trend upward and become very inaccurate when the source is greater than 8 meters from the RMC. In fact, the estimates shown in Table 4.3 correspond very well to the cutoff point found using the MLEM method and highlighted in Fig. 4-11. For example when the 827 cm data is analyzed using the MLEM method, all of the images below 600 cm are much less resolved than the images above 600 cm. This corresponds very well to the 827 cm depth estimate in Table 4.3 of 604.23 cm.

This information can be used to further constrain the gradient search routine so that the only acceptable range is above 600 cm. When the depth constraint is further tightened for a source located 827 cm from the detector, the position and activity estimates are 846 (120) cm and 1.6 (0.4) mCi respectively (values in parentheses are standard deviations). Unfortunately as the source moves further from the detector this method begins to fail as well. When the 1027 cm data is constrained to only the range above 700 cm, the depth coordinate and activity estimates are 863 (150) cm and 1.46 (0.5) mCi respectively. Although this is better than the estimate shown in Table 4.3, it is still biased 164 cm below the true position. This indicates that this method for estimating depth is good for discriminating sources in the near-mid range, but begins to fail as the source heads toward a far field condition. This makes sense intuitively because in the far field the photons hit the mask as parallel rays and there is no depth information provided.

Finally, it should be noted that if the polar position coordinates are known (from the MLEM algorithm) and the source activity is known (searching for a particular known source), then this method can provide a very accurate depth coordinate estimate for a single point source. Consider again the case where the source is located 1027 cm from the detector and the activity is known to be 1.7 mCi. When the gradient search algorithm is applied, the depth coordinate estimate is 998 cm (28). Knowing the source strength effectively limits the range of acceptable depths to a small window just due to solid angle effects alone. The measured transmission function contains a certain number of counts, and only a source within this range can accurately match the measured function.

4.3 RMC Response to Multiple Point Sources

Many potential orphan source search scenarios involve multiple point sources that may or may not be the same isotopes. Because the RMC maps a 1-D transmission function of a 3-D source scene, the measured transmission function will be a superposition of the transmission functions for each source. As with any imaging system, the resolution of the system is an important indicator to the capability of the system to identify two distinct sources. This section compares the results from experiments and simulations used to quantify the RMC angular resolution for a given mask configuration when the sources are the same isotope (i.e. emit the same energy photon). The single RMC dynamic range is measured as a function of source strength, which is used to make some observations about the detection limits for the system. The final topic discussed here is the performance of the system when the sources are not the same isotope. In this case a set of Ba-133, Cs-137, and Co-60 sources are measured together to determine whether position and activity estimates of the low energy Ba-133 source are adversely affected by down scattered photons from the higher energy sources. These effects are gauged by comparing the accuracy of the estimates when a single source is present versus multiple sources.

4.3.1 Angular Resolution

The RMC angular resolution can be measured or simulated by placing two point sources within the field of view and then changing their separation until they resolve into two distinct points. A series of simulations was run using the universal field model and the RMC design from Chapter 3. The mask separation is 25 cm, resulting in a theoretical angular resolution of ~55 arcminutes predicted by Eq. 2.22. Two identical point sources are simulated 1000 cm from the detector with no background. Counting statistics on the data is modeled using the Matlab command ‘poissrnd’. Initially the sources are separated by the theoretical angular resolution and an MLEM image is generated. If the sources are resolved, then they are moved closer together in 0.5 cm increments and the process is repeated until the sources are no longer resolved. If the sources are not resolved at the theoretical resolution, the sources are moved 0.5 cm apart until they are resolved. Next the sources are simulated 100 cm closer to the detector and the entire process is repeated. The theoretical angular resolution is then compared against the results from the simulated resolution as shown in Figure 4-12. The black Xs denote measured data using the prototype RMC with the source located 241, 500, and 1000 cm from the RMC. There is a slight divergence from the simulated results as the source moves further from the RMC, but the measurements are still well below the theoretical resolution. The measured values most likely measure higher because the simulation used in Fig. 4-12 assumes the background is zero.

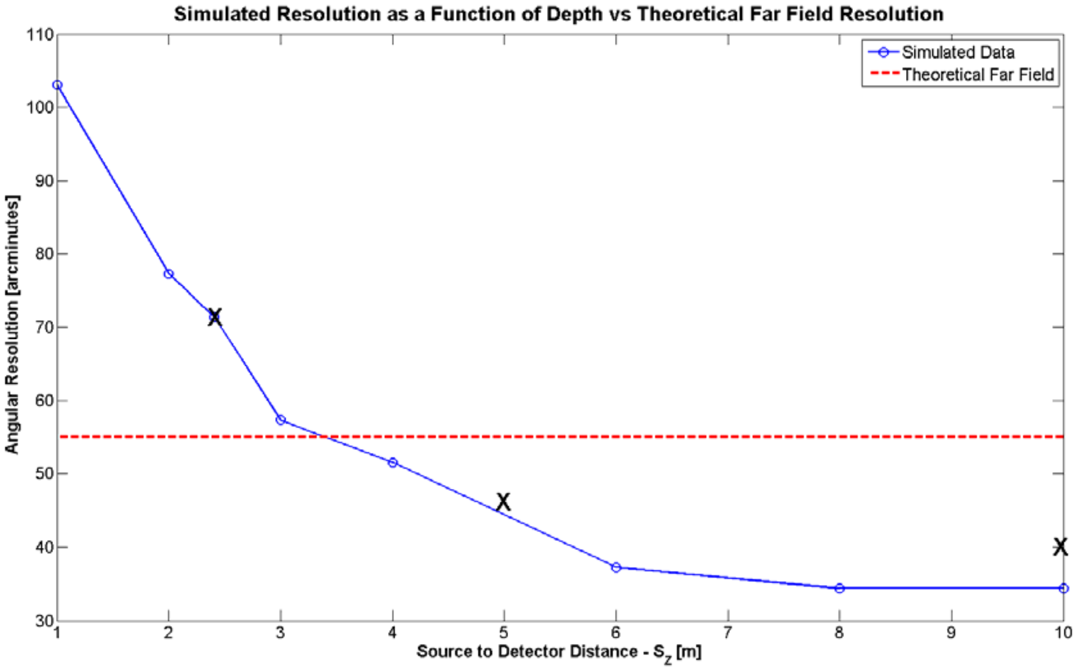

Figure 4-12. The blue curve represents the angular resolution (in arcminutes) as a function of the source depth coordinate, S_Z. These simulated data use the RMC design from Chapter 3 and assume that the unmodulated background is zero. The black Xs are measured data using the prototype RMC and the results match the simulations very well. The red line is the theoretical far field resolution given by Eq. 2.22.

The results show that a relationship exists between the angular resolution and the distance from the source to the RMC. They also show that the maximum achievable resolution is ~38% lower than the theoretical far field resolution given in Eq. 2.22. This gain in the resolution performance is directly related to the MLEM algorithm. Recall Fig. 2-14, which showed several transmission functions when two sources were separated by various distances. When the sources are very close together the transmission function still contains the characteristics of a single source. As the sources move apart two new sub-peaks begin to appear well before the sources are separated by the distance given by the theoretical angular resolution. The MLEM algorithm can account for these subtle changes in the transmission function and the resolution is improved. Figure 4-12 also shows that the resolution heads towards an asymptotic limit as the source moves toward a far field position. When the source is very close to the detector, magnification effects cause the resolution to degrade as expected.

Another important factor affecting the angular resolution is the unmodulated background, which is explored using a simulation. The same procedure for simulating the system is used as before, with the source fixed 1000 cm from the RMC. For each measurement the simulated background is increased and the sources are separated until they are resolved. Figure 4-13 shows a plot of the angular resolution as a function of the source to background ratio at the detector.

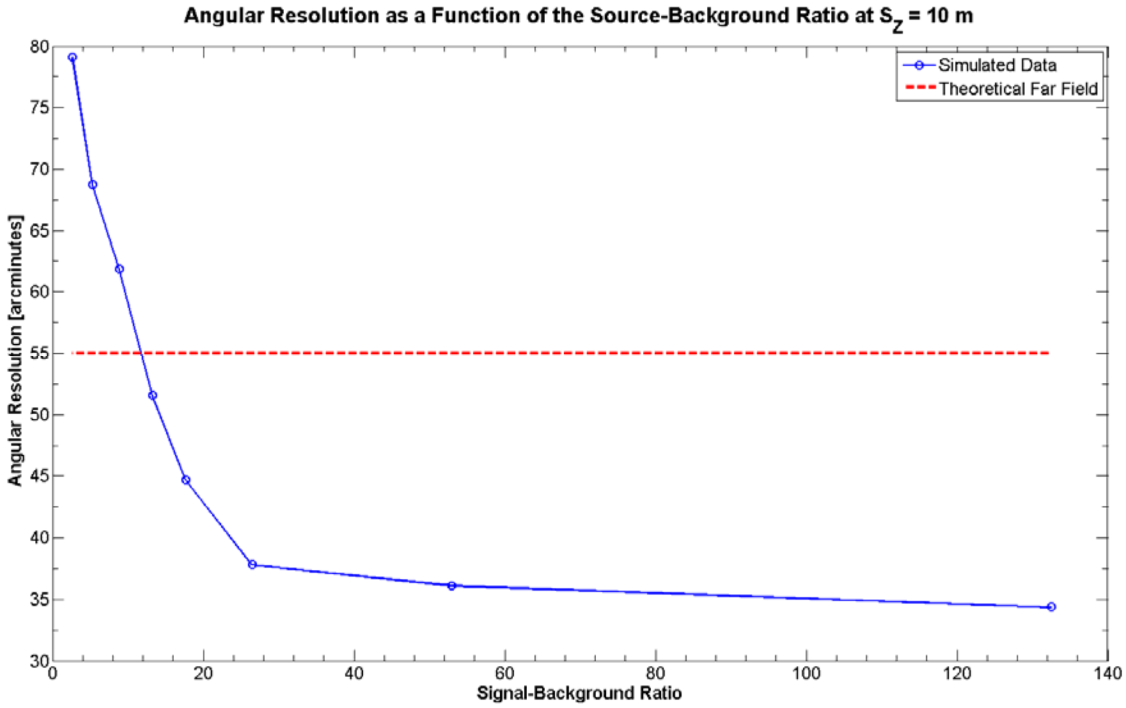

Figure 4-13. The angular resolution is shown as a function of the signal to background ratio when the source is 1027 cm from the RMC. When the source is very intense the resolution approaches the limit shown in Fig. 4.12. Even when the source to background ratio is near unity, the resolution is still less than 1.5°. The dotted red line shows the theoretical far field resolution predicted by Eq. 2.33.

In this case the source term is the count rate at the detector caused by a 2 mCi source located 1000 cm from the RMC. This methodology is used because first it is activity independent. If the 2 mCi source is replaced with a 1 mCi source, the signal to background ratio will simply be cut in half. It also allows for an approximation of the resolution when the source is located at a different distance. As an example, a source located 1414 cm from the RMC on axis, will produce approximately half as many counts in the detector as the source at 1000 cm following the $1/r^2$ law. If the signal to background ratio for the 1000 cm source is 40, then it will be 20 for the 1414 cm source. Figure 4-13 can then be referenced to get an approximate value of 43 arcminutes of resolution at 1414 cm assuming a 2 mCi source. This is approximate, because the sources are not located on axis. Caution must also be used, because the resolution degrades as the source moves closer to the detector as shown in Fig 4.12. Trying to apply this approximation to a source located at 300 cm would produce a resolution estimate that is biased low.

The results from both Figs 4-12 and 13 are encouraging for the orphan source search problem. Both figures show that the RMC maintains adequate resolution performance (<2°) even at the extremes of the distance and signal to background range. The maximum achievable resolution appears to be limited to ~34 arcminutes for the current RMC system which translates to less than 10 cm at 10 m or 1 m at 100m.

4.3.2 Dynamic Range

The dynamic range, as outlined in section 2.4.2 is a parameter defined by the ratio of the hottest source and the weakest source still detectable in an image in the field of view. This parameter is important in the orphan source search problem, because it influences the detection limit for the RMC when multiple sources are present. An experiment was conducted to measure the dynamic range of the designed RMC, and to confirm predictions from Chapter 2, that the dynamic range is limited by the statistical noise of the hot source and the modulation efficiency of the weak source.

For this experiment, a 2 mCi Ba-133 source is placed at x,y,z = (0,-15,232) cm and a six minute measurement is recorded. The source is then moved so that the separation between the first source position and the new source position is 2°. The second position in Cartesian coordinates is (7.7,-12.9,232) cm. This distance was chosen to ensure that both peaks would be fully resolved. The source is kept the same radius from the RMC axis of rotation to eliminate any perturbations that might occur from measuring different frequency components of the source scene. A second measurement is taken at this new position and the two data sets are combined in Matlab to ensure that both sources are resolved in the image. Figure 4-14 shows the relative positions of the source with respect to the RMC axis of rotation.

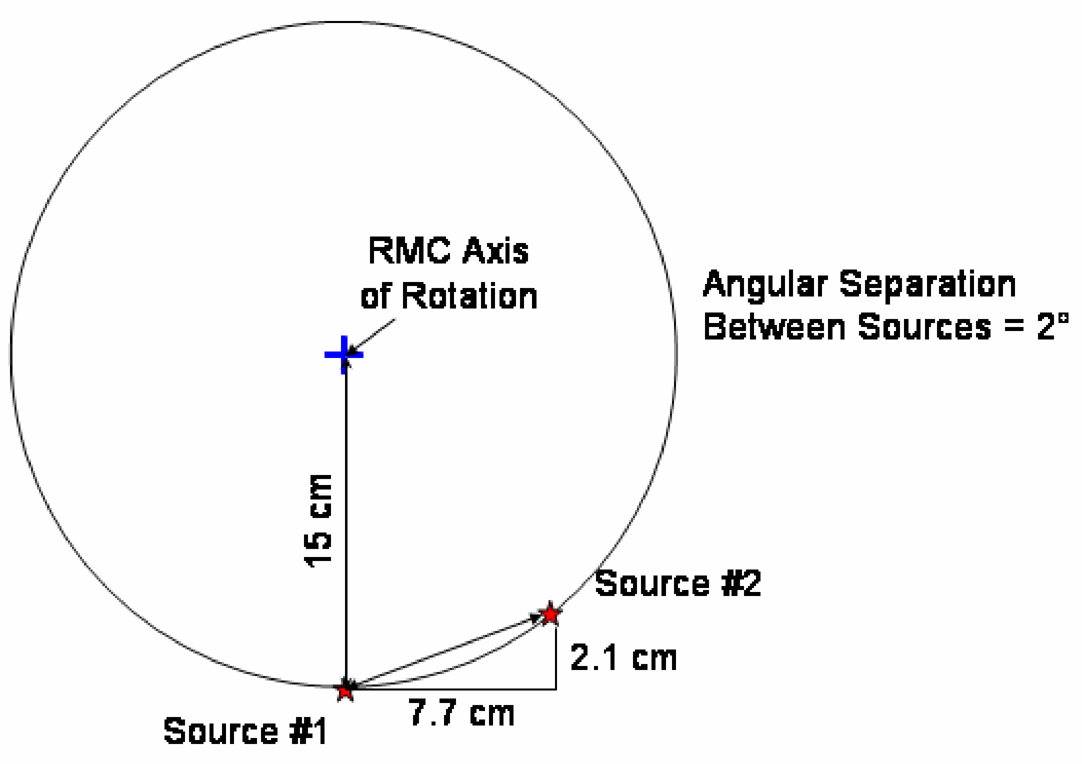

Figure 4-14. The dynamic range is measured by recording the detector response for a cold and hot source. In order to limit the effects caused by measuring data at different radii, the sources are located the same distance from the RMC axis of rotation with an angular separation between sources of ~2°.

Next, the intensity at the source 2 position is attenuated using a set of calibrated attenuator disks, which provide a known quantity of shielding. The attenuator is placed in front of the source and then another RMC measurement is recorded. The combined hot and attenuated source data are combined and an image is reconstructed. Because of the difference in strength between the two sources, the resulting images tend to have a significant amount of random noise. This noise is reduced by running 10 iterations of the bootstrap routine and taking the mean image. The signal to noise ratio is computed for both the hot and weak source and when the SNR of the weak source falls below a threshold of 5, the source is no longer detected. The dynamic range is calculated by taking the ratio of the strong source activity and the activity of the weakest source that is still detectable. Figure 4-15 shows the dynamic range as a function of the weak source SNR.

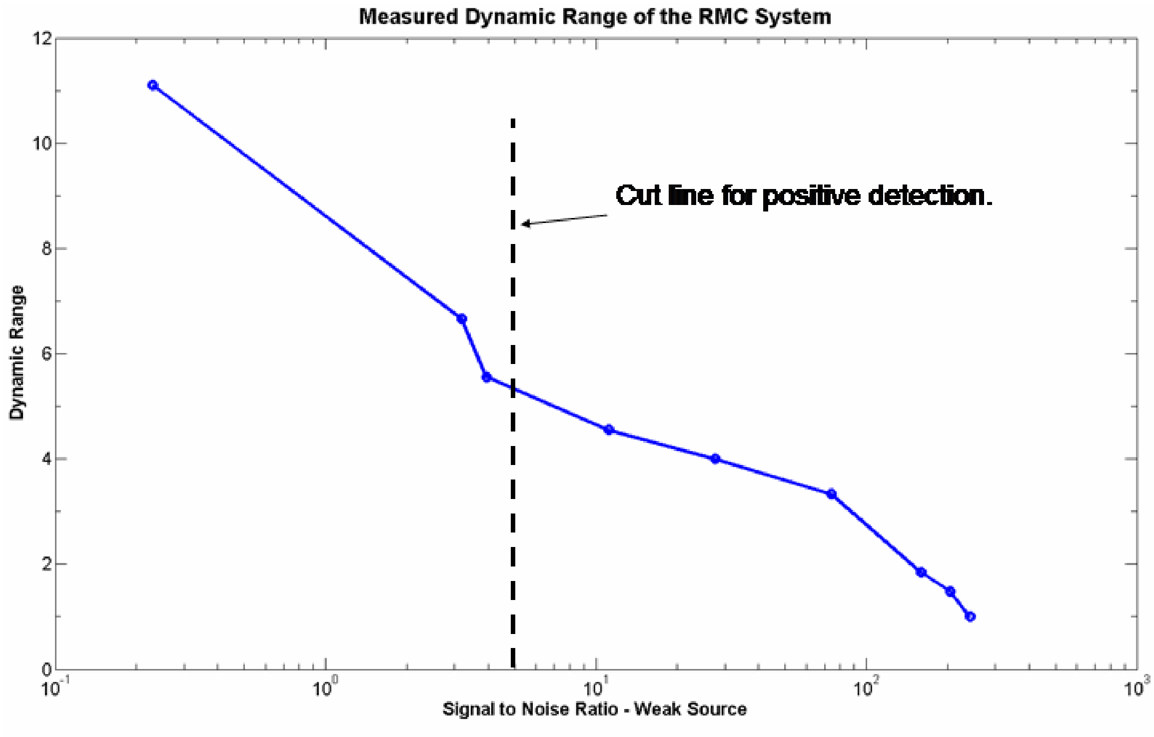

Figure 4-15. The dynamic range shown here is a measure of the RMC's ability to locate a weak source in the presence of a hot source. When the signal to noise ratio of the weak source falls below five, the weak source is no longer detectable. This condition is met when the dynamic range is ~6, which means that the RMC shown in Chapter 3 can locate a source that is six times weaker than the hottest source in the field of view.

The data in Fig. 4-15 show that the RMC design from Chapter 3 has a dynamic range of ~6, which means that the system can locate a source up to six times weaker than the hottest source in the field of view. A few comments should be made at this point on these results. First, this dynamic range represents an upper bound on the current system performance. A high unmodulated background will reduce the dynamic range because of the noise that is added to the data, making it more difficult to distinguish the weaker source. It is also seen that the position of the sources can have an impact on the dynamic range. If the weak source is closer to the axis of rotation than the strong source, it is more difficult to identify because the higher frequency modulation pattern of the hot source more effectively masks the low frequency components of the weak source.

4.3.3 Response to Multiple Sources of Different Energy

Another common scenario encountered in the orphan source search problem is one where there are multiple sources, but they consist of different isotopes emitting different energy photons. This is especially true when considering the orphan source versus a variety of nuisance sources that contribute to the lumpy background. Of primary concern with RMC measurements is that down scattered photons from high energy sources will contaminate the energy windows of potential orphan sources at lower energies. This section addresses this process and discusses the impact on the accuracy of the RMC for locating point sources.

The impact of higher energy sources can initially be quantified by measuring the count rate in a lower energy window with a high energy source present. Three sources were used to perform this study: a 100 μCi Ba-133 source, a 94.73 μCi Cs-137 source, and a103.8 μCi Co-60 source. Each source was measured independently 232 cm from the detector (the range where the RMC measurement would be made) using a 3x3” NaI detector and an ORTEC multi-channel analyzer (MCA). The total measurement time was 1 hour per spectrum. A fourth spectrum shown with the others in Figure 4-16 was taken with all three sources present. These spectra were analyzed to determine the location of the photopeaks so that a single channel analyzer can be set for subsequent counting and RMC measurements.

It is apparent from Fig 4.16 that down scattered photons from the higher energy sources contaminate the lower energy photopeaks, causing them to be broadened and less distinguished from background. The dark blue spectrum for all three sources is simply a superposition of the individual spectra for the individual sources. Table 4.1 lists the channels bounding the photopeaks for each isotope. The MCA was set to use 4096 channels and this information is used to compute the voltages used to set the SCA windows. Also shown in Table 4.4 is the total number of counts under the respective photopeaks when the source associated with the photopeak is present.

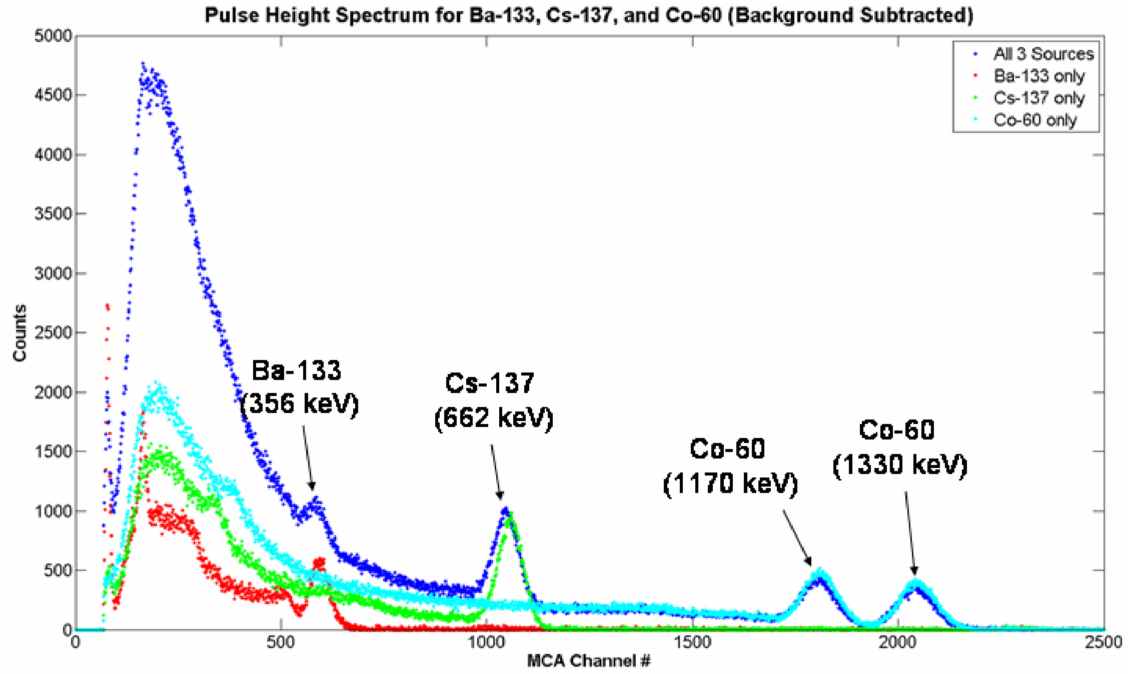

Figure 4-16. The background subtracted pulse height spectrum for three sources (Ba-133, Cs-137, and Co-60) is shown here. Down scattering from the higher energy sources leads to more noise in the Cs-137 and Ba-133 peaks. It is later shown that the accuracy of the estimates is not significantly impacted as long as this additional noise is included in the system model.

Table 4-4. The first row of this table lists the number of counts recorded under the specific photopeak shown in the columns. The second row lists the lower and upper channels that bound the photopeak in the multi-channel spectrum (using 4096 channels). The values in parentheses are the associated voltage settings that are used to set the single channel analyzer windows.

	Ba-133 Peak (356 keV)	**Cs-137 Peak (662 keV)**	**Co-60 Peak (1.17 MeV)**	**Co-60 Peak (1.33 MeV)**
Single Source Counts	68624	90526	63217	47931
Peak Window	LL* = 541 (1.32) UL – 642 (1.57)	LL = 975 (2.38) UL = 1137 (2.78)	LL = 1705 (4.16) UL = 1920 (4.69)	LL = 1952 (4.77) UL = 2142 (5.23)

LL – Lower Level Window on SCA, UL – Upper Level Window on SCA

The second part of this experiment examined the change in counts under each photopeak for a variety of source combinations. For these measurements the Velmex source table was moved to x,y,z = (0,-10,232) cm. An SCA was then set using the energy levels given in Table 4.4 for the 356 keV photopeak of Ba-133. The output of the SCA was connected to a counter that was set to record counts for 10 minutes. Four separate measurements were then made: No sources (background only), only the Cs-137 source present, only the Co-60 source present, and both the Cs-137 and Co-60 sources present. This experiment was then repeated using the other energy windows for Cs-137 and Co-60. Table 4.5 shows the results from these measurements.

Table 4-5. This data shows the number of counts under a specified photopeak when various combinations of sources other than the photopeak source are present. As with Fig. 4.16 this data shows that the lower energy peaks are corrupted by down scattered photons, while the high energy peaks are unperturbed as expected.

	Total Counts Under the Photopeak for a Given Source Combination						
Peak Window	**No Sources**	**Ba133**	**Cs137**	**Co-60**	**Ba+Cs**	**Ba+Co**	**Cs+Co**
Ba-133	4201	---	8316	10156	---	---	14522
Cs-137	2532	2424	---	8044	---	7936	---
Co-60 (1.17 MeV)	1330	1297	1266	---	1192	---	---
Co-60 (1.33 MeV)	1012	966	982	---	958	---	---

The second column of Table 4.5 shows the counts recorded in each energy window when there are no sources and reflects the room background. As expected, the number of background counts in the higher energy windows does not change when a lower energy source is present. The counts in the Ba-133 window increase by ~2.5 times when the Co-60 and Cs-137 sources are placed in front of the system. The last experiment measures the transmission function to determine whether these counts are modulated, or simply an additive component to the unmodulated background.

The final set of measurements taken in this experiment was used to determine whether the down scattered photons are modulated as they pass through the RMC masks. The results indicate that the down scattered photons from high energy sources are not modulated in the lower energy windows as they passed through the mask system. This means that the effect of high energy sources on lower energy RMC transmission functions is a constant increase across the entire transmission function. For this experiment, the SCA window is again set for Ba-133 and a series of 30 minute RMC measurements are made with various combinations of the Ba-133, Cs-137, and Co-60 sources placed at (0,-10,232) cm.

Figure 4-15 shows the RMC transmission functions and associated images when the SCA window is set to the 356 keV photopeak. The first image is with just the Ba-133 source in place. The second image uses the Ba-133 and the Cs-137 source, and the final image is all three sources in place. Figure 4.15 demonstrates that strong estimates of the position and source intensity can be found provided that the background contribution from the higher energy sources is properly modeled with the MLEM algorithm. For each of the images shown, the bootstrap method (100 iterations) is applied to find the standard deviation and bias of the peak position and source activity estimate. These results are presented in Table 4.6.

Table 4-6. Shown below are the polor coordinate and activity estimates when the SCA window is set for the 356 keV photopeak. The true source position is x,y = (10,0) cm and the true activity is 100 μCi. The estimates shown are mean estimates generated from 100 iterations of the bootstrap algorithm.

	X Estimate [cm]	**Std. Dev. X [cm]**	**Y Estimate [cm]**	**Std. Dev. Y [cm]**	**Activity Estimate [μCi]**	**Activity Std. Dev. [μCi]**
Ba only	10.5	0.158	0.7	0.258	135	39.5
Ba+Cs	10.6	0.211	0.2	0.350	108	23.1
Ba+Co+Cs	11.0	0.158	0.7	0.258	114	45.5

The data shown in Figure 4.15 and Table 4.6 is encouraging, because it demonstrates that the RMC correctly identifies the Ba-133 source in the presence of both the Cs-137 and Co-60 sources, with little degradation to the accuracy of the estimate. The key to generating a good estimate is making sure that the background contribution from the higher energy sources at 356 keV is accounted for during image reconstruction. Practically, this means that if available, the entire energy spectrum should be analyzed prior to image reconstruction so that the contributions from down scattering can be quantified and modeled.

The primary impact from the down scattered photons will be a reduction in the dynamic range and resolution of the system for lower energy sources. This reduction occurs because the statistical noise introduced by the higher background will act to mask less intense sources as described in section 4.3.2. The decrease in resolution can be seen by referencing Fig. 4-13, which shows the resolution is degraded as the background increases.

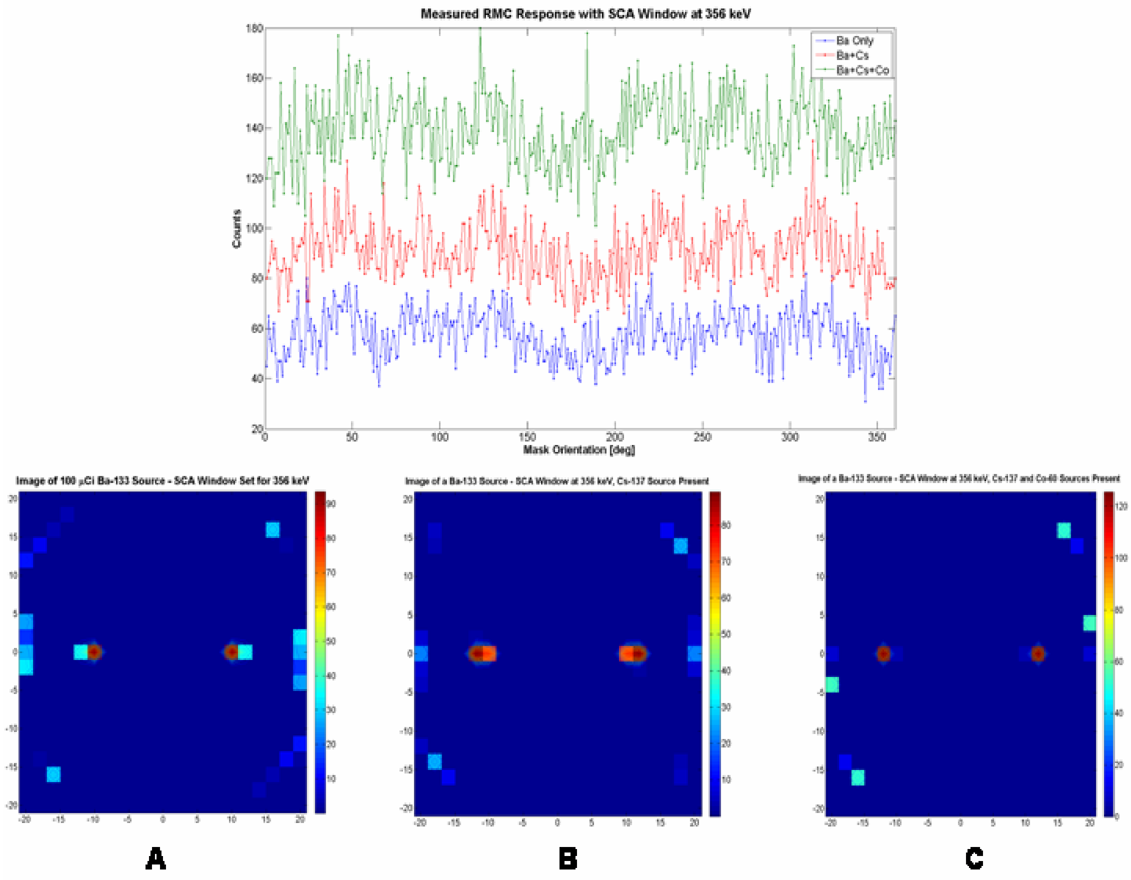

Figure 4-17. The effects of higher energy sources on the transmission function at lower energies is highlighted in the top window of this figure. The down scattered photons are not modulated in time, but instead contribute a uniform background in the energy window of interest (356 keV for this figure). When this background is correctly accounted for using the MLEM algorithm, a strong image is formed. Panel A is the image of only the Ba-133. Panel B is the image with the Ba-133 and Cs-137 sources present. Panel C is the image formed using the Ba-133, Cs-137, and Co-60 sources.

4.4 Detection Time

The final section of chapter 4 presents a method for estimating the time required to positively identify a point source given information about the source location, emission energy, and activity. Using the log-likelihood distribution methods described in section 2.4, a simulated RMC system viewing a source scene is compared against a RMC system viewing a background scene. It is shown that the separation between the source plus background and background only distributions can be used to determine the minimum amount of scanning time that is required to detect a source of a known activity. This information is useful for understanding the detection limits of the RMC.

The next set of experiments is used to compare the predicted detection time from simulations to measured data. The first step in the process is to generate the source plus background and background only log-likelihood distributions, which are used to locate the point of separation. Both distributions are computed using the universal field model of the RMC system as it would be configured for a measurement. For this study the 1.27 cm thick masks are used with a separation parameter of 24 cm. The simulated source has an activity of 25 μCi and is positioned at (0,-15,232) cm. The unmodulated background is 10 counts per second. Three simulations are executed where the total sampling times are 144, 216, and 360 seconds. Figure 4-18 shows the separation between the distributions for the three selected sampling times.

For this particular study, the regions of interest in Fig. 4-18 are where the distributions overlap. In particular, it is important to know the fraction of true positive events, which is the part of the source plus background distribution that does not overlap the background only distribution. The true positive fraction was calculated for each of the distributions shown in Fig. 4-18 and they are listed in Table 4.7. These numbers are validated using experimental data.

The experimental setup is the same as the simulation. A 25 mCi Na-22 source is used, and the SCA window is set to capture the 511 keV annihilation photopeak. Twenty independent measurements are taken at each of the sampling times used in Fig. 4.16. The MLEM algorithm is used to reconstruct images using the data and the resulting image is scored as either positive or negative. A positive reconstructed image properly locates the source with a signal to noise ratio greater than 5. A negative image does not have the source in the correct position or it has a SNR that is too low. The true positive ratio is the number of positive images generated divided by the total number of measurements. These results are also shown in Table 4.7.

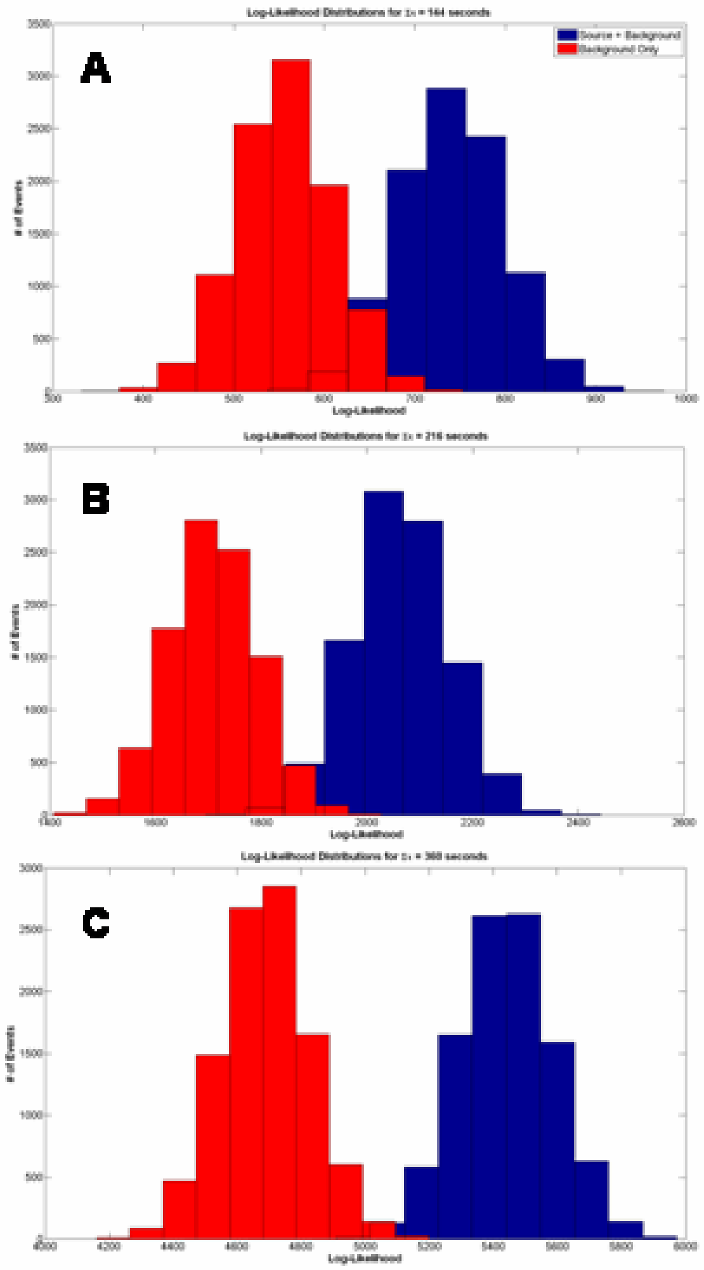

Figure 4-18. The three histograms above show the log-likelihood distributions for different total measurement times (A-144 sec, B – 216 sec, C – 360 sec). The red distribution is the log-likelihood distribution when only background is present and the blue distribution is the source plus background distribution. As the total measurement time increases, the distributions separate and the probability that the measured data will produce an image that accurately locates the source increases.

The data in Table 4.7 strongly support that the log-likelihood distributions can be used to predict the sampling time required in order to ensure a positive detection with a known confidence. This information can now be used by the user in the following manner. A given search scenario requires that the measurement must be completed in 30 minutes. Given this and the RMC design information, it is possible to determine the minimum detectable source at a known distance with 99% confidence that an image will be generated. In this case the detection time is fixed and a guess at the minimum activity is made at a known range. The distributions are created and the activity is increased if the true positive rate is lower than 99% or decreased if the true positive rate is greater than 99%. This iterative procedure is completed until the guess for the activity produces a pair of distributions with a true positive rate close to 99%. When this is applied to the current problem, the minimum detectable source at 356 keV is 12 μCi at 241 cm in 30 minutes. A crude estimate can be made for the minimum detectable source at other distances by invoking the inverse square law and scaling the activity appropriately. Figure 4-19 shows a plot of the detection limits as a function of depth for this current problem.

Table 4-7. This table compares the simulated true positive ratio found by comparing the log-likelihood distributions against the measured true positive ratio. Excellent agreement between the two methods indicates that the log-likelihood distributions can be used before a measurement to determine a detection limit based on the total sampling time allotted.

Sampling Time [sec]	Simulated True Positive Ratio	# Positive Images	# Negative Images	Measured True Positive Ratio
144	0.42	9	11	0.45
216	0.65	13	7	0.65
360	0.95	18	2	0.90

This scenario highlights one of many benefits to using the maximum likelihood methodology for RMC measurements. Interestingly, a 1 mCi source should be detectable to 99% confidence in 30 minutes at a range of 20 meters using the current non-optimized RMC system, and it would require a 20 mCi source to get a positive detection at 100 m. It should be noted that this simple scenario does not include the possibility of other sources in the field of view or the potential for background shifts during the course of the measurement. Also the assumption of the inverse square law at these distances is not accurate due to attenuation of gamma rays in the atmosphere. All of these factors can be incorporated into the likelihood model however, making the use of the log-likelihood distributions practical even with the more difficult scenarios.

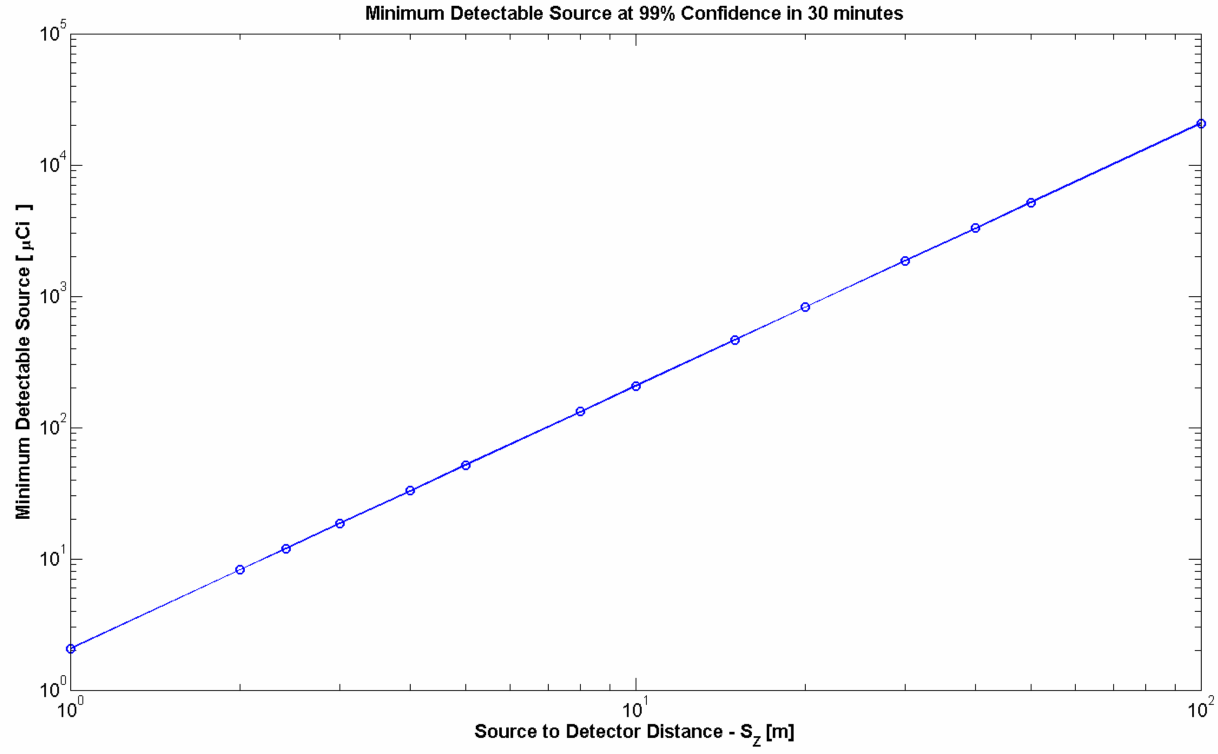

Figure 4-19. This shows the minimum detectable source at various distances from the detector using the RMC with a allotted scan time of 30 minutes. The detection values are to 99% confidence that the RMC measurement will produce an image showing the position of the source.

4.5 Summary of RMC Measurements and Simulations

The results of several measurements and simulations are used to study the performance of a single RMC system for locating point sources. The unmodulated background must be modeled correctly, as under- or overestimation can lead to an increase in the image noise and a decrease in the SNR when a source is located in the field of view.

Next several measurements demonstrated the ability of the system to accurately locate a single point source within ~1.6 arcminutes of accuracy. Also presented was the concept of three RMC imaging zones. The first zone is the blind spot running from the center of the RMC out to a position that is approximately equivalent to the system angular resolution. Sources located in this zone can not be accurately resolved, and typically can not be imaged. Beyond this zone is the imaging zone, which extends from the blind spot edge out to the edge of the field of view given by Eq. 2.21. Sources located in this zone produce unique transmission functions and localization of the source polar coordinates is very accurate. The final zone is the single mask imaging zone, which is located from the edge of the two mask field of view out to the edge of the single mask field of view given by Eq. 4.1. Although sources located in this region can not be accurately located, the images produced by running a few iterations of the MLEM algorithm show a region that points toward the azimuthal direction of the source. This information could possibly be used to rotate the RMC so that the source is in the imaging zone.

The next set of simulations and experiments focused on methods for estimating the depth coordinate of the source. The MLEM algorithm proved to be too underdetermined to adequately locate a source in three dimensions. It was useful however for locating the two polar coordinates ρ and ϕ, which are then used as constraints for a gradient search algorithm to perform a search using the log-likelihood formula. This method was able to identify the depth coordinate and source activity within 10% of the true values when the source was located within 400 cm of the RMC. Between 400 and 800 cm the estimates were not as accurate, but still within the standard deviation of the 10 independent runs of the gradient search routine. Beyond 800 cm the estimates were very inaccurate, and the estimates were always biased low. The estimates at these ranges do provide a lower bound on the depth however, which is useful for separating near-mid range (1-8 meters) and far-mid range (10-50 meters) sources. Finally, it was shown that when the two polar coordinates and the activity of the source are known, the depth coordinate can be located with a much higher degree of accuracy (1% at 10 meters).

Section 4.3 considers the RMC performance when multiple point sources are located in the system field of view. The angular resolution is both simulated and measured at several distances from the RMC. The results indicate that using the MLEM algorithm produces an angular resolution that is ~38% better than the theoretical value published previously. Additionally, the resolution is dependent on the distance from the source to the RMC. When the source is close to the detector the resolution is worse than the theoretical value due to magnification effects. As the source moves beyond 7 meters the resolution converges to its maximum value of ~35 arcminutes. The angular resolution is also affected by the unmodulated background. When the source to background ratio is high the resolution converges towards a maximum value of 35 arcminutes. When the source to background ratio is small, the resolution decreases due to added statistical noise on the data that makes the features (peaks and valleys) of the measured transmission function less distinct. The results of the angular resolution study are positive with regards to the orphan source search. The regime of operation for this problem ensures that the resolution will typically be better than 2° for most applications.

The dynamic range was another RMC performance indicator that was measured. The results show that the current RMC has a dynamic range of ~6, which means that the system can successfully detect the presence of a source emitting the same energy photons that is six times weaker than the hottest source in the field of view. Additionally measurements confirm that the dynamic range is primarily influence by the statistical noise on the hot source and the modulation efficiency of the weak source.

RMC measurement results were also presented when multiple sources of different isotopes are imaged. It is shown that the higher energy sources contribute to a uniform background in the photopeaks of lower energy sources. This background reduces the dynamic range and resolution of the system, but was shown to have little impact on the accuracy of the RMC results. Images of a Ba-133 source were generated with just the Ba-133 source present and then with Cs-137 and Co-60 sources present as well. The accuracy and standard deviation for all of the various source combinations were within 1% of each other, provided that the background provided by the higher energy sources was correctly modeled in the MLEM algorithm.

The final section of Chapter 4 presented a method for predicting the time required to detect and locate an orphan source by comparing simulated log-likelihood distributions of the source plus background and background only conditions. Measurements confirm that the overlap in the distributions directly correlates to the true positive image rate. By increasing the total time allocated for a measurement the separation between the distributions increases and the confidence for detecting a given source to a known confidence level can be calculated.

These results demonstrate that a single RMC is quite flexible for locating point source distributions. The tools and results developed here and in the chapters 2 and 3 can be used to make some general conclusions about the effectiveness of an RMC system for location orphan sources. Chapter 5 presents these conclusions and then looks ahead to some future work that can be done with this system.

CHAPTER V

CONCLUSIONS AND FUTURE WORK

The final chapter of this dissertation reviews the key findings of the research and then makes some conclusions regarding the suitability of an RMC system for the orphan source search problem. The chapter closes with an outline of four future research projects that would be beneficial for imaging with the RMC.

5.1 Review of Key Findings

Although RMC systems have been in use for over five decades, this research highlighted some new areas of study that were not previously considered. A new universal field system model was developed to address the problem of imaging sources in the near field. Not only does the model address the issue of near field versus far field measurements, but also includes many physical design parameters such as the mask thickness, mask penetrations by high energy photons, and the effects of finite extent mask patterns. The model is more flexible and well suited to design and optimization studies than many existing far field models, because most of the mask and system design elements are directly incorporated into the algorithm. For example a user could define a three mask system where all three masks are made of different materials with different grid patterns. Because the universal field model predicts the RMC transmission function accurately, the quality of the MLEM estimates in terms of position accuracy and resolution is enhanced over a far field model which makes several assumptions about the physical system (i.e., black thin masks, infinite extent, etc.).

Section 3.2 considered different operating parameters that could be modified during a measurement to add capabilities to RMC imaging. The separation between masks controls the system angular resolution as well as the field of view. When a single RMC measurement is used to measure an extended source, the reconstructed image is typically biased towards a particular point in the image. By changing the distance between the masks during a measurement, multiple Fourier components of the source scene are measured. These additional measurements add more information to the system, which allows extended sources to be imaged correctly. Once an extended source is located in a source scene, it can be removed during the image reconstruction step by incorporating it into the unmodulated background. This procedure was applied to a hot extended source that was masking a weaker point source. When this technique was applied, the extended source disappeared from the image and the weaker source appears. There is some error associated with this technique however, as the reconstructed position of the weak source has a bias of ~4 cm when the source to detector distance is 2.5 meters. The bias most likely is introduced by statistical noise caused by the hotter extended source.

An adaptive sampling method was applied to RMC operations, but was found to be unusable at this time due to an inability to reject false positives that occur in the images with sparse data. This method focused on changing the dwell time parameter so that the RMC spent more of its time sampling in regions where the source was most likely to be located. A scout scan is performed and the image reconstruction is used to locate any peaks. Based on these peak locations the dwell time is modified for subsequent scans to detect the source earlier. As mentioned above, when the data is sparse, false positives can occur, which force the system to spend time search in the wrong region. This makes the problem worse, as the region containing the source may now be under sampled by excessive sampling in the wrong area. In this case the simple 1D transmission function is not robust enough to account for an incorrect sampling decision.

The final body of work looked at several measurements made with the RMC. Images of a uniform background can be inaccurate, noisy, or filled with false positives if the assumed background supplied to the MLEM algorithm is either over- or underestimated. It was also shown that there are three zones of interest in the field of view when using an RMC system. The first zone contains a blind spot that extends from the RMC axis of rotation out to a distance equal to the angular resolution. Sources located in this region can not be located using a single RMC measurement. A second RMC or measurement with a different axis of rotation orientation must be used to eliminate this blind spot. The second region is the imaging region which extends from the edge of the blind spot to the edge of the system field of view. Reconstructed position estimates in this region were very precise, with the average radial and azimuthal coordinates having an error of 0.25 and 10 arc minutes respectively. The average standard deviation on the radial and azimuthal position estimates was 1.12 and 146 arc minutes respectively. The final zone is the single mask zone which extends from the edge of the system field of view to the edge of the single mask field of view. Sources in this region can not be located, but running a few iterations of the MLEM algorithm (<50) highlights a broad region that points toward the source. This information can be used to reposition the RMC centerline for additional measurements.

Results also demonstrated that an approximate estimate of the depth coordinate can be obtained using a combination of the MLEM algorithm and a gradient search algorithm. In this case the MLEM algorithm is used to accurately identify the two polar coordinates of the source, ρ and ϕ. A gradient search algorithm as outlined in section 2.3.2 is then used with the RMC universal model (Eq. 2.1) to produces estimates for the source activity and depth coordinate, S_Z. The average error on the depth coordinate for sources less than 6 meters from the detector was less than 1 meter. By the time the source is at 10 meters the error is greater than 3 meters. Although poor, the estimates for the long range sources (>6 meters) can be used to provide a lower range threshold to the gradient search algorithm. When the routine is executed again with the threshold, the position error for sources at 8 and 10 meters was reduced to ~1 meter. It was also shown that if the source activity is a known quantity then the gradient search algorithm can locate a source at 10 meters with an average error of 30 cm.

Next, the RMC response was simulated and measured when two identical point sources are in the field of view. The angular resolution was measured, and found to be ~38% better than previous theoretical results predicted when the source is greater than 8 meters from the system. This reduction is attributed to the maximum likelihood approach to image reconstruction. It is clear when looking at the transmission functions as two sources move apart that the combined transmission function becomes unique well before the theoretical predictions. When the source is closer than 3 meters, the resolution becomes worse than predicted by theory. This is attributed to the magnification of the projected front mask, which decreases the RMC position sensitivity. The resolution is also affected by an increase in the unmodulated background. As the background increases (or the source strength decreases) the angular resolution becomes worse. This can also be understood by referencing the transmission functions. When the background is high, the transmission functions become more noisy, which makes it difficult for the algorithm to pick up the subtle change in the transmission function as the two sources move apart.

Another scenario considers the effects of two point sources in the field of view, when each emits different energy photons. It was shown that down scattered photons are not modulated by the masks, but instead act as an additive component to the uniform unmodulated background. These results emphasize the need for a spectroscopic RMC imaging system, so that the down scattered background can be quantified and accounted for when reconstructing images at lower energies. When properly accounted for, it was shown that images of sources at lower energies (in the presence of a high energy source) were reconstructed properly with no loss of accuracy in the position estimate.

The final section of this thesis studied the time it takes to detect and locate a source using the RMC. Log-likelihood distributions of source plus background and background only distributions were used to predict the amount of scan time that would be required to locate a known source to a given level of confidence. These predictions were tested against measured data which matched within 95% of one another. This is a useful tool for field user, who can use the simulations to predict the length of time required to declare an area free of orphan sources to a desired confidence.

These results are encouraging, because they demonstrate that the RMC is a suitable candidate for the orphan source search problem. The next section discusses the advantages and disadvantages of the RMC for the orphan source search problem, and then considers how future research can enhance the current capabilities.

5.2 Suitability of the RMC to the Orphan Source Search Problem

Given the performance of the RMC during this research, there are a few observations that can be made regarding the suitability of this system to locate orphan sources. There are several positive attributes of RMC imaging for the orphan source search problem.

The high degree of precision for locating sources (~0.25 arc minutes radial and ~10 arc minutes azimuthally on average) as well as the excellent angular resolution (~35 arc minutes beyond 8 meters) using relatively coarse masks highlight the strengths of the technique. The depth coordinate estimates, although coarse, are still useful for narrowing a potential search area. With some a priori information such as the source activity, the error in the depth coordinate can be reduced by an order of magnitude. The ability to image and discriminate nuisance sources using the system model is very useful and builds on the success of earlier systems using multiple RMCs with different mask patterns. Finally the development of a method for predicting the detection limit of the RMC is critical for work in this field as it allows the user to know the amount of time a region must be scanned before it can be declared source free to a known confidence.

The negative aspects of the RMC for this task begin with the system field of view. The prototype system has a maximum field of view of ~17° using 1.27 cm masks with 4 mm slits. This can be increased to ~35° by reducing the mask thickness by half. As the masks become thinner, more photons are able to penetrate the masks and the modulation efficiency decreases, degrading both the dynamic range and resolution of the RMC. The slits in the masks can be made wider at the expense of the angular resolution. Another negative aspect of the RMC is that sparse data sets can sometimes produce peaks in images that are not physically tied to a particular source. This scenario would be true of any orphan source search where the source is shielded, has a low activity, or is in a region of high background. This can usually be remedied by running the bootstrap algorithm multiple times and taking the mean of the ensemble. Because the spurious peaks change from image to image, many realizations of a background source scene will average to a flat background when no source is present as shown in section 4.1. Finally, the geometric efficiency for a typical RMC system (25%) is relatively low compared to other imaging modalities such as coded aperture (50%) or Compton imaging (close to 100%). Although opening the slits represents a possible solution, the imaging performance is decreased in terms of the angular resolution. The tradeoff in this case is fast detection times versus high resolution images. Some of this will be defined by the nature of the task. If the orphan source is in the 100 meter range, then high resolution will be more important than at close range because the search area scales with the distance to the source. A high resolution narrows the search window. If the application is a port of entry, where the scan times are restricted to a few minutes the RMC may be a poor choice unless the geometric efficiency can be increased. This all depends on required detection limits. It may be that a 3-minute scan with an RMC is considered sufficient based on the target sources to declare an area orphan source free. If this is the case, then the RMC might be an excellent option because of its simple design. Again it all comes back to designing the system for the detection task that is required and selecting the correct system to achieve the task benchmarks.

Although the negative items reflect that some research is still needed, none of the problems appear to be impossible to overcome with additional research. There are several methods for improving the field of view, from going to higher Z materials (allowing thinner masks), to building an array of RMCs with overlapping fields of view to image a wide area. Killing or rejecting spurious pulses may be possible with further image processing techniques that can help clean up the image and reject false positives. The geometric efficiency can be improved by opening the masks, or by considering novel mask patterns that provide high resolution with fewer photons. The final portion of this thesis will look at several research initiatives that could be conducted to make RMC imaging better for the general orphan source search problem.

5.3 Future Work

5.3.1 System Design Enhancements and Optimization

There are several design enhancements that can and should be made to the current RMC system. First among these is the development of a better data acquisition system. Not only is the current design limited to measurements of a single photopeak, but it is also unnecessarily bulky. For a relatively modest investment (<$2000) a more compact data acquisition system can be built that handles both the position decoding operation and pulse height measurements. This design would contain a trigger input with a variable threshold and a peak-hold circuit with a 14-bit ADC to detect an incoming detector pulse and then digitize and measure the pulse height. Also included would be an updated, faster quadrature decoder IC to provide the angular orientation of the masks. The system would be controlled using a small field programmable gate array (FPGA) or microcontroller and communicate with the data acquisition computer via a USB interface [Ber08]. Whenever a pulse is triggered, the decoding circuit would be queried and the pulse height and instantaneous mask orientation would be recorded. The output data would be a list of individual pulse height measurements stamped with the orientation of the masks and time when the pulse occurred. A system like this could eliminate the need for bulky NIM modules and could fit inside a package that is about half the size of a small laptop. The entire system would consist of the RMC device and detector, the motor driver (the size of a small book), the new data acquisition box, a power supply, and a laptop. This could all be mounted on a small cart for portability and measurements outside of the lab.

Another design enhancement would be the addition of a small linear slide to the front mask carrier. Section 3.2 demonstrated the effectiveness of making multiple measurements with different mask separation values. The motorized slide would be computer controlled, and capable of changing the mask position during an RMC measurement. This would make a study on adaptively changing the mask separation much easier.

Studies also need to look at methods for increasing the field of view. Consider Figure 5-1, and note the increase in the field of view by simply making the front mask have a larger diameter. Although simple in concept, there is a tradeoff between increasing the field of view and the mask thickness. Section 3.1.2 discussed the effect of mask thickness on the field of view and demonstrated that the system field of view is limited to the minimum of either the single mask field of view given by Eq. 3.1 or the system field of view given by Eq. 2.21. For example, it is not difficult to construct a system that has a ~120° field of view by increasing the diameter of the front mask from 7.6 cm to 25 cm with a mask spacing of 15 cm. To create a single mask that has this field of view however would require either a thin mask or large slits. Assuming the masks are 1.27 cm thick, the slits would have to be 4.4 cm wide to have a 120° field of view. Such a mask would only have 3 slits if the mask diameter is fixed at 25 cm. If the slits are constrained to be 4 mm wide with a mask diameter of 25 cm, then the mask would have to be 3.5 mm thick. Referencing Fig. 3-2, it is seen that the modulation efficiency for a 3.5 mm mask might be acceptable for lower energy photons (such as the 356 keV line of Ba-133), but is less than 20% for photons above 1 MeV. A parameter optimization study could clarify the tradeoffs between the single mask and system fields of view.

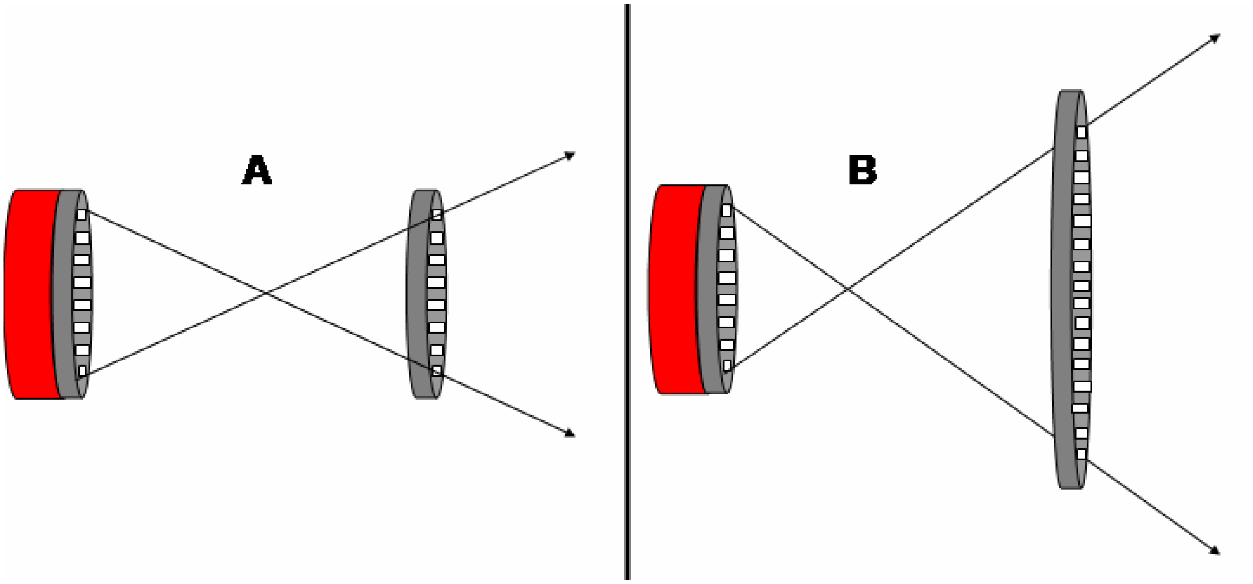

Figure 5-1. Increasing the size of the front mask (B) increases the system field of view. Increasing the mask size is limited however, because of the finite field of view caused by the thickness of a single mask.

Finally there is a large degree of design optimization that still needs to take place with regards to the orphan source search. The universal field model combined with tools such as the Cramer Rao Lower Bound on the variance and gradient search algorithms such as ‘fmincon’ would be very helpful with this endeavor. An optimization of the mask pitch for example might involve providing the universal field algorithm with several test source scenes. A search algorithm could then be developed to test various mask configurations until one is found that produces estimates with the lowest variance. At the very least, these types of studies could be useful for eliminating certain classes of mask designs (really narrow slit and large slats for example) from consideration.

5.3.2 Imaging with RMC arrays

Several groups including the RHESSI satellite team and Sharma have generated useful images with an array of RMCs [Huf02,Sha07-II]. Adding additional RMCs provide different viewpoints of a given source scene. This additional information is useful in several contexts. First, it was shown in the earliest days of RMC imaging that the 180°

ambiguity that is introduced by symmetric masks could be resolved by making two measurements with different RMC orientations [Mer67,Sch67,Wil70]. This occurs because the two systems have a different viewpoint of the source and when those two data sets are combined there is no ambiguity. Multiple RMCs have also been used to measure the distance to a source using parallax. Because the field of view may be a limiting factor for the orphan source search, a fan beam array may be a reasonable solution. The fan beam array shown in Fig. 5-2 would use multiple RMCs to provide an extended field of view. The entire array could also be placed on a rotary actuator, which would allow the RMC centerlines to be rotated back and forth as a way to enhance the image quality.

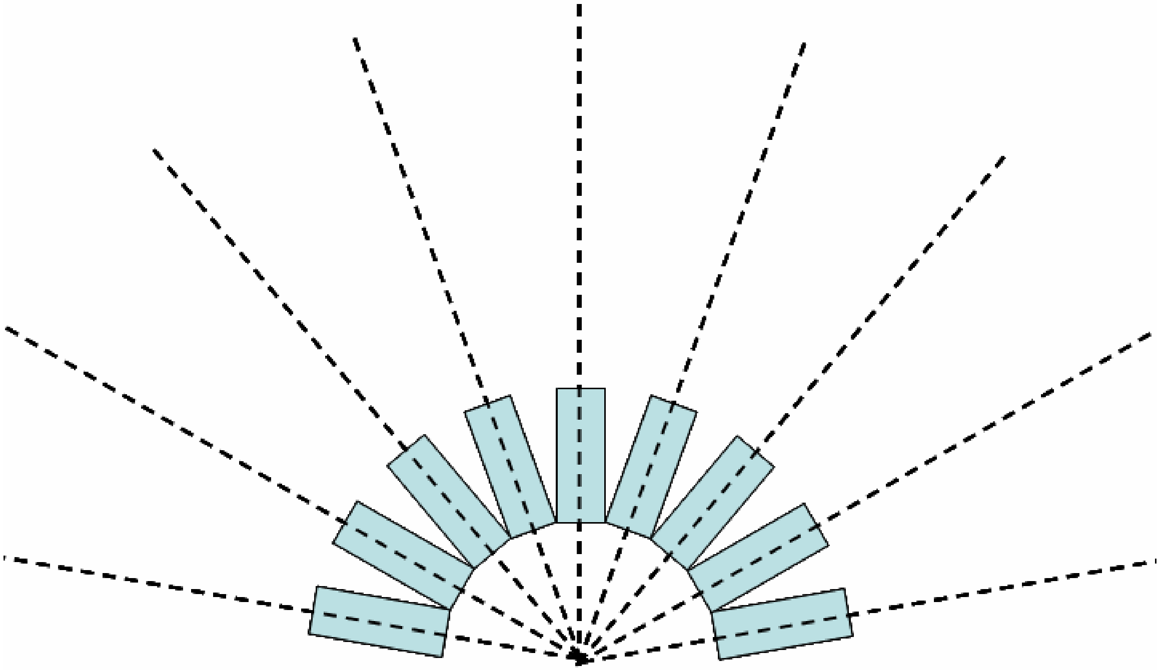

Figure 5-2. A fan beam array of RMCs is a possible configuration that could be used to extend the RMC field of view. The blue tubes represent the RMCs with the black dotted line denoting the axis of rotation. Potential blind spots in the array could be alleviated by placing the entire assembly on a rotary table and rotating the system halfway through a measurement to ensure full coverage.

Closely related to RMC arrays would be a single RMC mounted on a rotary turret or a linear positioning device. For a given allocated sampling time, the RMC axis of rotation could be moved using these devices, producing a different view of the source scene.

These individual measurements can then be combined using the MLEM algorithm to produce an estimate for a wider field of view.

5.3.3 Further Adaptive Imaging Studies

The short adaptive imaging study performed in this research only addressed modifying the dwell time parameter. It was also shown that changing the mask separation parameter is a powerful tool for measuring extended sources. The optimal selection of mask separations was not considered at this time. It is reasonable to assume that for a given source scene there is an optimal way to operate the RMC with regards to moving the masks. This can not be known prior to the measurement because each source scene will be unique. An adaptive scheme might make a few scout measurements and then use this data to choose an optimal set of mask separations. This is similar to methods that have been applied to adaptive pinhole imaging, where the separation between the pinhole and detector can be adaptively modified producing a well focused image [Bar07].

5.3.4 Time Coded Apertures

The decision to study RMCs for this thesis initially came out of a search to develop a portable time coded aperture imaging system. Time coded apertures are similar to static coded apertures, except the mask pattern is recorded as a function of time. In many ways the RMC is a simple form of a time coded aperture. Early work on these systems by May et al. and later by Clinthorne et al. demonstrated that time coded apertures can provide much higher quality images than static coded apertures in high background environments (low signal to noise regions) [May74,Cli95]. One design used a large tungsten coded plate that was placed over a pinhole array that covered a position sensitive detector [Cli95]. This design is highlighted in Figure 5-3. During a measurement the tungsten plate would be move to a position and a coded image would be measured by the position sensitive detector. The plate would then be moved one increment to the left so that a new coded pattern was in place and a second measurement was made. The process was repeated until the plate had slid through all the different possible combinations of a pseudorandom sequence.

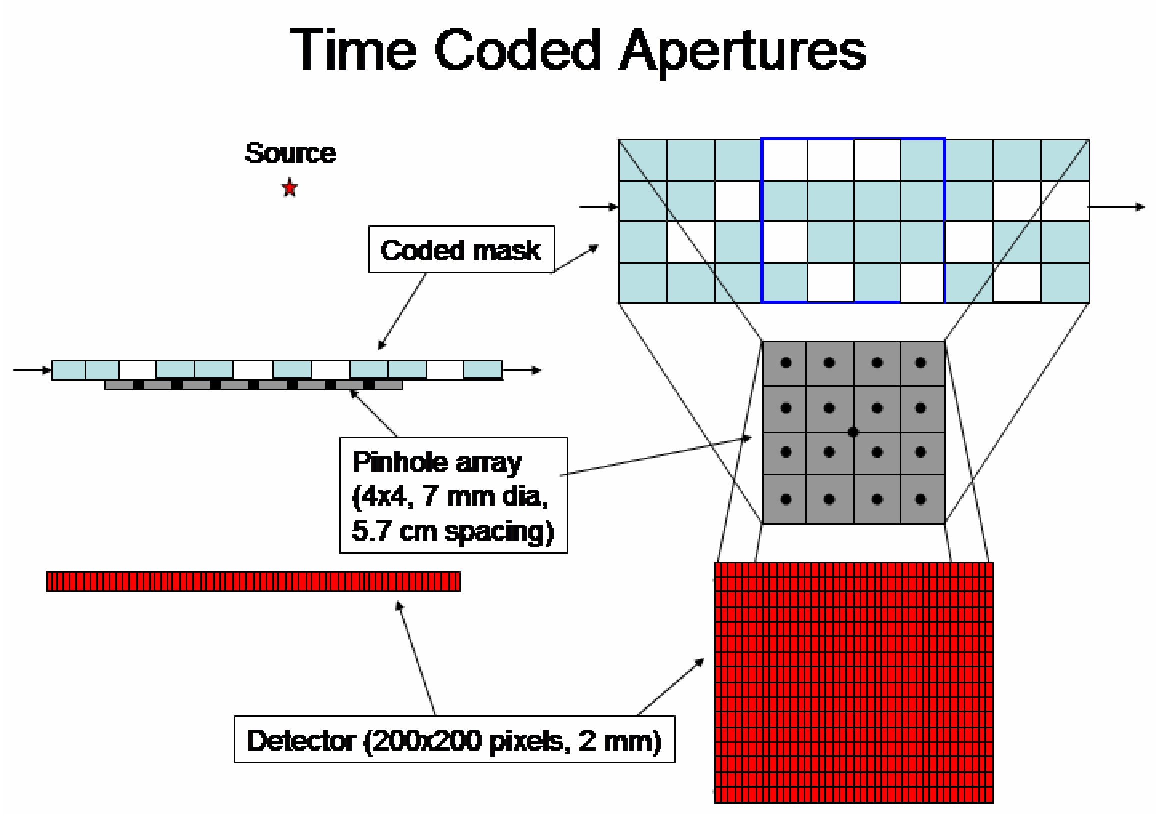

Figure 5-3. This illustrates how a time coded aperture operates. The coded mask is moved across the pinhole aperture and position sensitive detector. At each time step the mask stops and a measurement is made. The combined measurements at all mask positions produce a higher quality image than just a single coded aperture alone.

All of the measured data are then processed an appropriate image reconstruction algorithm. Because the process uses different realizations of the same source scene, the noise from each individual image tends to cancel out and the sources are highlighted. For mobile applications at standoff distances, the use of a large tungsten plate is not feasible due to size and mass constraints. A clever RMC mask design can accomplish the same purpose in a portable package. In this case a pseudorandom mask pattern would be cut in the front and rear masks. As the masks rotate the projection of the front mask onto the rear mask will cause some of the holes to appear open and some to be closed. At one position a certain pattern will be open, but at another position a different pattern will be open. While the exact design is not clear at this point, this method should work for making a portable time coded aperture. The only tradeoff is that a position sensitive detector would need to be used. The benefit is a system that may be sensitive to weaker sources than are currently measured using the RMC or a static coded aperture.

It is apparent that there are many directions that the research can go from here. The RMC is an excellent candidate for stand off detection problems and its simple design makes it attractive for a wide range of other terrestrial imaging tasks. No significant obstacles appear to impede this system for the orphan source search problem and future development should be pursued.

APPENDICES

APPENDIX A

DERIVATIONS AND COMPUTATIONS

A.1 Log- Likelihood Function and Fisher Information

One method for parameter estimation uses the concept of maximum likelihood. In this context the process is to define a likelihood function, which is describes the PDF of the system as a function of the unknown parameters [Kay93-I]. The Poisson distribution can be written as

$$P\left\{x=k\right\}=\frac{e^{-\lambda}\lambda^{k}}{k!}, \tag{A.1}$$

where x is a random variable and λ is the expected value of x [Pap02]. Assuming statistical independence, the likelihood function is defined in terms of the probability densities of values given in the vector $\underline{x}$ as

$$L(\theta)= f(\underline{x};\theta)=\prod_{n=1}^{N}\frac{\theta_{n}}{x_{n}!}\cdot e^{-\theta_{n}}, \tag{A.2}$$

where L(θ) is a function of θ defined for a set of fixed values of $\underline{x}$ [Her99]. When applied to the RMC problem, $\underline{x}$ is the measured data while θ contains the unknown parameters to be estimated. With the RMC data,

$$y_{n} \sim Poisson\left(\tau_{n}\left[s_{n}\left(\theta\right)+b\right]\right) \tag{A.3}$$

and our model for the mean is

$$\bar{y}_{n}\left(\theta\right)=\tau_{n}\left[s_{n}\left(\theta\right)+b\right]. \tag{A.4}$$

In Eqs. A.3 and A.4 τ_n is the dwell time for measuring the n_{th} bin, s is the signal, b is the background, and θ contains the unknown parameters to be estimated. Plugging these definitions back into Eq. A.2 the likelihood function is now

$$L\left(\theta\right)=\prod_{n=1}^{N}\frac{\overline{y}_n\left(\theta\right)}{y_n!}\cdot e^{-\overline{y}_n(\theta)}. \tag{A.5}$$

A more useful quantity is the log-likelihood function, which is found by taking the natural logarithm of both sides of Eq. A.5, or

$$\begin{aligned}\log\left[L\left(\theta\right)\right]&=\log\left[\prod_{n=1}^{N}\frac{\overline{y}_n\left(\theta\right)^{y_n}}{y_n!}\cdot e^{-\overline{y}_n(\theta)}\right]\\&=\sum_{n=1}^{N}y_n\log\left(\overline{y}_n\left(\theta\right)\right)-\overline{y}_n\left(\theta\right)-\log\left(y_n!\right) \qquad \text{(A.6)}\\&=\sum_{n=1}^{N}y_n\log\left(\overline{y}_n\left(\theta\right)\right)-\overline{y}_n\left(\theta\right)-C.\end{aligned}$$

It should be noted that the last term in Eq. A.5 is a constant in θ and therefore irrelevant to the parameter estimation problem [Her99]. The log-likelihood is beneficial because it imposes a non-negativity constraint on the data, produces a function that is strictly smooth and concave and is directly related to the information content in a system through a parameter known as the Fisher Information [Her99].

The Fisher Information is a measure of the information in a given system and is stated in terms of the log-likelihood function as

$$F\left(\theta\right)=-E\left[\frac{\partial^2\log\left(L\left(\theta\right)\right)}{\partial\theta^2}\right]. \tag{A.7}$$

Using the log-likelihood function for a Poisson process and Eq. A.7, the Fisher Information of the generic RMC system can now be derived. Taking the first and second partial derivatives of the log-likelihood function with respect to q and then the negative of the expectation yields

$$\frac{\partial\left[\log\left(L(\theta)\right)\right]}{\partial\theta}=\sum_{n=1}^{N}\frac{y_n}{\overline{y}_n(\theta)}\cdot\frac{\partial\overline{y}_n(\theta)}{\partial\theta}-\frac{\partial\overline{y}_n(\theta)}{\partial\theta}$$

$$\frac{\partial^2\left[\log\left(L(\theta)\right)\right]}{\partial\theta^2}=\sum_{n=1}^{N}\frac{y_n}{\overline{y}_n(\theta)}\cdot\frac{\partial^2\overline{y}_n(\theta)}{\partial\theta^2}-\frac{y_n}{\overline{y}_n(\theta)^2}\cdot\frac{\partial^2\overline{y}_n(\theta)}{\partial\theta^2}-\frac{\partial^2\overline{y}_n(\theta)}{\partial\theta^2}$$

$$-E\left[\frac{\partial^2\left[\log\left(L(\theta)\right)\right]}{\partial\theta^2}\right]=\sum_{n=1}^{N}\frac{\overline{y}_n(\theta)}{\overline{y}_n(\theta)}\cdot\frac{\partial^2\overline{y}_n(\theta)}{\partial\theta^2}-\frac{\overline{y}_n(\theta)}{\overline{y}_n(\theta)^2}\cdot\frac{\partial^2\overline{y}_n(\theta)}{\partial\theta^2}-\frac{\partial^2\overline{y}_n(\theta)}{\partial\theta^2} \tag{A.8}$$

$$F(\theta)=\sum_{n=1}^{N}\frac{1}{\overline{y}_n(\theta)}\frac{\partial^2\overline{y}_n(\theta)}{\partial\theta^2}.$$

It is common to come across problems in which many parameters are estimated. In these situations, the unknown parameters θ are placed in vector form and the Fisher Information is restated in matrix form as

$$\underline{\underline{F}}(\underline{\theta})=\sum_{n=1}^{N}\frac{1}{\overline{y}_n(\underline{\theta})}\nabla_{\theta}\overline{y}_n(\underline{\theta})\nabla_{\theta}{}^{T}\overline{y}_n(\underline{\theta}). \tag{A.9}$$

An important item to note is that the Fisher information is not dependent on the measured data, but rather only on the expected values and their gradients, which are computed with a user-defined system model. The Fisher Information can therefore be used to provide insight for optimal system model designs provided it sufficiently models the real system.

APPENDIX B

EXPERIMENTAL SETUP AND SYSTEM SETTINGS

B.1 List of Equipment Used and Commonly Applied Settings

Equipment List:

Oscilloscope: LeCroy Waverunner 44Xi
NIM bin: Ortec 4001A
Detector/PMT: St. Gobain 3M3/3, Sodium Iodide (3x3")
PMT Base/Voltage Divider: Ortec 266
High Voltage Power Supply: Tennelec 952A
Pre-Amplifier: Ortec 113
Shaping Amplifier: Ortec 572
Single Channel Analyzer: Ortec 550
Quad Counter: Ortec 974
Multi-Channel Analyzer: Ortec 926 ADCAM
Data Acquisition Board: National Instruments 6111 E-PCI using a SCB-68 interface
Stepper Motor: Applied Motion HT23-297
Motor Driver: Applied Motion Si3540
Optical Encoder Ring: Renishaw RESR R20-115
Encoder Read Head: RGH 20
Decoder: Avago HCTL – 2016 on a National Instruments USB interface 6008
Source Positioning System: Velmex Unislide K1M01

Commonly Applied Equipment Settings:

HVPS: 800 Volts, polarity = +
Pre-Amplifier:
    Capacitance: 200 μF
Amplifier:
    Coarse Gain: 50
    Fine Gain: 12.8 (module has an offset, this gain setting equals 1)
    Shaping Time: 2 μs
SCA:
    Mode: Normal
    Window Settings: Variable based on source used
MCA:
    Resolution: 4096

Commonly Applied Motor Settings: (settings below show commands provided to motor driver)

Motor Resolution: MR13 (36000 steps per revolution)
Velocity: VE0.1363 (15 rpm)
Acceleration: AC360
Deceleration: DE360
Motor Current: CC0.8 (0.8 amps)
Step Size: DI327 (327 steps per degree)

B.2. Schematic and Picture of the Decoding Circuit

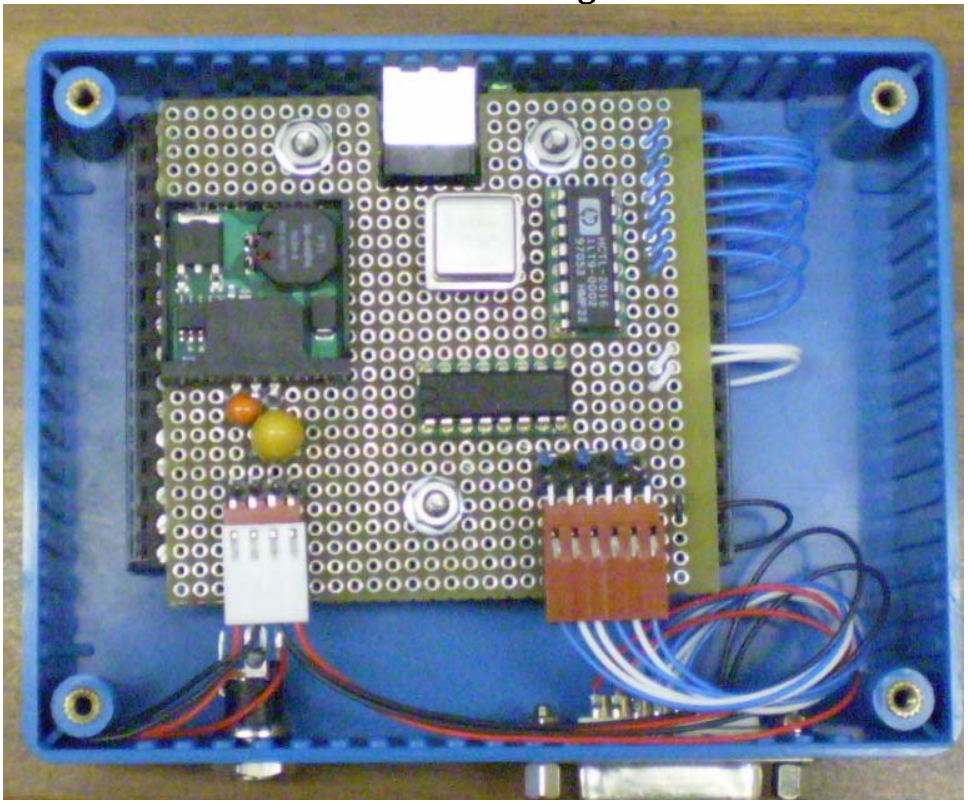

The picture above shows the decoding circuit that was built to convert the raw output from the Renishaw rotary encoder into useful angular position data. The decoder box has dimensions of 12x9x3.5 cm.

B.3. List of Sources Used in this Research

Source	Activity [μCi]	Serial #	Reference Date
Ba-133	48.54	1309-27	7/1/2008
Ba-133	2000	D1-354-1142-49	2/1/2006
Cs-137	4000	D2-292-1142-66	6/1/2006
Cs-137	94.73	989-11-5	5/1/2003
Co-60	103.8	989-11-4	5/1/2003
Na-22	100.8	989-11-7	5/1/2003

APPENDIX C

TWO DIMENSIONAL IMAGES OF MASK PENETRATIONS MEASURED USING A HPGE STRIP DETECTOR

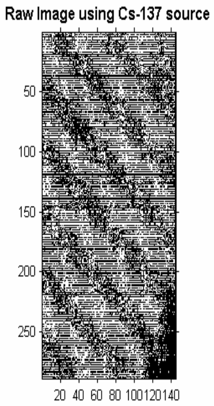

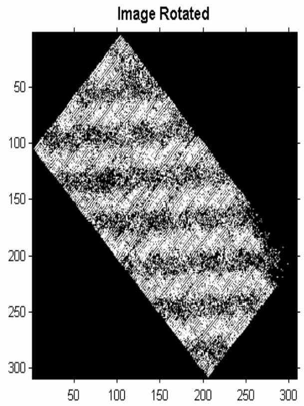

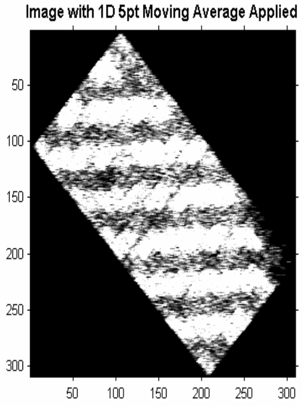

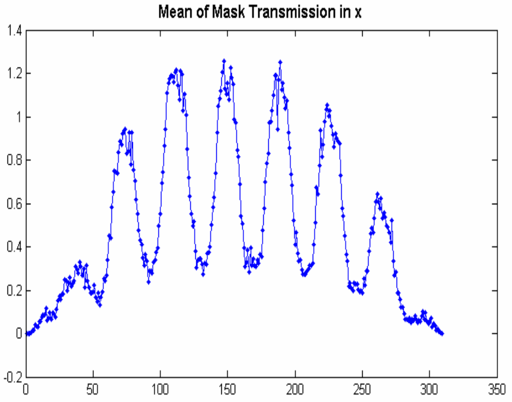

The pictures above are measured planar images of a set of RMC masks using a high-purity germanium (HPGe) strip detector and a 4 mCi Cs-137 source (662 keV). The dark bands show the mask slits and the light areas are openings in the mask pair. The picture in the bottom right is a plot of a slice taken across the image. Because the masks are not completely opaque, the transmission as a function of position on the mask are not square waves as shown in Fig. 2-3, but are instead rounded. Pictures like this can be used to understand how to properly model the mask penetrations.

REFERENCES

[App08] Applied Motion Products, "Hardware Manual – Si3540 Programmable Step Motor Driver". http://www.applied-motion.com/ampinfo/manuals/si3540web.pdf. 2008.

[Ava06] Avago Technologies, "HCTL-2000 Quadrature Decoder/Counter Interface ICs Data Sheet". http://www.avagotech.com/products/motion_control_solutions/integrated_circuits/decoder/hctl-2016/. 2006.

[Bar08] Barrett, H.H., Furenlid, L.R., Freed, M., Hesterman, J.Y., Kupinski, M.A., Clarkson, E., and Whitaker, M.K. "Adaptive SPECT", IEEE Trans. on Medical Imaging, Vol 27, #6. Jun. 2008. pp. 775-788.

[Ber08] Berry, J.E. Private communication on a compact data acquisition system for the RMC. 2008.

[Bra68] Bradt, H., Garmire, G., Oda, M., Spada, G., and Sreekantan, B.V. "The Modulation Collimator in X-Ray Astronomy". Space Science Reviews. Vol 8. 1968. pp. 471-506.

[Cli95] Clinthorne, N.H., Rogers, W.L., He, Z., and Wehe, D.K. "Time-Coded Apertures for Imaging in High-Background Environments". IEEE Trans. on Nuclear Science. October 1995. pp. 1-7.

[Eis97] Eisenbud, M. and Gesell, T. "Environmental Radioactivity: From Natural, Industrial, and Military Sources – 4th Edition". Academic Press. 1997.

[Fer03] Ferguson, C.D., Kazi, T., Perera, J. "Commercial Radioactive Sources: Surveying the Security Risks". Monterey Institute for International Studies: Center for Nonproliferation Studies. Occasional Paper #11. Jan. 2003.

[Fis90] Fisher, T.R., Hamilton, J.W., Hawley, J.D., Kilner, J.R., Murphy, M.J., and Nakano, G.H. "Imaging of Gamma Rays with the WINKLER High-Resolution Germanium Spectrometer". IEEE Trans on Nucl Sci, Vol 37, #3. June 1990. pp. 1483-1489.

[Fre08] Freed, M., Kupinski, M.A. Furenlid, L.R., Wilson, D.W., Barrett, H.H. "A Prototype Instrument for Single-Pinhole Small-Animal Adaptive SPECT Imaging", submitted to Med. Phys., 2008.

[Gai96] Gaither, G.C., Schmahl, E.L., Crannell, C.J., Dennis, B.R., Lang, F.L., Orwig, L.E., Hartman, C.N., and Hurford, G.J. "Quantitative Characterizations of the X-Ray Imaging Capability of Rotating Modulation Collimators with Laser Light", Applied Optics, Vol 35, #34. 1996. pp. 6714-6726.

[Got71] Gotoh, H. and Yagi, H. "Solid Angle Subtended by a Rectangular Slit". Nuclear Instruments and Methods. Vol 96. 1971. pp. 485-486.

[Huf02] Hurford, G.J., Schmahl, E.J., Schwartz, R.A., Conway, A.J., Aschwandan, M.J., Csillaghy, A., Dennis, B.R., Johns-Krull, C., Krucker, S., Lin, R.P., McTiernan, J., Metcalf, T.R., Sato, J., Smith, D.M. "The RHESSI Imaging Concept", Kluwer Academic Publishers. 2002.

[Joh01] Johnson, Roger W. "An Introduction to the Bootstrap". Teaching Statistics. Vol 23-2. Summer 2001. pp. 49-54.

[Kay93-I] Kay, S.M. "Fundamentals of Statistical Signal Processing: Estimation Theory". Prentice-Hall, Inc. 1993.

[Kay93-II] Kay, S.M. "Fundamentals of Statistical Signal Processing: Detection Theory". Prentice-Hall, Inc. 1993.

[Kno00] Knoll, G.F. "Radiation Detection and Measurements, 3rd Edition", John Wiley & Sons, Inc. 2000.

[Lun81] Lund, N. "Gamma-Burst Studies Using Long-Duration Balloon Flights in the Arctic". Astrophysics and Space Sciences. Vol. 75. 1981. pp. 145-151.

[Mat07] Matlab R2007b. "Help Guide". The MathWorks. 2007.

[May74] May, R.S., Akcasu, Z., and Knoll, G.F. "Gamma-Ray Imaging with Stochastic Apertures". Applied Optics. Vol. #13, Issue 11, pp. 2589-2601.

[Mer67] Mertz, L. "A Dilute Image Transform with Application to an X-Ray Star Camera". Symposium on Modern Optics. Polytechnic Institute of Brooklyn. Mar 1967. pp 787-791.

[Mer71] Mertz, L. "Numerical Image Synthesis For a Ring Pupil". Optica Acta. Vol 18, #1. 1971. pp 51-57.

[Mer86] Mertz, L.N., Nakano, G.H., and Kilner, J.R. "Rotational Aperture Synthesis for X-Rays", J. Optical Society of America. Vol 3, #12. Dec 1986. pp. 2167-2170.

[Mur89] Murphy, M.J. "The Virtues of Positive-Definite Reconstruction of X-Ray and Gamma-Ray Images". NIM-A, Vol 290. 1989. pp. 551-558.

[Nat08] National Instruments. "LabVIEW Professional Development System – version 8.2". National Instruments. 2006.

[Oda65] Oda, M. "High-Resolution X-Ray Collimator with Broad Field of View for Astronomical Use". Applied Optics. Vol. 4, #1. Jan. 1965. pp. 143.

[Tay03] Taylor, G.M. Ed. “Dirty Bombs: RDD report offers steps to reduce threat”. Nuclear News. Vol 46. #3. Mar. 2003. pp. 37-39.

[Pos63] Posner, E.C. “Optimal Search Procedures”. IEEE Trans on Info Theory. 1963. pp. 157-160.

[Ren08] Renishaw. “RESR angle encoder system – Data Sheet L-9517-9128-04-C”. http://www.renishaw.com/media/pdf/en/7c14706839e54dff99cdcc768c93aada.pdf. 2008.

[RHE08] RHESSI Home Page. http://hesperia.gsfc.nasa.gov/hessi/. 2008.

[Sch68] Schnopper, H.W. and Thompson, R.I. “Predicted Performance of a Rotating Modulation Collimator for Locating Celestial X-Ray Sources”. Space Science Reviews. Vol 8. 1968. pp 534-542.

[Sch70] Schnopper, H.W. et al. “Precise Location of Sagittarius X-Ray Sources with a Rocket-borne Rotating Modulation Collimator”,

[Sha06] Sharma, A.C. et al. “Rotating Slat Collimator Design for High-Energy Near-Field Imaging”. Proc. SPIE. Vol 6142. 2006.

[Sha07-I] Sharma, A.C. et al. “Design and Development of a High-Energy Gamma Camera for Use with NSECT- Imaging: Feasibility for Breast Imaging”. IEEE Trans Nucl Sci. Vol 54, #5. Oct 2007. p 1498-1507.

[Sha07-II] Sharma, A.C. “Development and Design of a Near-Field High-Energy Gamma Camera for use with Neutron Stimulated Emission Computed Tomography”, Ph.D. Dissertation, Department of Biomedical Engineering, Duke University. 2007.

[She86] Shepp, L.A. and Vardi, Y. “Maximum Likelihood Reconstruction for Emission Tomography”. IEEE Trans on Medical Imaging, Vol M1-1, #2. Oct 1982. pp. 113-122.

[Shu00] Shultis, J.K. and Faw, R.E. “Radiation Shielding”. American Nuclear Society. 2000.

[Smi98] Smith, E.L. “Design, Modeling, and Performance of a Hybrid Portable Gamma Camera”, Ph.D. Dissertation, Department of Nuclear Engineering and Radiological Sciences, University of Michigan. 1998.

[Smi04] Smith, D.M., Huford, G.J., Boggs, S.E. “Rotating Modulation Collimator Imagers”. New Astronomy Reviews. Vol. 48. 2004. pp. 209-213.

[Try99] Tryka, S. “A Method for Calculating the Average Solid Angle Subtended by a Circular Disk from Uniformly Distributed Points within a Coaxial Circular Plane”, Rev of Sci Instr. Vol 70 #10. 1999. pp 3915-3920.

[Wil70] Wilmore, A.P. "The Imaging Properties of the Rotation Collimator", Monthly Notices of the Royal Astronomical Society. Vol 147. 1947. pp 387-403.

[Zio02] Ziock, K.P and Goldstein, W.H. "The Lost Source, Varying Background, and Why Bigger May Not Be Better". Unattended Radiation Sensor Systems for Remote Applications. Ed. Trombka, J.I. et al. American Institute of Physics. 2002. pp. 60-70.

[Zio07] Ziock, K.P. and Nelson, K.E. "Maximum Detector Sizes Required for Orphan Source Detection". NIM-A. Vol 579. 2007. pp. 357-362.

[Zio07-II] Ziock, K.P., Craig, W.W., Fabris, L., Lanza, R.C., Gallagher, S., Horn, B.K.P, and Madden, N.W. "Large Area Imaging Detector for Long-Range Passive Detection of Fissile Material". IEEE Trans. on Nuclear Science. Vol 51, #5. October 2004. pp. 2238-2244.